EPITAXIAL GROWTH AND REAL-TIME ELECTRON DIFFRACTION ANALYSIS OF ADVANCED III-V SEMICONDUCTOR-BASED QUANTUM DOTS

A Dissertation Presented to
the Faculty of the Department of Physics
University of Houston

In Partial Fulfillment
of the Requirements for the Degree
Doctor of Philosophy

By
Manori Vajira Chintha Gunasekera
May 2015

EPITAXIAL GROWTH AND REAL-TIME ELECTRON DIFFRACTION ANALYSIS OF ADVANCED III-V SEMICONDUCTOR-BASED QUANTUM DOTS

_____
Manori V. Gunasekera

APPROVED:

_____
Dr. Alexandre Freundlich
Advisor

_____
Dr. Wei-Kan Chu

_____
Dr. Donna Stokes

_____
Dr. Lowell Wood

_____
Dr. Wanda Wosik

_____
Dean, College of Natural Sciences and Mathematics

ACKNOWLEDGMENTS

First and foremost I would like to thank my advisor Alexandre Freundlich. I am honored to be his Ph.D. student and he taught me, both consciously and unconsciously, how good theoretical and experimental physics is done. I deeply appreciate all his contributions of time, ideas, and funding to make my Ph.D. experience productive and stimulating. The joy and enthusiasm he has for his research was contagious and motivational for me, even during tough times in the Ph.D. pursuit.

I am thankful to my committee members Dr. Wei-Kan Chu and Dr. Lowell Wood for their excellent support; I am also thankful to Dr. Donna Stokes and Dr. Wanda Wosik for the excellent example provided as successful woman physicists and professors.

I would also like to express my thanks to Dr. Chandani Rajapaksha, a former student, for her guidance and support as a mentor when I started my research work. Many thanks to our lab manager Carlos Gramajo for his involvement in maintaining the lab clean and safe.

The members of the Center for Advance Materials group have contributed immensely to my personal and professional time at University of Houston. The group has been a source of friendships as well as good advice and collaboration. I am especially grateful for Dr. Akhil Mehrotra and Dr. Gopi Krishna, my former fellow students for teaching and helping me with experiments and I have had the pleasure to work alongside with them. My heartfelt gratitude goes to my fellow graduate students Wei Wang, for her lovely companionship, Kaveh Shervin, for being an understanding friend and his immense support all the time, Michael Fitchette, for his timeless support in correcting manuscripts, Camden Kirkland, for his help whenever needed, and Khim Kharrel, for being a helping hand for and the numerous summer and rotation students who have come through the lab.

I am indebted to all internal collaborators Dr. Wei-Kan Chu, Dr. Buddhi Thilakarathne, and Dr. Dharshana Wijesundara for providing access and performing AFM measurements without any hesitations. I am also grateful to my fellow student Dr. Dinghao

Tang under supervision of Dr. David Smith at Arizona State University and Dr. Irena Rusakova for TEM image processing.

I am pleased to thank administrative staff Naomi Haynes, the graduate coordinator at Department of Physics, and Yessica Contreras and Nancy Do at Center for Advanced Materials for being always supportive.

My beloved parents, Peter (late) and Podimenike Gunasekera, receive my deepest gratitude for making me who I am today, and I dearly thank my brother Sanjaya Gunasekera and sister Neranjala Gunasekera for always being there for me. I would also like to express my gratitude to my parents-in-law, Milton and Mala Weerasinghe, for being my second parents.

A special thanks goes to my little jewel Rayani and the new coming baby for endless love and the strength I feel because of them. And most of all, none of the degree would have been possible if it were not for my loving husband, Indika Weerasinghe. My greatest appreciation goes to him for standing by me in every foot step of my Ph.D. work and life. This dissertation is dedicated to him.

EPITAXIAL GROWTH AND REAL-TIME ELECTRON DIFFRACTION ANALYSIS OF ADVANCED III-V SEMICONDUCTOR-BASED QUANTUM DOTS

An Abstract of a Dissertation
Presented to
the Faculty of the Department of Physics
University of Houston

In Partial Fulfillment
of the Requirements for the Degree
Doctor of Philosophy

By
Manori Vajira Chintha Gunasekera
May 2015

ABSTRACT

The impact of growth kinetics on structural properties significantly affects optical and electronic performances of self-assembled Stranski-Krastanov (SK) quantum dots. Here and within the framework of the synthesis of archetype InAs/GaAs quantum dot system we have undertaken a systematic study on the evolution of dot facet orientation in terms diffraction characterization by the reflection high-energy electron diffraction (RHEED) technique. The existence of a sharp transition of facet arrangements and shapes near the onset of dot formation is investigated, and a dot structure bound by {2 5 11} facets is proposed. During further calculations, we observed asymmetric ripening of quantum dot facets at initial growth stages, and as the dot ripens, more symmetric facet arrangement to the incident direction was noted. Further, incorporating the correlation between dot structural properties and RHEED intensity features, we propose structures for quantum dots bounded by {1 3 6} and $\{1\ \bar{3}\ 5\}$ facets for both asymmetric and symmetric situations.

In addition, development of advanced quantum dot structures to fabricate wetting layer separated InAs quantum dots is implemented. Improvement of photoluminescence emission from InAs quantum dots embedded in a GaAs matrix is presented at the end of the work.

CONTENTS

Chapter 1

Introduction

In the applications of microelectronic devices, the electronic structure of the material can be tailored by confining carriers in low-dimensional systems. Unlike one-dimensionally confined quantum wells (QWs) with Heaviside density of states (DOS) and two-dimensionally confined quantum wires with parabolic sub band DOS, three-dimensional confinement in quantum dots (QDs) leads to atom-like energy level structure, that is of interest to solid state physicists as well as commercial applications such as lasers, single-electron pumps, light-emitting diodes (LEDs) and biomoleclular markers. The first discovery of size effects of QDs is ascribed to A. I. Ekimov in 1981 who observed the size dependence of CdS and CuCl microcrystals grown in transparent dielectric matrix. In later findings, a short wavelength shift of the exciton lines and the fundamental absorption edge was reported (Ekimov, Efros, and Onushchenko 1985).

The unique properties of quantum dots are derived from quantization of electron energies which leads to dramatic changes in transport and optical properties. Among different technological applications based on QDs, the concept of semiconductor QDs in LED first emerged in 1990s. Tuning of QDs (by varying the size) for emission at any wavelength longer than the source wavelength with very high efficiency and with very narrow spectral distribution is used to engineer the light spectrum in display industry. In addition, QDs are very promising as an active material for solid state lasers due to the discrete energy spectrum and the theory was first proposed by Arakawa and Sakaki in 1982 (Arakawa and Sakai 1982) . First 1.3-μm III-V quantum dot lasers were grown on Ge substrates with performance comparable to devices grown on native III-V substrates. Nowadays, 1.3-μm lasers capable of operating in high temperature environment have also been demonstrated (Huffaker *et al*. 1998) (Liu *et al*. 2011).

Fabrication of QDs is branched into several technologies including semiconductor nanocrystal QDs (NCQD), lithographically made QDs (LGQD), field-effect QDs (FEQD) and self-assembled QDs (SAQD) (Lakhtakia 2004). Stranski-Krastanov growth mode which will be discussed later leads to self-assembled QDs with excellent photonic properties (Sanguinetti *et al.* 1999).

1.1 Motivation and state of the technology

Stranski-Krastanov (SK) growth mode is the most common and effective self-assembled dot nucleation method in fabricating coherent and defect free islands with high homogeneity and is vastly studied because of its complex kinetics and thermodynamics. The release of strain energy accumulated in the absorbent layer which originates from the

lattice mismatch between the absorbent and the substrate is the key factor in SK-type island formation. For instance, within the framework of InAs/GaAs SKQD studied in this work the 7.2% of lattice mismatch in InAs on GaAs heteroepitaxial system forms InAs quantum dots by elastic relaxation at two-dimensional InAs wetting layer.

From the application point of view, QD shape and size define its electronic structure and optical properties, hence the dot shapes have been examined intensively in literature. Several post-fabrication studies have been carried out in extracting dot shapes; specifically attempts have been made to extract facet orientations. Atomically resolved scanning tunneling microscopy (STM) studies have revealed the occurrence of {1 3 7} facets in smaller quantum dots (Márquez, Geelhaar, and Jacobi 2001). At later stages of growth process, the dot shape is founded to be terminated by steeper facets of {1 1 0} , {1 1 1} and $\{\overline{1\ 1\ 1}\}$ families (Xu *et al.* 2005) (Kratzer *et al.* 2006).

However, an *in-situ* analytical tool for real-time assessment is more desirable as it extracts dot parameters under same fabrication conditions particularly growth temperature. Prior to this work, reflection high-energy electron diffraction (RHEED) has become a standard qualitative *in-situ* diagnosis tool for SK dot structural characterization as it is a highly sensitive, simple and nonintrusive technique which can be easily incorporated into any epitaxial growth system. The diffraction patterns from RHEED have been used in probing surface morphological changes during epitaxial growths. In the process of self-assembled quantum dot fabrication, the nucleation from wetting layer to quantum dots follows a transformation of 2D streak lines from the WL into three-dimensional inverted vee shaped features from quantum dots. These inverted vee-shaped features are called

chevrons and originate from refraction and transmission diffraction through island facets. The initial studies of RHEED of InAs/GaAs quantum dots have deduced a square-based pyramidal structure bounded by {1 1 3}*A* facets from RHEED observations at [1 $\bar{1}$ 0] and [1 1 0] (Nabetani *et al.* 1994) and a structure terminated by {1 3 6} facets has been proposed based on an analysis of the chevron angle appeared along [1 $\bar{3}$ 0] and [3 $\bar{1}$ 0] azimuths (Lee *et al.* 1998). More recent studies of *in-situ* atomically resolved scanning tunneling microscopy (STM) reveal that the smallest QDs observed are bounded by {1 3 7} facets (Xu *et al.* 2005). These studies have contributed in conducting *in-situ* characterization of dot morphology to improve reproducibility and control over dot structural parameters. Yet, for a precise controllability the lack of real-time assessments had been an issue and our group has been able to address this matter by building a theoretical model based on RHEED calculations.

As an initial approach, our group has investigated the capability of RHEED in extracting QD size from periodic intensity fringes along chevron tails, dot density from RHEED intensity and shape from chevron angles with the use of a in-house developed theoretical model mentioned above (Feltrin and Freundlich 2007b)(Feltrin and Freundlich 2007a). The model calculates diffraction patterns from the kinematic theory within the framework of first Born approximation for the electrons scattering in the forward direction. The effect of atomic vibrations was later added to the model as a function of Debye temperature (Rajapaksha and Freundlich 2009). For the validation of simulated RHEED images, diffraction patterns recorded during experimentally grown InAs QDs on GaAs(001) have been used. Chevron angle observations along [1 $\bar{1}$ 0] , [1 1 0] and [1 $\bar{3}$ 0] have been

investigated to infer a QD structure with {1 3 7} and {1 1 3} facets as the initial shape of self-assembled InAs QDs (Freundlich, Rajapaksha, and Gunasekera 2011). These simulated images have been compared with the calculations applied for QD structures suggested by Lee *et al.* (1998), Xu *et al*. (2005), and Kratzer *et al*. (2006). Furthermore, a real-time assessment on average dot height evolution during growth has also been discussed (Rajapaksha 2010). Oscillations of RHEED intensity profiles along chevron tails have been associated with dot heights and the evolution of dot size has been studied as a function of growth time. This work is a continuation of these previous analysis and further details will be discussed below.

1.2 Summary of the objectives and organization

The underlying objective of this work will be discussed in this section. As an approach the structure of the dissertation manuscript will be stated first. Basic requirements and formation of quantum heteroepitaxial systems are reviewed in the second chapter. Different growth modes will be introduced and SK growth mode will be the main focus. The role of strain on the formation of self-assembled QDs is also included.

The fabrication method of such QDs is molecular beam epitaxy (MBE). The growth technique, mechanisms and dot properties of MBE grown nano islands are noted in Chapter 3. The fourth chapter is dedicated to fundamentals of RHEED and its applications in QD analysis.

The development of theoretical simulation of InAs QD structure on GaAs(001) using atomistic Valence Force Field approach(VFF) and the calculation of RHEED diffraction

images by kinematical theory are described in chapter 5. Prior work performed by the group is also presented as an approach for the next chapter.

In chapter 6, the experimental procedure is given at first. Then my studies on extracting dot shapes at the onset of dot formation are presented. Dot structures are calculated by taking RHEED investigations of experimental observations of InAs QDs grown on GaAs(001) into account. The study is performed at growth temperatures 440^0C and 480^0C and corresponding average size evolutions are also compared. A new chevron angle of $45.2^0 \pm 1^0$ at InAs deposition of 1.6ML is extracted and the relevant dot structure is calculated to be {2 5 11} facets. The first evidence of dot facet asymmetries is also noted in this chapter and the results are justified using chevron angles and intensity periodicities.

Development of advanced QD structures will be exhibited in chapter 7 preceded by the growth technique. GaAs and AlAs intermediate layer incorporated QDs are studied to find the possibility of fabricating WL free QDs. Photoluminescence (PL), tunneling electron microscopy (TEM), Atomic force microscopy (AFM), and RHEED investigations are carried out and the comparisons of the results are given here.

Chapter 8 concludes and summarizes the research outcomes and the future outlook on the subject is also noted.

Chapter 2

Quantum Dot Heterostructures

In this chapter an overview of Quantum dot heterostructures will be discussed. In section 2.1, basis criteria for fabrication of quantum heterostructures and three heteroepitaxial growth modes, Frank-van der Merwe (Frank and Merwe 1949), Volmer Weber (Volmer and Weber 1925), and Stranski-Krastanov (Stranski and Krastanov 1938) mechanisms are presented. Section 2.2 describes different growth stages of SK dot growth: first the formation of InAs WL on GaAs(001) archetype system is described in terms of surface energy and the calculation for critical thickness is included. Next the transition from 2D layer growth to 3D island nucleation and surface morphological changes are presented. The final part under section 2.2 focuses on three-dimensional phase of self-assembled SK InAs/GaAs (001) QDs where energetics of SK growth mode is discussed in terms of surface energies and strain relaxation energies. In section 2.3 equilibrium dot shapes proposed in literature are presented.

2.1 Heteroepitaxial systems

Semiconductor structures in which layers of different chemical compositions and unequal bandgaps are present are called heterostructures. Size quantization effect in these structures lead to quantum confinement with sharper density of states with unique electronic and optical properties. Achieving the following four basic requirements hence become essential in the production of quantum heterostructures (Joyce and Vvedensky 2004).

I. Small lateral size which is related to carrier effective masses to achieve expected quantum confinement.

II. Relatively narrow size distribution to avoid inhomogeneous broadening of electronic transitions in optical applications.

III. Interfaces with high degree of definition to produce an abrupt carrier-confinement potential.

IV. Structural and chemical stability: i.e. the interfaces must retain their chemical integrity and be stable against the formation of structural defects during all stages of fabrication.

Deposition of atoms and molecules in an ordered manner in layer by layer growth (epitaxial) is the best solution in fabricating thin films and low-dimensional structures which satisfies the above criteria. Chemical vapour deposition (CVD), metal-organic vapour phase epitaxy (MOVPE), liquid phase epitaxy (LPE) and chemical beam epitaxy (CBE) are a several suitable epitaxial growth techniques and among those molecular beam epitaxy (MBE) is the best candidate and more on this growth technique will be discussed

in Chapter 3. The epitaxial films grown by these techniques are categorized under three modes governed by interfacial surface energies and strain energies due to lattice mismatch between layers. The growth modes are classically described as follows and a schematic of each mode with examples is given in Figure 2.1: (Bauer 1958)

I. Frank-van der Merwe (FM) : Layer-by-layer growth (Frank and van der Merwe 1949)

In FM growth mode, the deposited material contributes to the pseudomorphic growth satisfying the following condition which is called Bauer's condition for surface free energies (Bauer *et al.* 1975);

$$\gamma_s > \gamma_f + \gamma_i, \tag{2.1}$$

where γ_s is the surface free energy of the substrate, γ_f is the free energy of the film and γ_i is the interface surface free energy (Joyce and Vvedensky 2004) (Totten and Liang 2004). According to equation 2.1, to reduce the effect of higher substrate surface free energy, the film wets the substrate growing stable uniform 2D layers. Ge on Si(111) is an example of FW growth and is shown in Figure 2.1(d).

II. Volmer-Weber (VW) : 3D island growth mode (Volmer and Weber 1925)

The inequality,

$$\gamma_s < \gamma_f + \gamma_i, \tag{2.2}$$

sets the condition for the epitaxial layer form 3D island. Based on the surface energies the adadom-adatom interactions are stronger than the adatom-surface atom interactions which result in forming three-dimensional adatom clusters to minimize the higher surface free energies of adatoms. During continuous deposition, crystals

prefer to avoid each other by increasing their height by forming isolated islands (Muller and Kern 1998). As shown in Figure 2.1(e) Si on Ge (111) undergoes VW growth process.

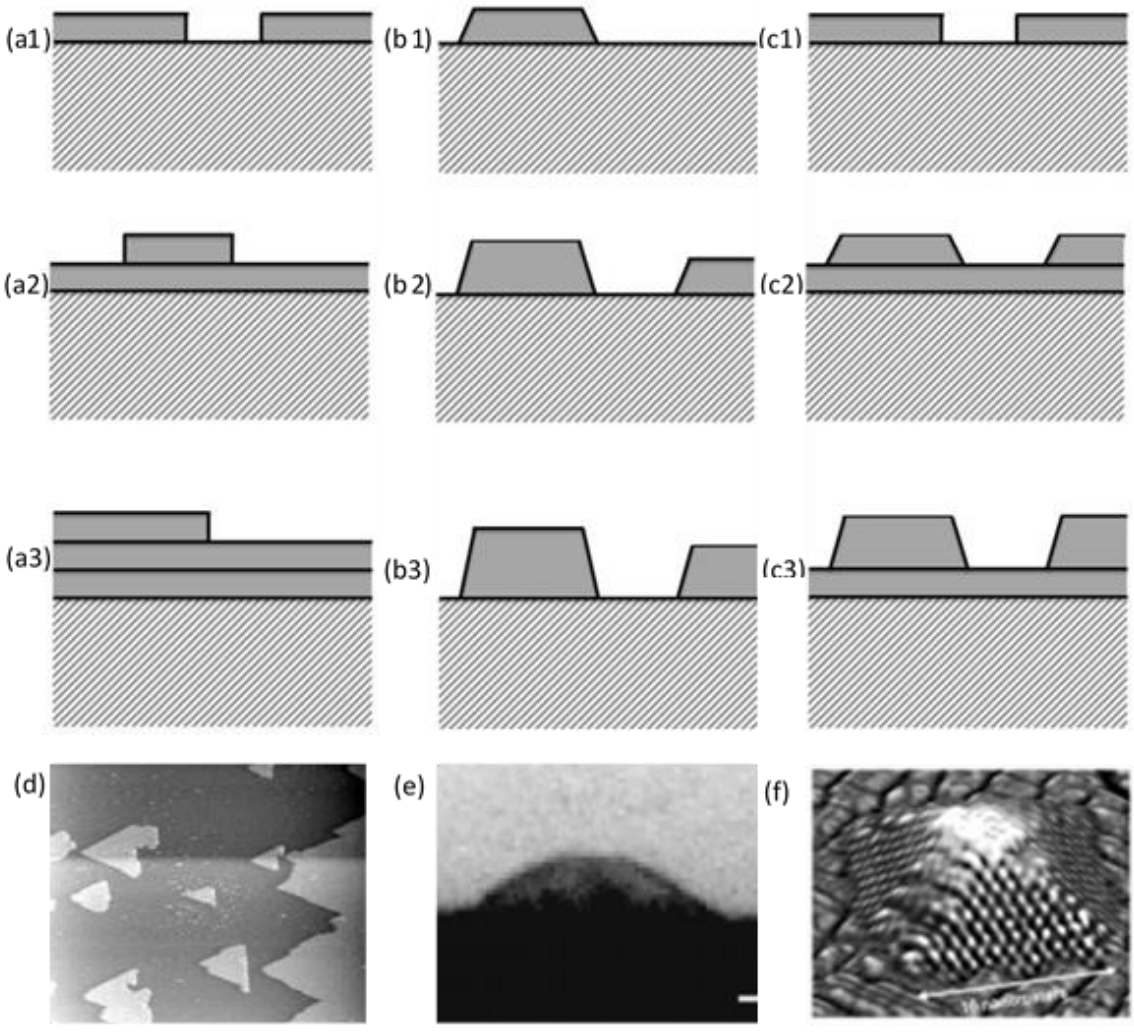

Figure 2.1. Evolution of growths (a1-a3) Frank-van der Merwer growth, (b1-b3) Volmer Weber growth, (c1-c3) Stranski-Krastanov growth, (d) FM growth of Ge film on Si (111) (Rosei *et al.* 2000), (e) VW growth of Si on Ge (111) (Raviswaran *et al.* 2000) and (f) SK growth of Ge on Si(001) (Marshall and Castell 2014).

III. Stranski-Krastanov (SK) : Layer-by-layer plus islands (Stranski and Krastanov 1938)

SK growth mode is an intermediary process of 2D layer and 3D island formations. If the inequality stated in Equation 2.1 is fulfilled for a lattice mismatched system with the strained epilayer with small interface energy, the initial layer-by-layer growth is followed by three-dimensional islands formed due to relaxation of strain built up in the system (Stranski & Krastanov 1938). Ge/Si(100) is one of the mostly studied systems which nucleate SK growths. Figure 2.1(f) is an AFM image of Ge quantum dot embedded in Si(100) matrix.

2.2 Self-assembled Stranski-Krastanov InAs quantum dots on GaAs(001)

Stranski-Krastanov quantum dots were first reported by Ivan Stranski and Lyubomir Krastanov in 1938 (Stranski and Krastanov 1938). The growth is an intermediate level between 2D layer growth (FM) and 3D island growth (VW). InAs SK dots grown on GaAs(001) are the most studied III-V compounds in literature (Goldstein *et al.* 1985). There are two factors which govern the SK growth process of InAs/GaAs(001): surface energy and the strain due to ~7% lattice mismatch between InAs and GaAs. Initially higher value of surface energy of GaAs than that of InAs aids the formation of 2D InAs film which is known as the wetting layer. The driving force for the self-assembled QDs is the strain energy induced in the WL. The phase diagram of different strain relaxation mechanisms during InGaAs growth on GaAs(001) is shown as an example below (Heyn 2010).

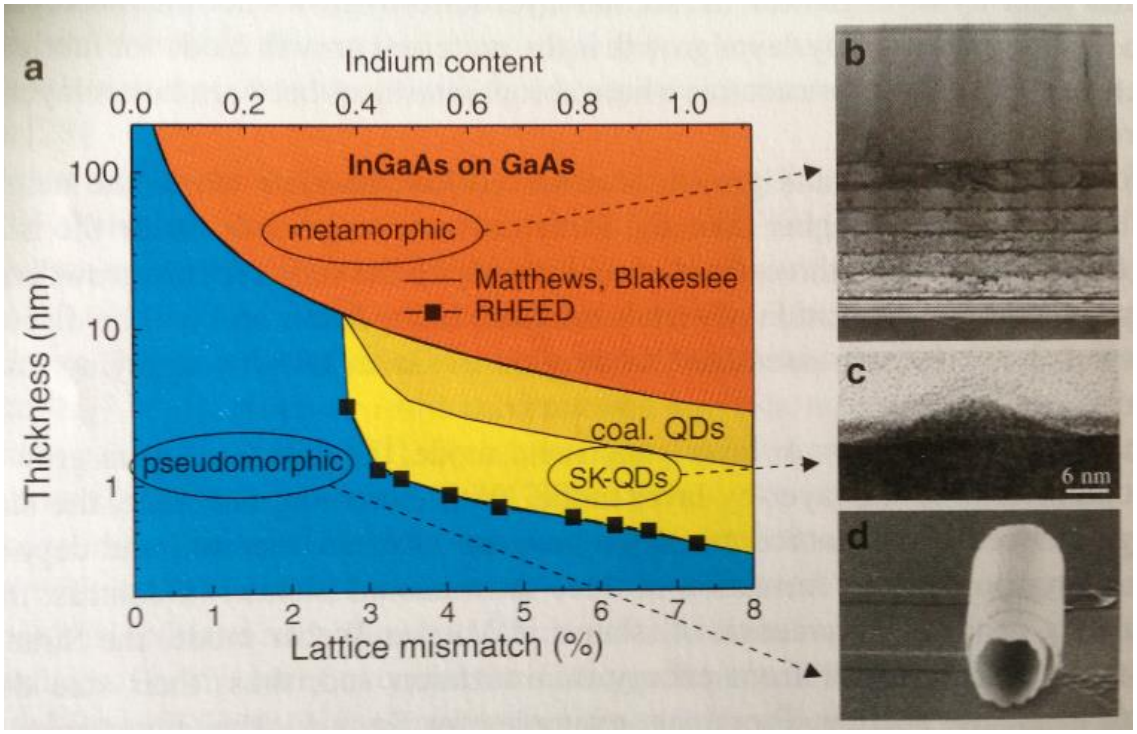

Figure 2.2: (a) Phase diagram of the strain status during $In_xGa_{(1-x)}As$ growth on GaAs(001) , TEM cross-section of (b) a metamorphic InAs HEMT, and (c) an InAs SK QD and (d) SEM image of a semiconductor nanotube . The figures are after Heyn, Springer (Heyn 2010). No scales provided in the original figures (b) and (d).

Thinner InGaAs films with low In content are pseudomorphically strained and are used in fabrication of semiconductor nanotubes utilizing a self-rolling mechanisms which is shown in Figure 2.2(d) (Kipp *et al.* 2006). As the films get thicker, dislocations are formed at the InGaAs/GaAs interface and are applied in fabrication of metamorphic buffers inside high-mobility InAs high electron mobility transistors (HEMTs) (Löhr *et al.* 2003). Stranski-Krastanov InAs QDs shown in Figure 2.2(c) are energetically favorable at higher In percentages (>40%) and an increase of the film thickness in this regime causes coalescence of QDs. Critical coverages for SK-QD formation are measured using RHEED oscillations and are indicated in solid squares in the Figure 2.2(a) (Heyn 2010). The onset

of dislocation formation is represented by the solid line and the calculations follow Matthews and Blakeslee (Matthews and Blakeslee 1974).

2.2.1 Wetting layer formation and critical thickness

InAs surface energy of 44 meV/Å^2 being less than the surface energy of GaAs (45 meV/Å^2), first a uniform InAs layer is formed which is known as the wetting layer (Pehlke *et al.* 1997) (Placidi *et al.* 2012). The surface energies and lattice parameters of InAs and GaAs materials are given in table 2.1.

In the absence of shear strain, the parallel ($\epsilon_{||}$) and perpendicular ($\epsilon_{\perp}$) strain components to the surface in a coherently grown layer are given by

$$\varepsilon_{||} = \frac{\left|a_{f||(\perp)} - a_{eq}\right|}{a_{eq}}, \tag{2.3}$$

where $a_{f||}$ and $a_{f(\perp)}$ are the in-plane and out-of-plane lattice parameters of the deformed cell and a_{eq} is the equilibrium lattice constant of the unstrained material. For a strained epilayer with small interface energy, initial growth is layer by layer. As the growth continues the layer gains a large strain energy and lowers its energy by forming islands in which strain is relaxed.

The critical thickness at which this islanding started to occur is

$$d_c = \frac{\Delta\gamma_{3D}}{(1-R)E\varepsilon^2/(1-\nu)}. \tag{2.4}$$

Table 2.1: Parameter values of the lattice constant, crystal structure and surface energy ($\gamma_{surface}$) (NSM 2015)

Semiconductor	Crystal Structure	Lattice Constance (Å)	$\gamma_{surface}$ (meV/Å^2)
InAs	Zinc Blend	6.0583	44
GaAs	Zinc Blend	5.6532	45
AlAs	Zinc Blend	5.6611	-

where $\Delta\gamma_{3D}$ is the surface energy cost per unit area due to the formation of a density n of 3D islands relaxing a fraction (1-*R*) of the strain energy of the film. *E* is the Young modulus and υ is the Poisson ratio. In the case of InAs/GaAs archetype system, calculations (Placidi *et al.* 2012) and experimental observations (Bute *et al.* 2008) (Tsukamoto *et al.* 2006) report that the critical thickness of equivalent InAs WL on GaAs occurs in the range of 1.5-1.7 ML.

Evolution of WL on GaAs(001) has been inspected by Honma *et al*. using a STMBE (Scanning Tunneling Microscope within MBE) at growth temperature 500^{0}C (Honma, Tsukamoto and Arakawa 2006). As seen in Figure 2.4 they obtained a uniform InAs surface at InAs coverage around 1 ML and above. The InAs 2D islands circled in Figure 2.3 indicate anisotropy in island dimensions which in relation to an anisotropy of the hopping barrier energy of In adatoms on a GaAs (001) surface.

An example of the growth temperature on wetting layer thickness was reported by Zhang H. *et al.* (Zhang, Chen, Zhou, *et al.* 2012) and the results are plotted in Figure 2.4. Open symbols indicates 2D growth and solid symbols are for 3D growth. At lower temperatures WL thickness increases first and then becomes saturated as the growth transforms to 3D. On the other hand, distinct concave up features of the WL evolution has

occurred for growths done at higher temperatures right after QD formation. This anomaly is associated to the generation of large QDs with dislocations and the enhance indium desorption.

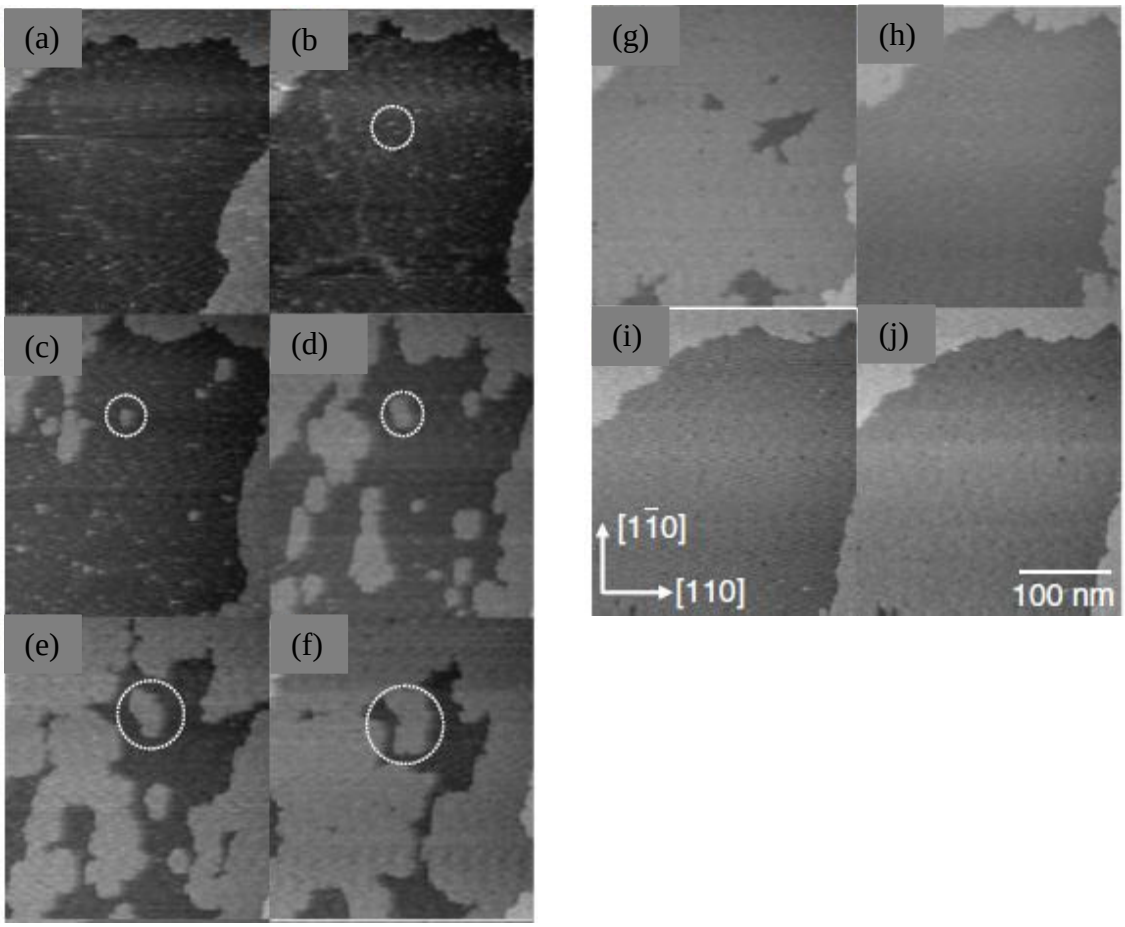

Figure 2.3 : STMBE images (horizontal scale 100nm) of WL evolution at equivalent InAs coverage of (a) 0 ML, (b) 0- 0.16 ML, (c) 0.16- 0.31 ML, (d) 0.31- 0.47 ML, (e) 0.47-0.63 ML, (f) 0.63-0.78 ML, (g) 0.78- 0.94 ML, (h) 0.94-1.09 ML, (i) 1.25- 1.41 ML and (j) 1.56-1.72 ML. The figure is after Honma *et al.*, Jpn. J. Appl. Phys. (Honma, Tsukamoto, and Arakawa 2006).

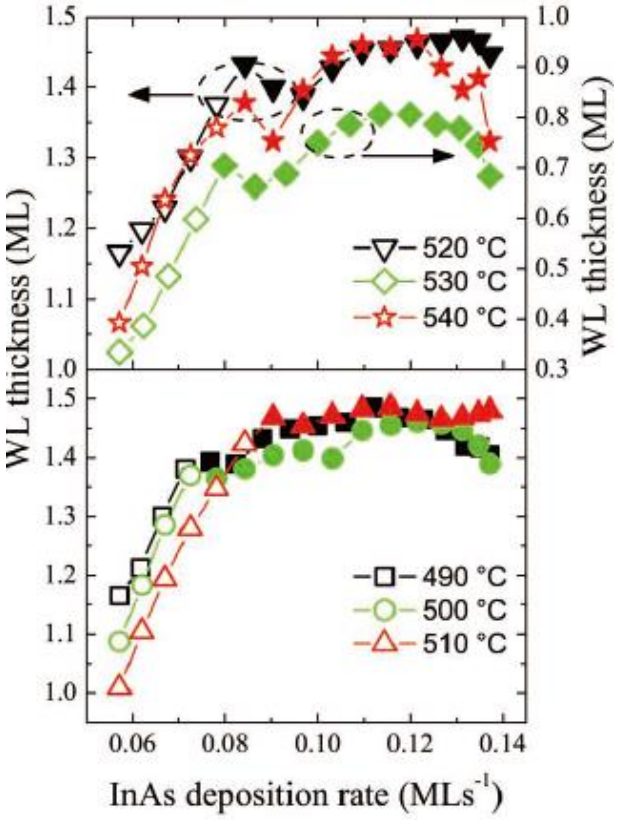

Figure 2.4: The InAs WL thickness evolution as a function of InAs deposition rate at different growth temperatures. The figure is after Zhang *et al*., Nanoscale Research Lett.(Zhang *et al.* 2012).

2.2.2 2D-3D transition: Evolution of surface morphology

Approaching the critical thickness (d_c) for 2D-3D transition (Equation 2.4, the surface morphology changes drastically and becomes very complex. At this critical coverage, the accommodated strain associated with the lattice mismatch starts relaxing by initiating the transition from a 2D surface to 3D islands in order to increase the number of atoms on the surface. The dependence of the density of 3D islands, ρ_D, to the InAs coverage, d, can be described in terms of a first-order phase transition (Bimberg, Grundmann, and Ledentsov 2001):

$$\rho_D = \rho_0(d - d_c)^{\alpha}, \tag{2.5}$$

where α is a fitting parameter and ρ_0 is the normalization density.

Surface morphology at different stages of InAs coverage show how the size distributions of 3D islands and 2D mounds evolve during transition regime [Figure 2.5]. At the very initial stages of the 2D-3D transition, the island distribution is bimodal with quasi-3D QDs and 3D QDs (Arciprete *et al.* 2006). Nucleation of dots occurs at the step edges of 2D islands and terraces due to a favorable strain condition at those sites.

With the increasing coverage, the family of quasi-3D QDs tends to disappear and convert into 3D QDs. As shown in Figure 2.6 starting from InAs equivalent coverage of 1.52 ML, the number of large QDs increase steadily and in the region 1.57 -1.61 ML it undergoes a sudden rise while the number of quasi-3D islands decreases. Hence, for the InAs/GaAs material system this 1.57-1.61 ML zone is considered as the transition range and 1.59 ML equivalent deposition is inferred as the critical thickness (Bute *et al.* 2008) (Placidi *et al*. 2012). The kinetics of this transition process is governed by the surface diffusion of adatoms which originate from steps present on the surfaces (Song *et al.* 2006). The surface-mediated mass transport can be due to intermixing which causes the increases of the substrate elastic strain, then relieved by atoms forming nucleation sites for 3D islands. The rate equations considering the mass transport between adatoms, 2D precursors and 3D QDs are based on the mean-filed approximation (Dobbs *et al.* 1997).

$$\frac{dn_1}{dt} = F - \beta n_1 - D(\sigma_2 n_2 + \sigma_3 n_3)n_1, \tag{2.6}$$

$$\frac{dn_2}{dt} = D\sigma_2 n_1 n_2 - \gamma n_2, \tag{2.7}$$

$$\frac{dn_3}{dt} = D\sigma_3 n_1 n_3 + \gamma n_2, \tag{2.8}$$

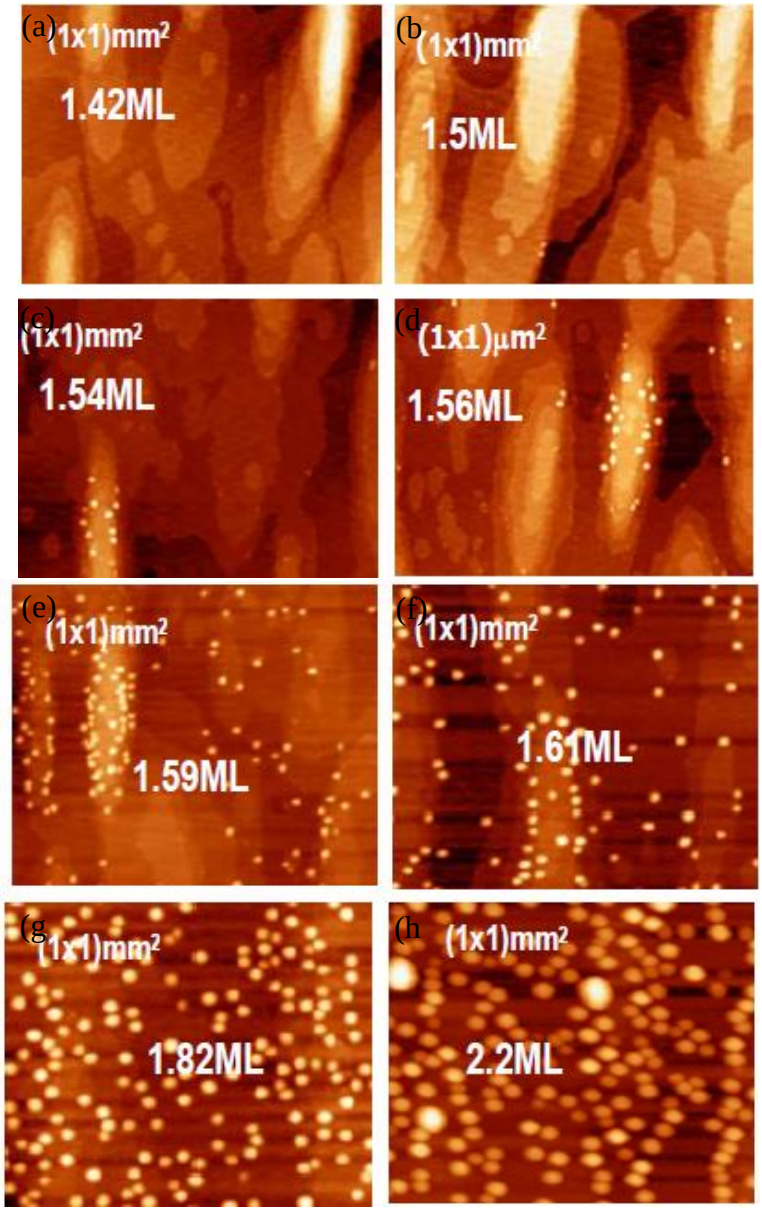

Figure 2.5: AFM topographies for InAs coverage of (a) 1.42 ML, (b) 1.5 ML, and (c) 1.54 ML,(d) 1.56 ML, (e) 1.59 ML, (f) 1.61 ML, (g) 1.82 ML and (h) 2.2 ML. The figure is after Bute *et al.*, J. Optoelectronics & Adv. Mat.(Bute *et al.* 2008).

where F is the InAs deposition rate, D is the diffusion coefficient of adatoms, and σ_2 and σ_3 are the normalized capture numbers for adatoms to be captured by the precursors and quantum dots, respectively. n_1, n_2 and n_3 are the amounts of adatoms, precursors, and quantum dots in terms of atoms or equivalent volumes in unit of ML. β is the attachment rate of adatoms to form pure two-dimensional wetting layer and γ is the nucleation rate of quantum dots.

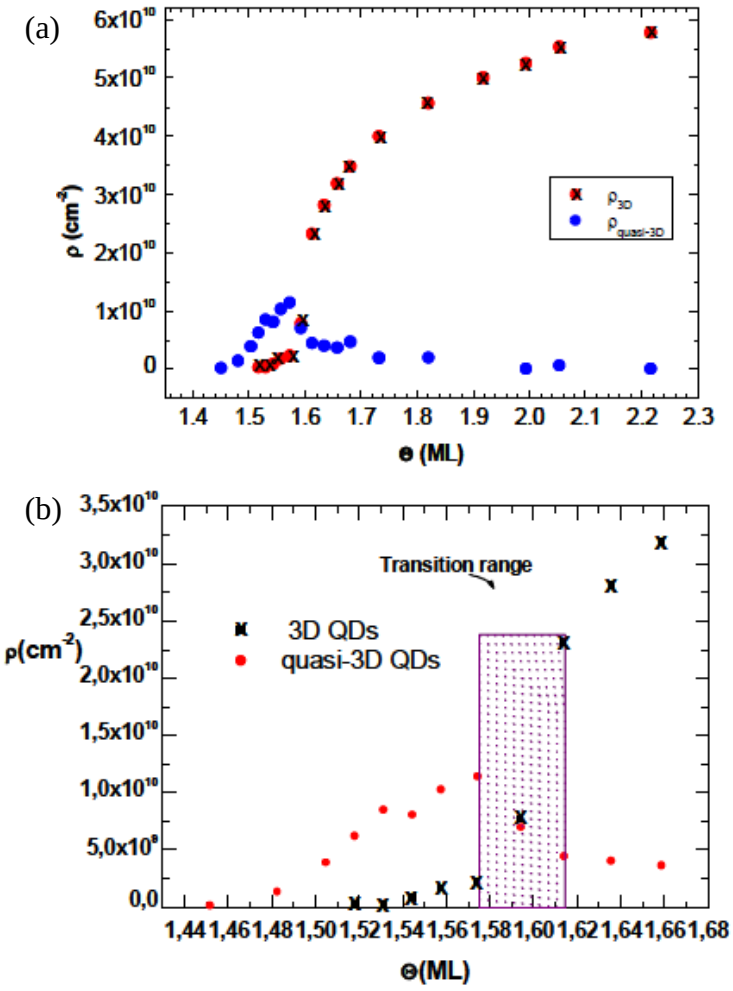

Figure 2.6: (a) Number density dependence of InAs coverage of small and large QDs extracted from the above AFM images in Figure 2.5 and (b) A close up of transition stage takes place at 1.59ML. The figure is after Bute *et al.*, J. Optoelectronics & Adv. Mat.(Bute *et al.* 2008).

2.2.3 3D phase: InAs SK QDs on GaAs (001)

Elastic relaxation of wetting layer at and beyond the critical limit leads two possible morphologies as shown in Figure 2.7: dislocated islands and coherent islands (Vanderbilt and Wickham 1991).

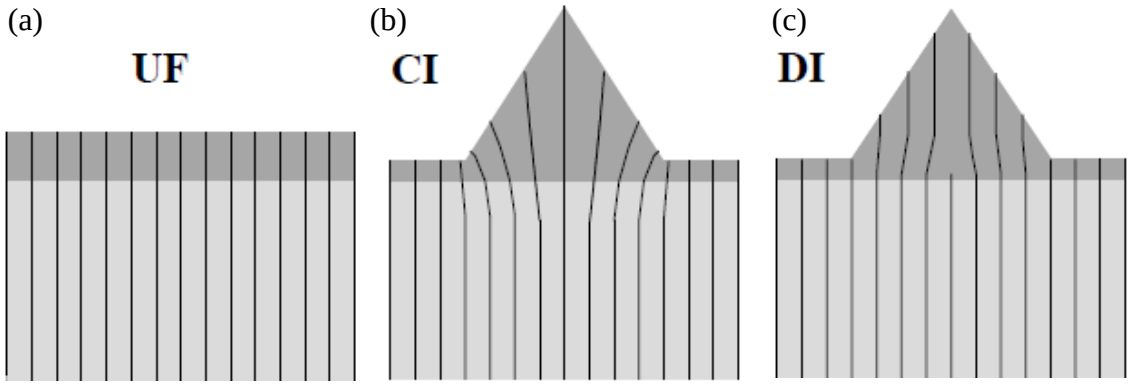

Figure 2.7: Schematics of strain relaxation during SK growth. (a) Uniform strained film (UF), (b) coherent strained islands (CI) and (c) Dislocated relaxed islands (DI) (Pehlke *et al.* 1997).

When a material is grown on a lattice-mismatched substrate, the elastic energy of a strained uniform film (UF) is given by

$$E_{UF} = c\varepsilon_0^2 V, \tag{2.9}$$

with c is the elastic constant, ε_0 is the epitaxial strain from equation 2.3 and V is the volume of the film.

The energy of the dislocated islands (DI) is given by the sum of excess energy $\gamma\Delta A$ and the island-substrate interface energy λA_0, which contains the energetical cost per area to create dislocations.

$$E_{DI} = \gamma\Delta A + \lambda A_0, \tag{2.10}$$

where γ is the surface energy, λ is the energy cost, and A is the surface area. For a sufficiently large film thickness, formation of dislocated islands are energetically preferable.

The change in morphology in coherent islands (CI) without any dislocations is driven by the gain in elastic relaxation energy (E_{el}) and thus the energy of CI becomes

$$E_{CI} = \gamma \Delta A + c\varepsilon_0^2 V - E_{el}, \tag{2.11}$$

The schematic diagram of these three energy configurations are shown in Figure 2.8. At increasing volume of an island, uniform film will be transformed to either coherent islands or dislocated islands depending on the interface/excess surface energy.

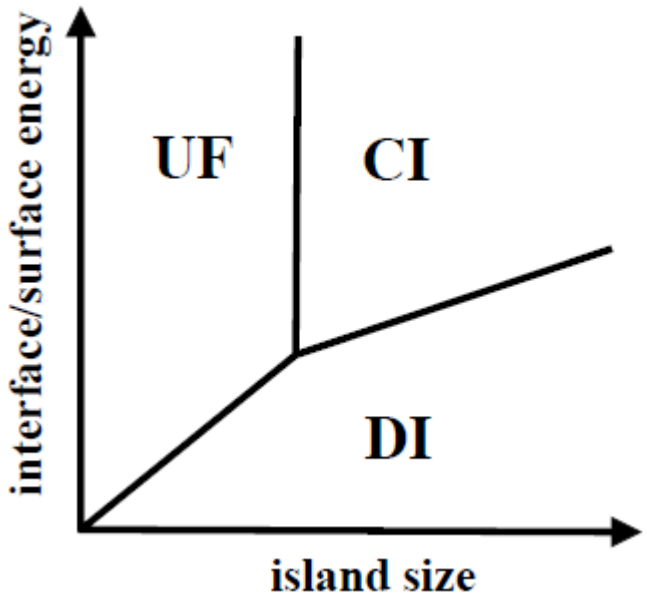

Figure 2.8: Schematic diagram showing the preferred morphology as a function of its volume and the ratio of interface to excess surface energy. The figure is after Pehlke *et al*., Appl. Physica A (Pehlke *et al.* 1997).

If the change of surface energy due to island formation is positive and small, coherent islands are formed and the change of the energy of the heterophase system is written as a balance of strain energy and surface energy according to the following equality (Shchukin *et al.* 1995) (Bimberg, Grundmann and Ledentsov 2001).

$$E_{island} = E_{edges} + \Delta E_{surface} - \Delta E^{V}_{relaxation}, \tag{2.12}$$

E_{edges} is the short-range energy of the island edges (Equation 2.13), $\Delta E_{surface}$ is the excess surface energy(Equation 2.14), and $-\Delta E^{V}_{relaxation}$ is the energy of elastic relaxation of the volume strain caused by lattice mismatch with the substrate (Equation 2.15). The scaling behavior of the energy terms are

$$E_{edges} = A_0 V^{1/3}, \tag{2.13}$$

$$\Delta E_{surface} = B_0 V^{2/3}, \tag{2.14}$$

$$\Delta E^{V}_{relaxation} = C_0 V . \tag{2.15}$$

where V is the volume of the island and A_0, B_0 and C_0 are shape-dependent scaling constants calculated within continuum elasticity theory and DFT. In the situations where the contribution of the surface energy dominates over the short-range edge energy, if the size of a three-dimensional island exceeds a critical size (= 2B/3C), further growth of the island becomes energetically favorable. When coherent islands with size larger than the critical value are formed, they undergo the phenomenon called Ostwald ripening. This process takes place to reduce the overall surface of the islands, thus reducing the total surface energy of the system (Ostwald 1900) (Arciprete *et al.* 2010).

At larger dot volumes, the elastic relaxation energy in Equation 2.15 becomes shape dominating energy term and it is the difference between the remaining bulk strain energy stored in the island plus the substrate after relaxation; hence the term is treated within classical continuum elasticity (CE) theory.

In CE approach the strain energy per atom (E_{CE}) in a cubic system is given by (Landau and Lifshitz 1975)

$$\Delta E^{V}_{relaxation} = E_{CE} = \frac{V}{2}C_{11}\left(\varepsilon_{xx}^2 + \varepsilon_{yy}^2 + \varepsilon_{zz}^2\right) + \frac{V}{2}C_{44}\left(\varepsilon_{yz}^2 + \varepsilon_{zx}^2 + \varepsilon_{xy}^2\right) + VC_{12}\left(\varepsilon_{yy}\varepsilon_{zz} + \varepsilon_{zz}\varepsilon_{xx} + \varepsilon_{xx}\varepsilon_{yy}\right), \quad (2.16)$$

where V is the equilibrium volume, $C_{\alpha\beta}$ are cubic elastic constants, and ε_{ij} is the strain tensor related to the displacement u_i given by the relation

$$\varepsilon_{ij} = \frac{1}{2}\left(\frac{\partial u_i}{\partial x_j} + \frac{\partial u_j}{\partial x_i}\right), \quad (2.17)$$

The total stresses σ_{ij} for arbitrary material are related to the strains ε_{ij} as follows

$$\sigma_{ij} = C_{ijkl}\varepsilon_{kl}. \quad (2.18)$$

For materials with cubic symmetry only three of the elastic constants components are independent. They are $C_{11} = C_{1111} = C_{2222} = C_{3333}$, $C_{12} = C_{1122} = C_{2233} = C_{3311}$ and $C_{44} = C_{1212} = C_{2323}$ etc.

The boundary condition for the formation of dots is the free elastic stresses along (001) growth direction (σ_{zz}) on the surface. Then Equation 1.8 becomes

$$\sigma_{zz} = C_{12}\,\varepsilon_{xx} + C_{12}\,\varepsilon_{yy} + C_{11}\,\varepsilon_{zz} = 0, \tag{2.19}$$

Hence for a 2D film which is constrained on a (001) substrate, the relaxation of under biaxial strain predicts

$$\frac{\varepsilon_{\perp}}{\varepsilon_{\parallel}} = \frac{\varepsilon_{zz}}{\varepsilon_{xx}} = -\frac{2C_{12}}{C_{11}}, \tag{2.20}$$

where $\varepsilon_{xx} = \varepsilon_{yy}$ in cubic systems.

2.3 Equilibrium InAs/ GaAs (001) QD structures & shape transition

The theoretical calculations discussed above have been applied to construct the equilibrium QD shapes at different growth stages along with the use of experimental observations (Xu *et al.* 2005)(Kratzer *et al.* 2006).

It has shown from the calculations in Kratzer *et al.* that the relaxation term in Equation 2.12 is an energy gain; i.e. the islands stabilize themselves by strain relief compared to the homogeneously strained film. $\Delta E^{V}_{relaxation}$ being a volume effect, ultimately becomes dominant for the larger QDs.

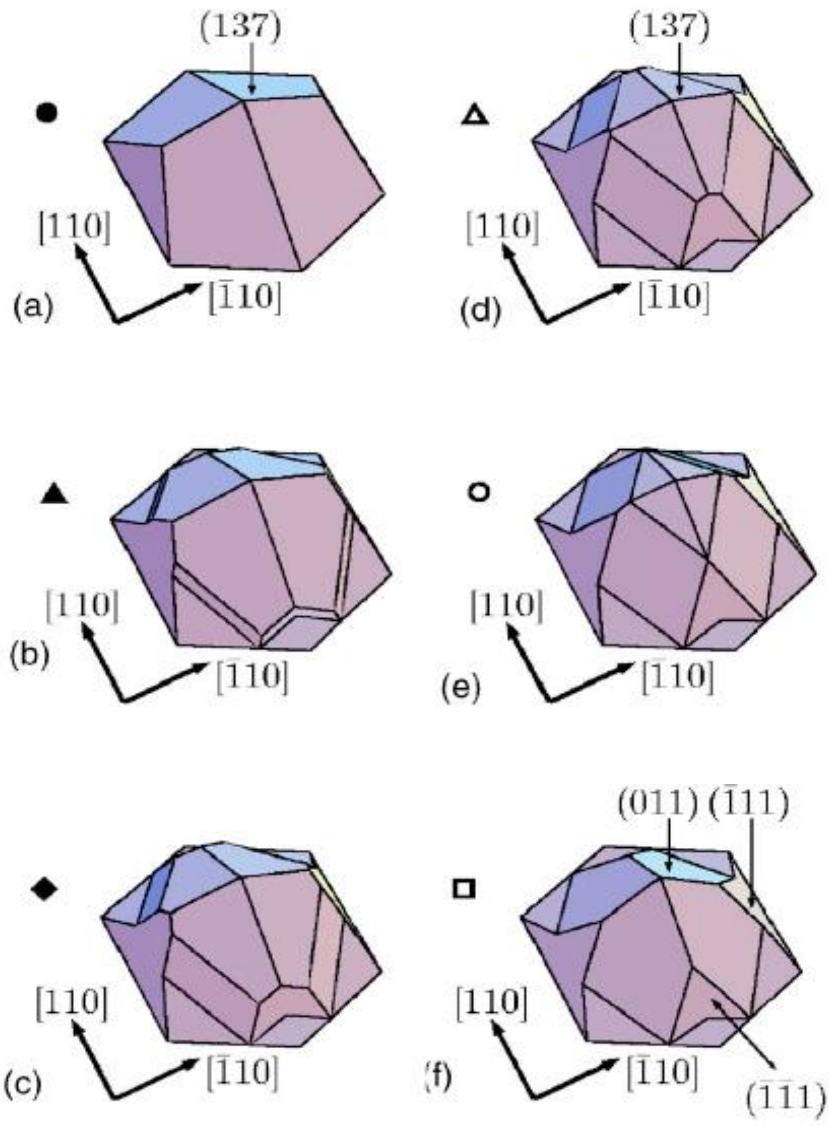

Figure 2.9: (a)-(f) Calculated shapes for the growth of InAs QDs on GaAs (001) during ripening. The figure is after Kratzer *et al*., Phys. Rev. B (Kratzer *et al.* 2006).

Smaller shallower islands are pyramidal in shape and the facets are found to be of the family of {1 3 7} facets (Figure 2.9(a)) which are energetically favorable due its low cost

in terms of surface energy. The shallow {1 3 7} side facets increase the surface area only moderately compared to the base area of the QD.

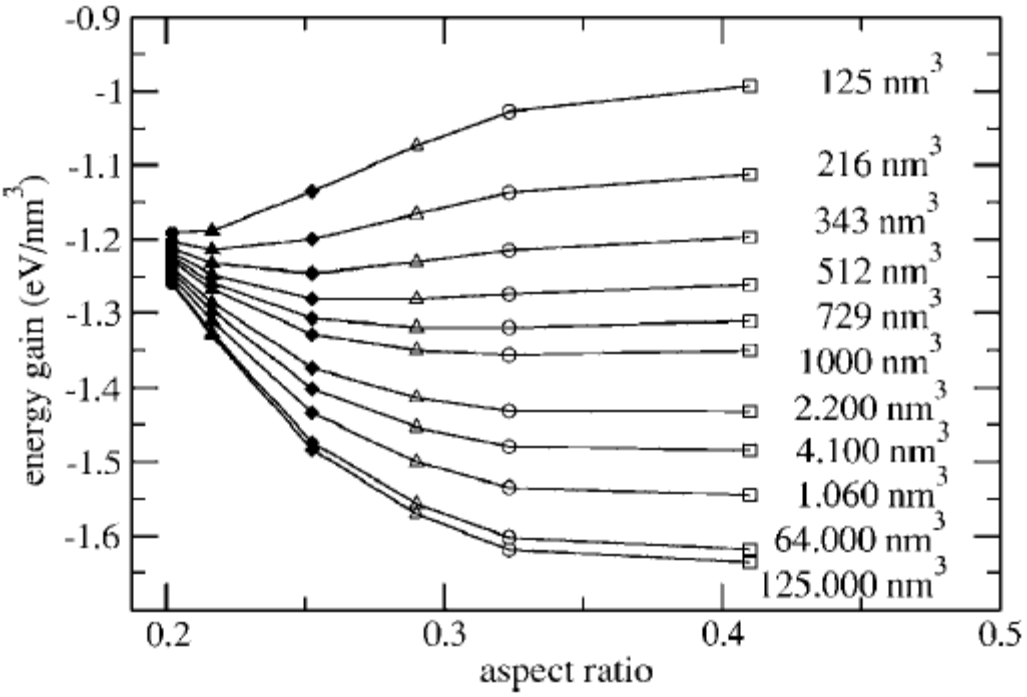

Figure 2.10: Calculated energy gain per unit volume for quantum dot formed from a given amount of material (no specific shape is considered). On the abscissa, the shapes displayed in Figure 2.9 are represented by their aspect ratio (height: base diameter). The figure is after Kratzer *et al*., Phys. Rev. B (Kratzer *et al.* 2006).

Moreover, the high surface strain on these facets lower their surface energies considerably. Further the calculation of energy gain per unit volume for different volumes corresponds to different shapes (in terms of aspect ratio) in Figure 2.10 concludes that the smaller volumes are preferred to have minimum energy for the flat pyramidal shape which in this case {1 3 7} facet-bounded structures.

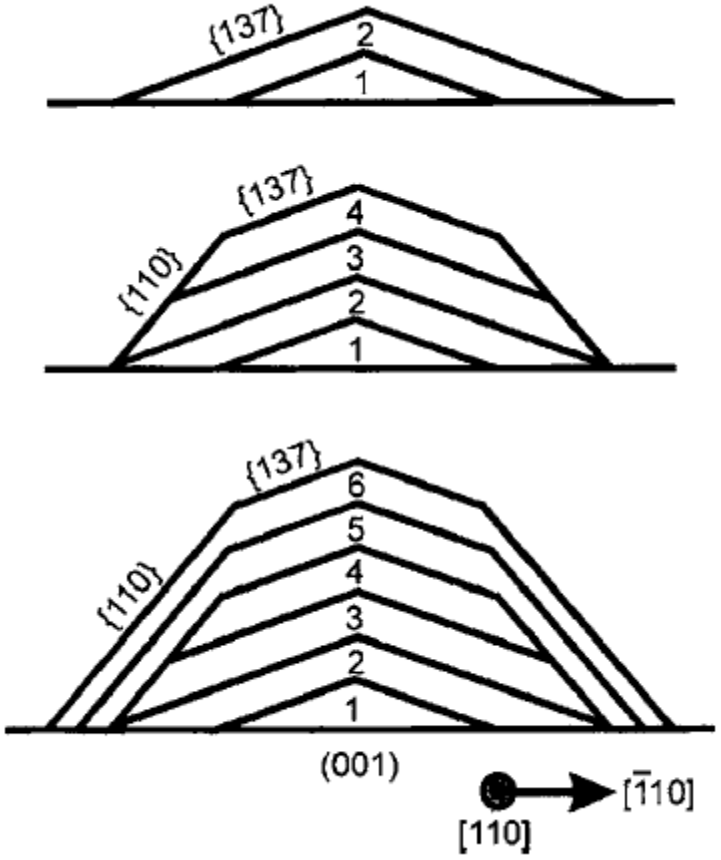

Figure 2.11: Schematic growth model for addition of dot facets during growth. The figure is after Xu *et al*., J. Appl. Phys. (Xu *et al.* 2005).

As the island grows the additional {1 3 7} layers are stacked on top of the existing planes creating low index {1 1 0} facets at the edges as explained in Figure 2.11. Later in the growth process an intermediate symmetric dot with octagonal base appears with all edges replaced by {1 1 0}, {1 1 1}*A* and {$\overline{1\ 1\ 1}$}*B* facets. According to Figure 2.10, quantum dots with volumes larger than 1000 nm^3 are found to be favorable having steeper facet with higher aspect ratio. More efficient strain relaxation in these steeper planes give rise to a thermodynamic driving force for developing a domelike shape on top of a flat base as the island grows larger.

Further growth may cause dislocations in the system leading to irregular shapes. Small shallower $\{\bar{1}\,3\,5\}$ and $\{\bar{1}\,1\,2\}$ facets have not included in these proposed structures. A detailed description on the presence of these facets will be presented in later sections.

2.4 Summary

In this chapter the growth kinetics of self-assembled Stranski-Krastanov InAs/GaAs(001) QDs is described based on strain relaxation and surface energies in the heteroepitaxial layers. The three phases of growth process are reviewed. The 2D phase shows the experimental and theoretical calculations of WL critical thickness which is in the range of 1.5-1.7ML. The surface morphological changes during the transition between layer growth and island nucleation are explained using surface-mediated mass transport by mean-field approximation.

The balance between excess surface free energy, elastic relaxation energy, and short-range energy of the island edges determines the equilibrium dot shapes (facet configurations) at different dot volumes. At initial growth stages $\{1\,3\,7\}A$ facets are found to be the favorable bounded dot shape and as the dot grows steeper facets such as $\{1\,1\,0\}$, $\{1\,1\,1\}A$ and $\overline{\{1\,1\,1\}}B$ are formed to minimize the effect from higher strain energy accumulates in the quantum dot.

Chapter 3

Molecular Beam Epitaxy (MBE) and MBE-grown QD Properties

This chapter is focused on the morphological behavior of GaAs surfaces which are grown using molecular beam epitaxy (MBE). The first section (3.1) reports the effects of group III and group V flux ratio in formation of different surface reconstructions. Adsorption and desorption of Ga and As_2 atoms are used to investigate the kinetics of GaAs growth in Section 3.2. In Section 3.3 a schematic of MBE growth chamber is included and the calculations of variation of flux deposited on a substrate are also presented. In the final section which is Section 3.4 structural properties of MBE-grown InAs SKQDs are discussed.

3.1 Morphology of epitaxial growth by MBE

In the late 1960's , Alfred Y. Cho together with John Arthur, pioneered in the invention of molecular beam epitaxy (MBE) technique as a layer growth process involving the reaction of thermal molecular or atomic beams on a crystalline surface at ultrahigh vacuum conditions ($x10^{10}$ torr) (Cho and Arthur 1975)(Parker 1985). Precise positioning of matrix and dopant atoms in layered structures can be attributed by molecular beam epitaxy and hence well-defined structures and atomically clean surfaces in different crystallographic orientations.

During layer deposition, the surface structure is one of the important aspect of high quality MBE growth under ultrahigh vacuum conditions with very close control of individual fluxes (Joyce 1981). Most of the preliminary investigations on this character have been carried out for GaAs growth on GaAs substrates with different growth planes. In 1969, A. Y. Cho used an *in-situ* approach to configure morphology of homoepitaxial GaAs ($\overline{1}\,\overline{1}\,\overline{1}$) films by molecular beam method in an ultra-high vacuum high-energy electron diffraction (HEED) system (Cho 1970). Elongated diffraction spots for surfaces which are not atomically flat and streak patterns for smoother surfaces were observed at different growth temperatures. Surface structures of GaAs grown on GaAs($\overline{1}\,\overline{1}\,\overline{1}$) formed arsenic rich and gallium rich reconstructed surfaces at a transition temperature and the conversion between structures is also a function of the Ga and As_2 deposition rates. These transition characteristics between the surface structures revealed that the relative stability of one or the other structure depends upon the relative population of adsorbed Ga and As atoms on the surface. Section 3.1.1 describes different surface reconstructions on GaAs

(001) surfaces. Further details on Ga and As_2 interactions with GaAs will be explained in later sections.

Heteroepitaxy creates a variety of topographical defects, such as pyramids, mounds, dislocation lines, and dendrites. Residual surface contamination or induced strain relaxation are usually the cause for pyramids and mounds. Dislocation lines are usually caused by stress produced in lattice mismatched layers (Cho 1970). In this work we mainly focus on pyramidal-shaped islands which are also known as quantum dots.

3.1.1 Surface reconstruction

The atomic structure of the GaAs (001) surface is significantly important because most of the GaAs devices are fabricated on (001) plane. Different reconstructions such as (2X4), (4X4) and (2X8) surfaces have been observed on GaAs(001) by scanning tunneling microscopy (STM) as a function of stoichiometry (Biegelsen *et al.* 1990) and the conversion between the surfaces are found to be a function of crystal temperature and [As]/[Ga] flux ratio (Cho 1970) (Arthur 1974). GaAs(001)- 2X4 surface is of utmost technological importance within the family of zinc blend III-V semiconductors. The phases γ, β, and α are obtainable under different growth conditions (Farrell 1990). Low crystal temperature and/or relatively high As/Ga ratio which is referred as As rich condition produce α or $\beta 2$ phases (2X4) structures and high crystal temperature and/or low flux ratio create Ga stabilized ζ(4X2) stoichiometric reconstruction (Schmidt, Bechstedt and Bernholc 2002) (Labella *et al.* 1999).

The thermodynamic stability of these surface reconstruction as a function of Ga chemical potential (μ_{Ga}) has been calculated for zero temperature condition by Northrup

and Froyen, Phys. Rev. Lett. (Northrup and Froyen 1993). Figure 3.1 shows the calculated phase diagram for the energetically relevant surface structures of GaAs(001).

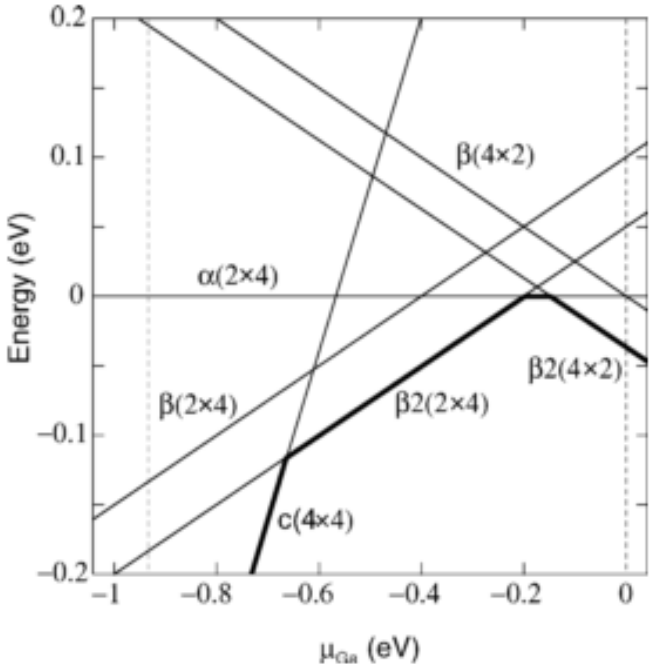

Figure 3.1: Formation energy for a (1x1) unit cell for GaAs (001) surfaces as a function of μ_{Ga}. The emboldened line indicates the equilibrium phases. The figure is after Northrup and Froyen, Phys. Rev. Lett. (Northrup and Froyen 1993).

For extremely arsenic-rich situations with high μ_{As} (low μ_{Ga}), a *c*(4X4) phase which corresponds to the formation of three-dimer blocks of As on top of an As-terminated substrate is stable (Joyce and Vvedensky 2004). ζ(4X2) phase is formed under rich Ga condition with low μ_{As} and the schematics of these two phases are exhibited in Figure 3.2.

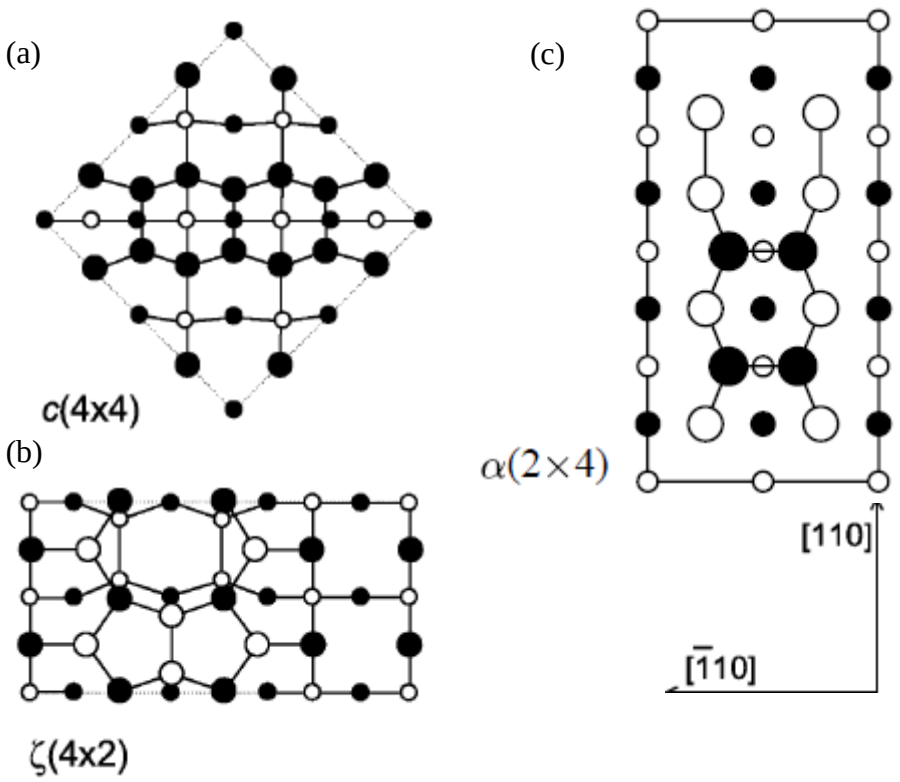

Figure 3.2: Top view of relaxed GaAs(001) surface structures (a) *c*(4x4), and (b) ζ(4X2). The figure is after Schmidt *et al*. Appl. Surf. Sci. (Schmidt *et al.* 2002). (c) Proposed structure for *α*(2x4) surface. The figure is after Labella *et al*. Phys. Rev. Lett. (Labella *et al.* 1999). Empty (filled) circles represent Ga(As) atoms. Uppermost atoms are indicated by larger symbols.

*β*2(2X4) phase is the most likely structure for moderately As terminated surfaces (at intermediate μ_{As} levels) and both α and *β*2 structures are found to have the lowest formation energy and *β*2 is the most favorable. The structure of *β*2 phase has a top layer with two As dimers and two missing As dimers. The second layer Ga atoms lying beneath the two missing As dimers are also missing, and the exposed third layer As atoms themselves dimerize (Joyce and Vvedensky 2004). Calculations of these trenches and dimer rows are shown in figure 3.3 (Labella *et al.* 1999) while Figure 3.4 reveals a detailed geometry of

As and Ga atomic positioning of first few top most layers. The light and dark bands represents dimer blocks and trenches respectively.

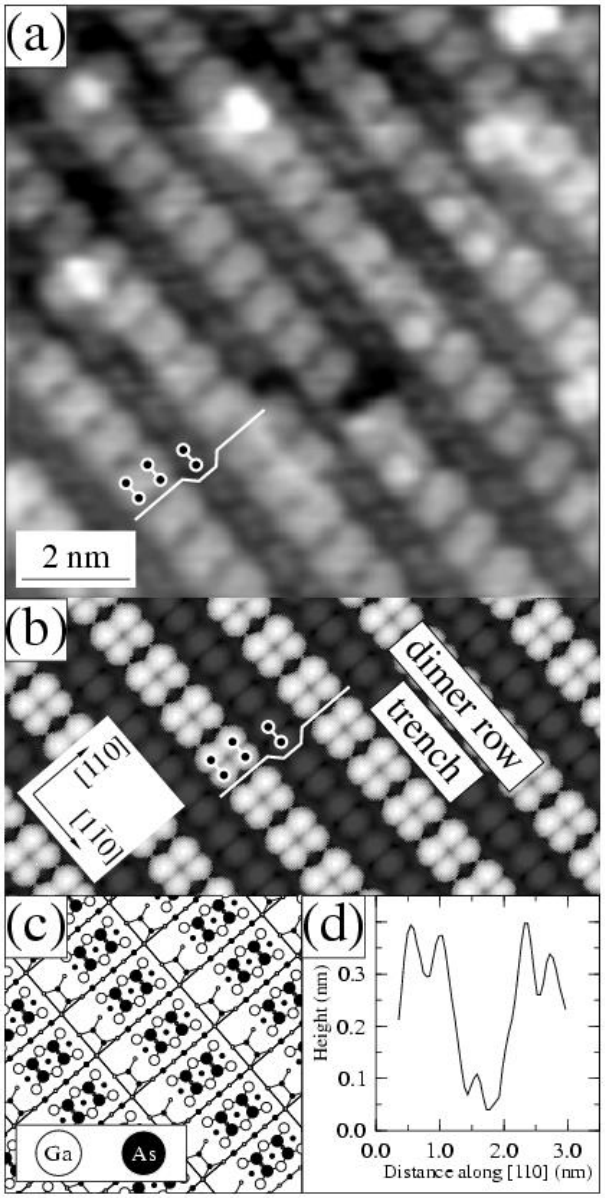

Figure 3.3: (a) Filled state STM image (b) simulate STM image of β2 phase (c) structural model and (d) height cross section across a dimer trench along the [1 1 0] direction. The figure is after Labella *et al*. Phys. Rev. Lett. (Labella *et al.* 1999).

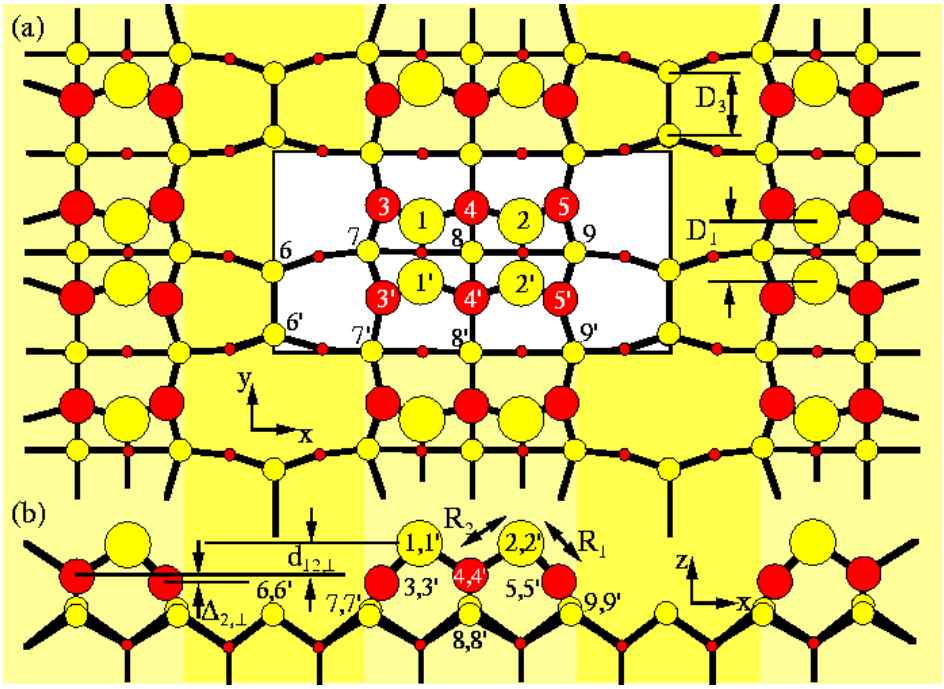

Figure3.4: Relaxed geometry of the GaAs(001)-β2(2X4) surface: (a) top view, and (b) the x-z side view. The dark and light shaded bands highlight the trenches and the dimer blocks, respectively. Yellow circles represent As atoms and Red circles represent Ga atoms. The figure is after Srivastava & Jenkins, Phys. Rev. B (Srivastava and Jenkins 1996).

The atomic geometry above is computed by Srivastava and Jenkins using *ab initio* pseudopotential calculations and equilibrium bond lengths are given in Table 3.1.

Table 3.1: Atomic positions of β2(2X4) reconstructed As and Ga atoms. The values are in angstrom (Å). The table is after Srivastava & Jenkins, Phys. Rev. B (Srivastava and Jenkins 1996).

D_1	D_2	$d_{12,\perp}$	$\Delta_{2,\perp}$	R_1	R_2
2.39	2.50	1.26	0.30	2.28	2.42

3.2 Growth mechanisms of GaAs

In MBE, Group III atomic beams impinge on the heated substrate surface, migrate into the appropriate lattice sites, and deposit epitaxially in the presence of excess Group V molecular beams.

The reaction of Ga and As_2 on GaAs is a first-order dissociative chemisorption of As_2 molecules on single Ga atoms. This mechanism is illustrated in Figure 3.5. Kinetics of this reaction is described in two processes: Adsorption and desorption.

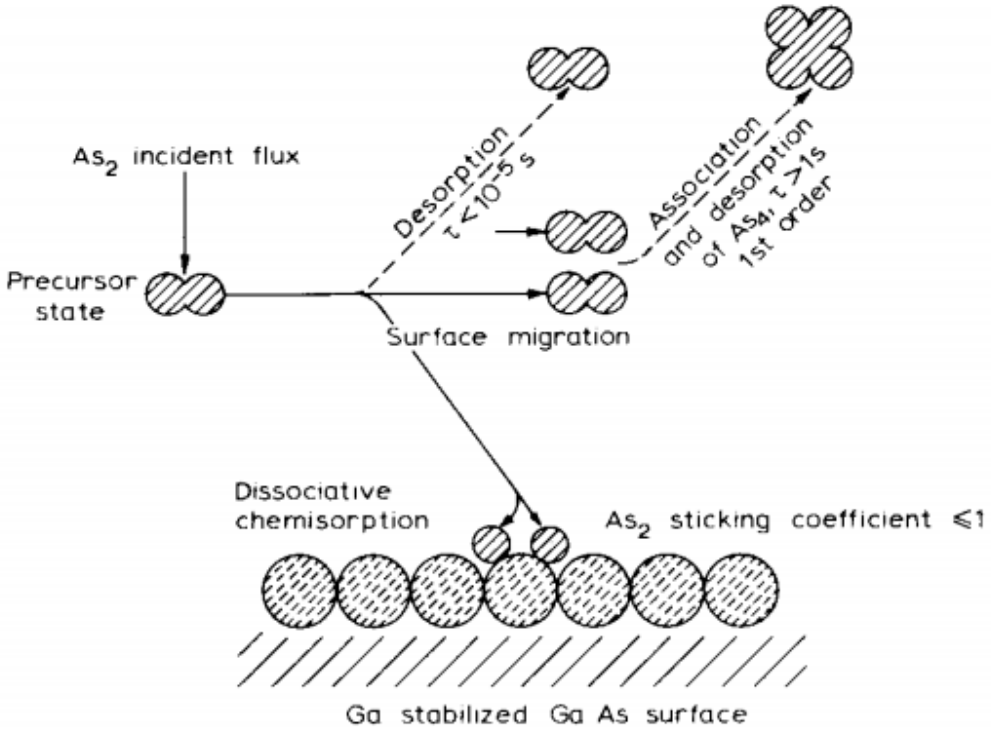

Figure 3.5: Incorporation of As atoms on a GaAs(001) surface from impinging As_2 The figure is after Foxon, JVST B (Foxon 1983).

3.2.1 Adsorption:

The first study on interaction of Ga and As2 molecular beams with GaAs(111) surface was described by J. R. Arthur in 1968 (Arthur 1968). According to the investigation, in order to grow GaAs it is necessary to supply gallium and arsenic vapors in such a ratio that the rate of collisions between adsorbed Ga and impinging arsenic vapor is equal to the arrival rate of Ga. The observations suggest that Ga atoms dominates the growth of GaAs layers at elevated temperatures and the sticking coefficient of Ga on GaAs is accounted to be unity. Therefore, Ga atoms are necessary for As_2 atoms to adsorb on GaAs and adsorbed Ga atoms strongly modify the adsorption rate of As_2. This effect provides a kinetic mechanism for the growth of stoichiometric GaAs layers from Ga and As vapor (Arthur 1968).

Dissociative adsorption of arsenic atoms are considered to follow the reaction sequence (Arthur 1974)

$$As_{2(g)} \rightleftharpoons As_2^*, \tag{3.1}$$

$$As_2^* + 2V_{(As)}^* \rightleftharpoons 2\,As_{(As)}^*, \tag{3.2}$$

As_2 molecules are first adsorbed into mobile, weakly bound precursor states and the reaction is expressed in Equation 3.1. Equation 3.2 indicates the dissociation of those adsorbed As_2 into paired empty As sites. Note: asterisks represent surface species. $V_{(As)}^*$ is a vacant As site at the surface and $As_{(As)}^*$ is filled As site.

The sticking coefficient for the above series of reactions is derived to be

$$S = \frac{k\tau(1-\theta)^2}{1+k\tau(1-\theta)^2}, \tag{3.3}$$

where τ is the mean surface life time of As_2^*, θ is the fraction of surface arsenic sites which are filled, and *k* is the rate constant for dissociation.

3.2.2 Desorption

For a first-order desorption process of Ga on GaAs the surface lifetime τ, the ad-atom concentration *n* and the desorption rate Γ are related by (Cho and Arthur 1975)

$$\Gamma = \frac{n}{\tau}, \tag{3.4}$$

If a beam of atoms of intensity F incident on the surface, then the rate of change of ad-atom concentration becomes

$$\dot{n} = -\frac{n}{\tau} + F. \tag{3.5}$$

The integration of the above equation yield the desorption rate to be

$$\Gamma(t) = F\left(1 - e^{-\frac{t}{\tau}}\right), \tag{3.6}$$

with the initial condition $n(0) = 0$ and with the assumption of $\tau \neq f(n)$

When the beam is shut off abruptly, desorption is expressed as a function of temperature (T) ,the activation energy E_a and Boltzmann constant K_B (Enrlich 1956).

$$\tau = \tau_0 \exp\left(\frac{E_a}{K_B T}\right). \tag{3.7}$$

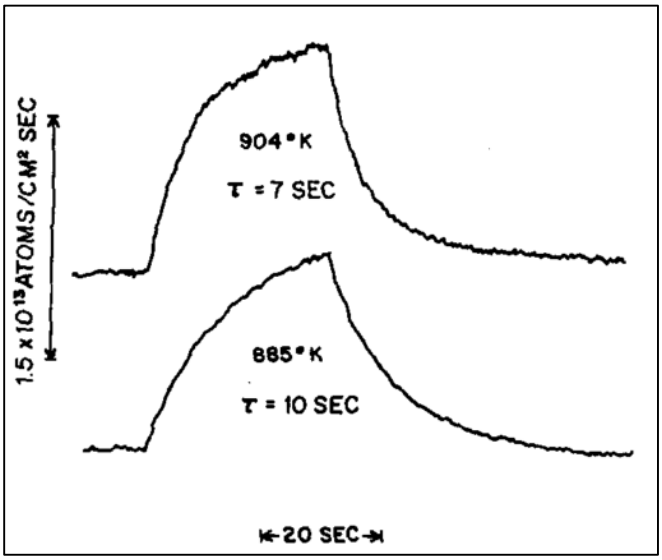

Figure 3.6: Reflected Ga pulse from GaAs(1 1 1) at 904 K and 885 K. The figure is after Arthur, J. Appl. Phys. (Arthur 1968).

As_2 atoms on GaAs however do not desorb according to Equation 3.7. Periodically interrupted beam of As_2 was used to determine the flux of As_2 desorbed from GaAs in Cho & Arthur (1975). The first two pulses indicate the As_2 flux on clean, heated GaAs and the third pulse represents the desorption flux of As_2 on Ga-covered GaAs. Comparison of short life times of first two pulses and considerable lifetime of third pulse suggests that the As_2 desorption takes place along only with the consumption of adsorbed Ga. According to the reverse reactions shown in Equations 3.1 and 3.2, recombination of As atoms to molecules at elevated temperatures may succeed desorption of arsenic.

The rate of change of population of adsorbed As_2^* ,$\dot{n}$, and is then

$$\dot{n} = F - \frac{n}{\tau} - kn(1-\theta)^2 + A\theta^x \exp(B\theta), \tag{3.8}$$

where *A*, *x*, and *B* are rate constant, recombination reaction order and coverage coefficient of the binding energy respectively

.

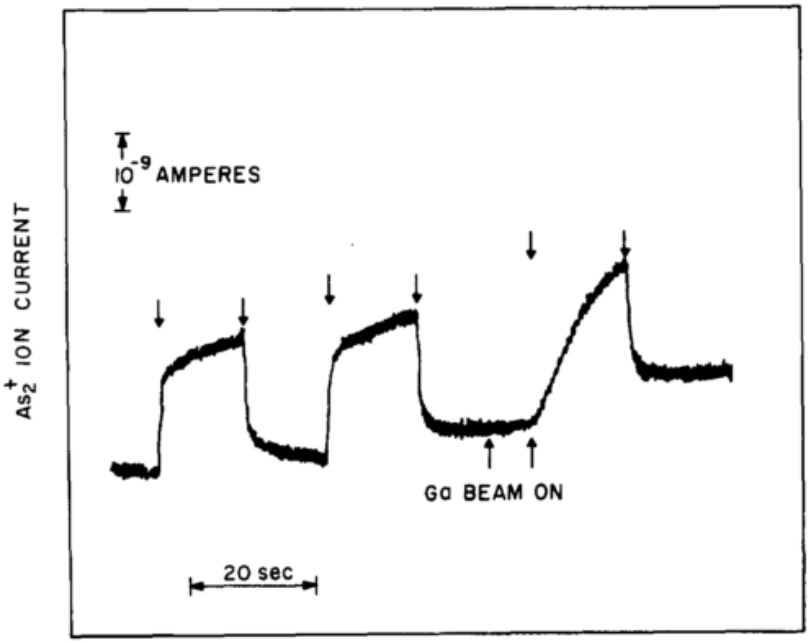

Figure 3.7: Desorbed pulse shapes from incident rectangular pulses of As_2 on GaAs(111): prior to third As_2 pulse ~0.5ML Ga has deposited during indicated period. The figure is after Cho & Arthur, Progress in solid state Chem. (Cho and Arthur 1975).

Then the rate of change of fractional coverage of dissociated arsenic $\dot{\theta}$, with n_0 being the density of As sites, takes the form

$$n_0\dot{\theta} = 2\{kn(1-\theta)^2 - A[\theta^x \exp(B\theta) - 1]\}, \tag{3.9}$$

Assuming steady state conditions for As_2^* , the rate of desorption of As_2 is derived as

$$\frac{n}{\tau} = (1-S)[F + A\theta^x \exp(B\theta)] \tag{3.10}$$

while the rate of change of θ is demonstrated as

$$n_0\dot{\theta} = 2\{A - (1 - S)[F + A\theta^x \exp(B\theta)]\} \tag{3.11}$$

Sticking coefficient S is displayed in Equation 3.3 and since it is a temperature dependent, two conditions can be discussed for low and high temperature limits.

Based on experimental observations (Arthur 1974), A is negligible for low temperatures and hence Equations 3.10 and 3.11 transform to

$$\frac{n}{\tau} = F(1 - S), \tag{3.12}$$

and

$$n_0\dot{\theta} = 2FS, \tag{3.13}$$

At higher temperatures, θ will reach a steady state value ($\dot{\theta} = 0$) due to rapid desorption and absence of As_2 flux. Then both the Equations 3.12 and 3.13 form one equation

$$\frac{n}{\tau} = A, \tag{3.14}$$

which can be interpreted as desorption rate is equal to decomposition rate.

3.3 MBE apparatus and technique

MBE is the simplest method of growing epitaxial films of semiconducting materials in terms of physical principles involved and it is a highly controlled ultra-high vacuum (UHV) process. Control over thickness and possibility of fabricating semiconductor heterostructures with monolayer abruptness are the advantages of this mature growth technique. MBE employs atomic beams such as Al, Ga, and In and molecular beams such as As_4 and P_4. The reactants are generated inside the growth chamber by evaporation at high temperatures from solid elemental sources. Group III elements are provided in terms of atomic beams and group V elements are from the decomposition of hydrides such as arsine (AsH_3) and phosphine (PH_3) which cracks into As_2, P_2, and H_2 (Frood, Davies, and Tsang 1997). A schematic of a UHV MBE chamber is illustrated below in Figure 3.8.

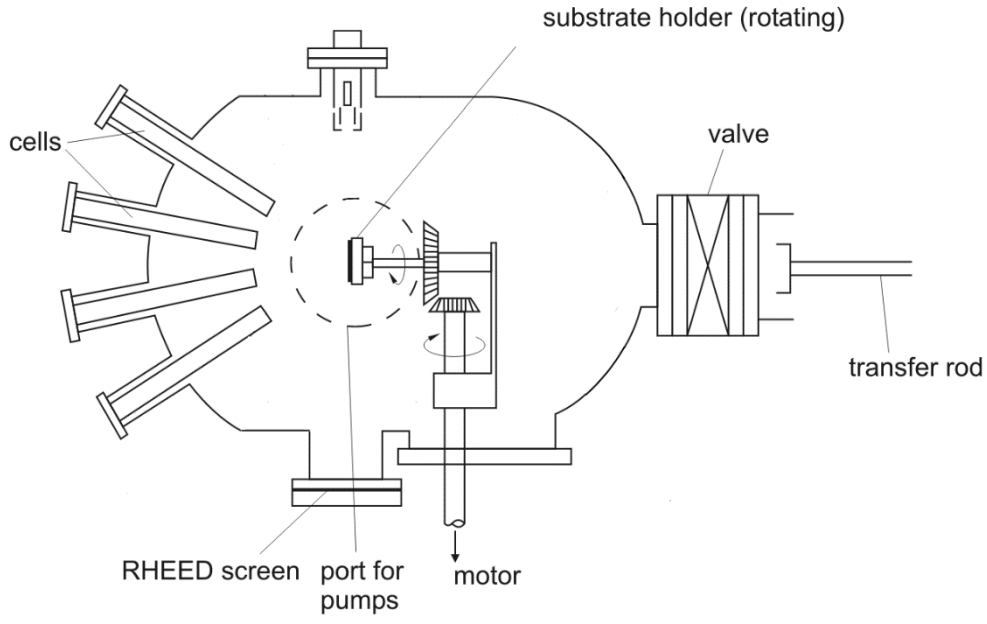

Figure 3.8: Schematic of a MBE chamber.

The solid sources of MBE are Knudsen effusion cells which provides an angular distribution of atomic or molecular beams. Collision-free molecular flow is ensured if the pressure of vapor in the cell is such that its mean free path is greater than the orifice diameter. According to the kinetic theory of gases the mean free path λ between collisions of atoms or molecules at a pressure *p* is given by

$$\lambda = \frac{k_B T}{\sqrt{2}\pi p D^2}\,, \tag{3.15}$$

where *D* is the diameter of atoms or molecules and *T* is the cell temperature. The flux of particles F_e effusing from an orifice with a mass m under the equilibrium conditions established between the vapor and condensed phase is (Cho 1970) (Langmuir 1913)

$$F_e = p_{eq}(T).a\sqrt{\frac{N_A}{2\pi m k_B T}}\frac{molecule}{cm^2}.s\,, \tag{3.16}$$

where *a* is the orifice area (cm^2), L is the distance to the substrate (cm) and $p_{eq}(T)$ is the equilibrium pressure (Torr) which is expressed by the Clausius–Clapeyron relation

$$p_{eq}(T) = A\exp\left(\frac{-\Delta H}{k_B T}\right), \tag{3.17}$$

where ΔH, k, N_A, and A are enthalpy of vaporization, Boltzmann constant, Avogadro's constant, and a parameter constant respectively.

The intensity distribution from an aperture is assumed to be a point source follows the Lambertian cosine law (Joyce 1981). The flux F that reaches a point P on a substrate situated at a distance r_p following a path at an angle (θ + φ) with the substrate axis (Franchi 2013).

$$F = \frac{F_e}{\pi}\frac{1}{r_p^2} cos\theta \cos(\theta + \varphi), \qquad (3.18)$$

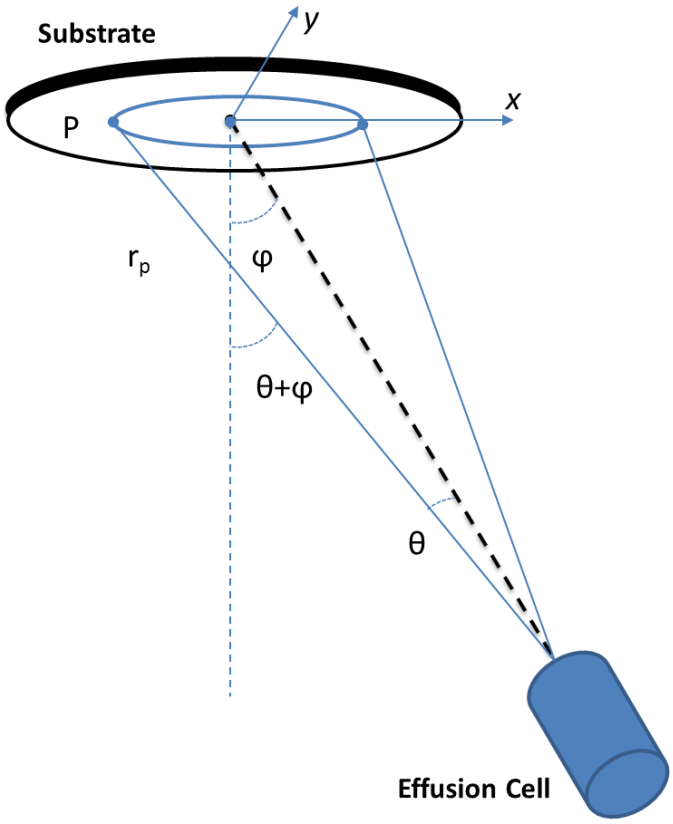

Figure 3.9: Schematic of the positioning of an effusion cell and the substrate in MBE system. φ and θ are angles between cell and substrate and between cell axis and path. The figure is after Franchi, Elsevier (Franchi 2013).

To illustrate the flux variation across the substrate at different growth positions, we used Equation 3.18 for Ga flux at 1000K cell temperature. Distribution is symmetric at the growth position but not perfectly uniform.

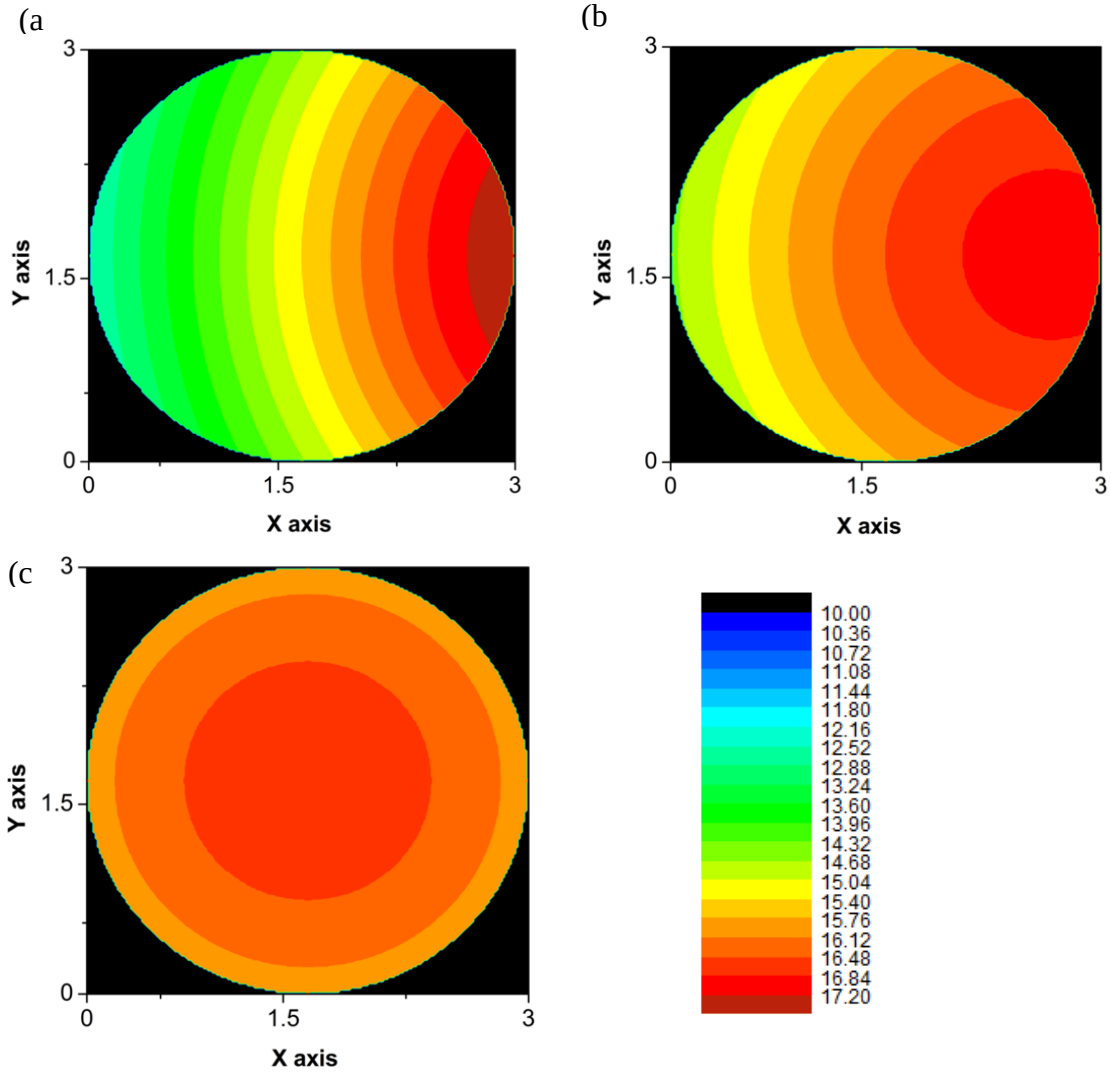

Figure 3.10: (a),(b) & (c) Calculated Ga flux variations at different points on a 3-inch wafer at pyrometer , RHEED and Growth positions respectively.

3.4 Dependence of MBE growth conditions on QD structural parameters

Many attempts have been devoted to explore the dependence of island densities, critical sizes and shapes on the growth conditions, as this aspect underlines achieving the desired optical properties, including quantum dot behavior. Narrowing the density of states has not yet shown to produce superior performances due to a large size distribution. For the low-height InAs dots, the dispersion of quantum energy caused by the variety of dot sizes becomes large because of their large quantum effect resulting in a large linewidth in the emission spectra. A narrower line width is achievable in larger dots hence fabricating large-size dots is also useful for the active region of long-wavelength lasers (Saito, Nishi, and Sugou 1999). Nevertheless depositing more InAs to fabricate larger QDs causes a coalescence of dots and introduces dislocations in the dots during the growth of high-density InAs QDs. Thus acquiring proper dot structural parameters via precise control of growth conditions has become vastly important study.

3.4.1 Flux ratio dependence on QD dot density and size

The influence of the As_4 flux on InAs QDs differ significantly in connection with the mobility of atomic species on the surface, surface energy, In desorption and In segregation efficiency. The observed decrease in InAs island density in Figure 3.11 and the increase in the average lateral size of the islands is manifestation of the strain-enhanced cation migration.

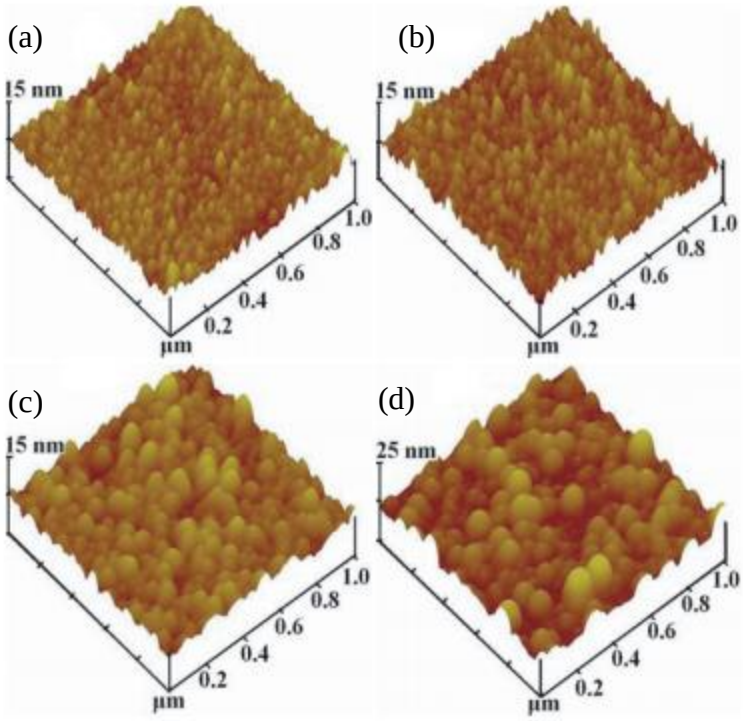

Figure 3.11: AFM images of InAs QDs on GaAs(001) growth with V/III flux ratio (a) 22, (b) 45, (c) 89 and (d) 190. The figure is after Meng *et al*. EPL Journal, (Meng *et al.* 2008).

The decrease in the island density with increasing temperature in Figure 3.12 is a consequence of the thermally enhanced indium surface migration. Formation of 3D islands depend on the attachement/detachement rate of cations (In) and anion (As) surface migration length. At the lower temperatures (420^0C) enhanced arsenic incorporation with increasing arsenic pressure, enabling the cations to be incorporated and the island density to decrease. At higher temperatures ($\geq 480^0$C) where anion incorporation is not the limitation, increased arsenic pressure will not necessarily lead to a significant impact on island growth (and hence density) since the increased anion pressure inhibits cation migration.

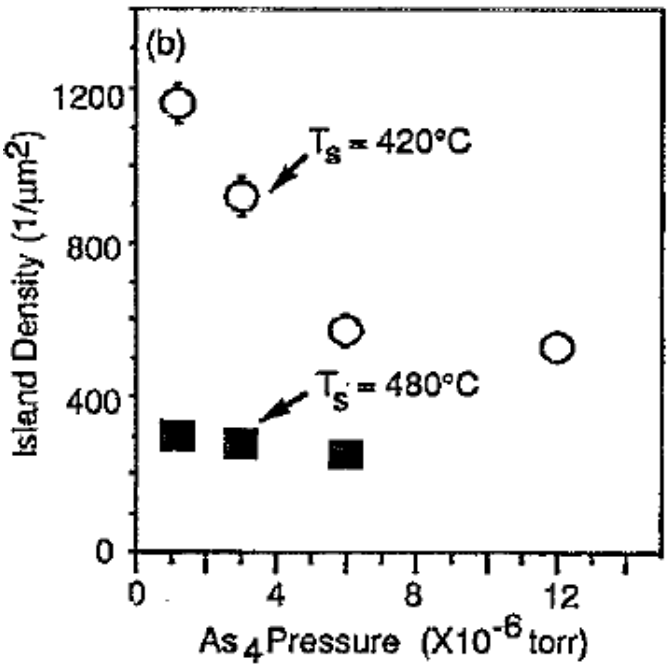

Figure 3.12: The variation of InAs dot density as a function of As_4 flux ratio grown at 480^0C and 420^0C. The figure is after Madhukar *et al.*,Appl. Phys. Lett. (Madhukar *et al.* 1994).

3.4.2 Effect of growth temperature on QD density and size

Increasing the growth temperature reduces the nucleation rate of the dot, so the dot density is decreased and the dot size is increased simultaneously. A dot of a pyramidal shape with low aspect ratio is transformed when its volume exceeds a critical value by raising the growth temperature. The shape transition indicates that the high-aspect-ratio dot is energetically favorable at a large volume and the size distribution become uniform.

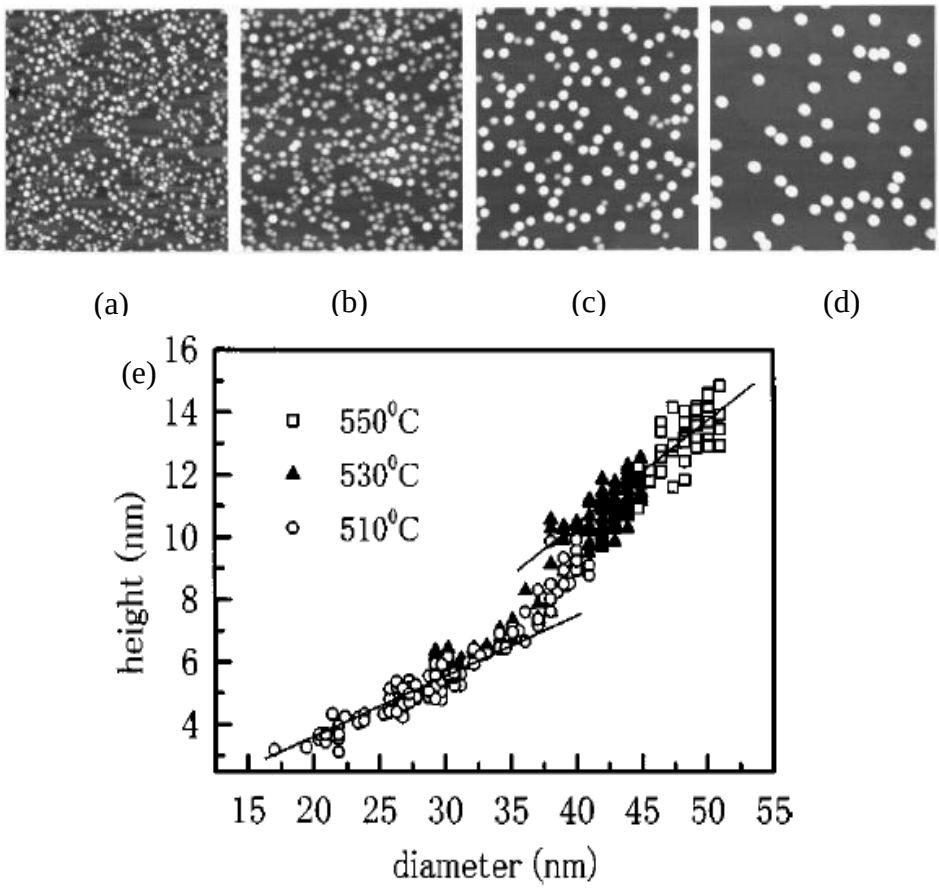

Figure 3.13: 1μm x 1 μm AFM images of InAs QDs grown at temperatures (a) 500^0C, (b) 510^0C, (c) 530^0C and (d) 550^0C. (e) Height of the InAs quantum dots as a function of their diameter grown at different temperatures. This figure is after Saito, Nishi, and Sogou, Appl. Phys. Lett. (Saito , Nishi, and Sogou 1999).

3.4.3 Effect of annealing on QD size and density

As shown in Figure 3.14 the mean volume of QDs increases and their density decreases as function of annealing owing to the coarsening at higher temperatures. Although the average AR decreases for case of annealing at 460^0C with compared to 420^0C, as shown in Figure 3.14(e), the average volume and the number density do not change. A mass redistribution on the surface of QDs, evolving from { 1 3 6} to {1 3 7} facets while also

eliminating incomplete layers on the top of islands is considered as a possible explanation for this effect.

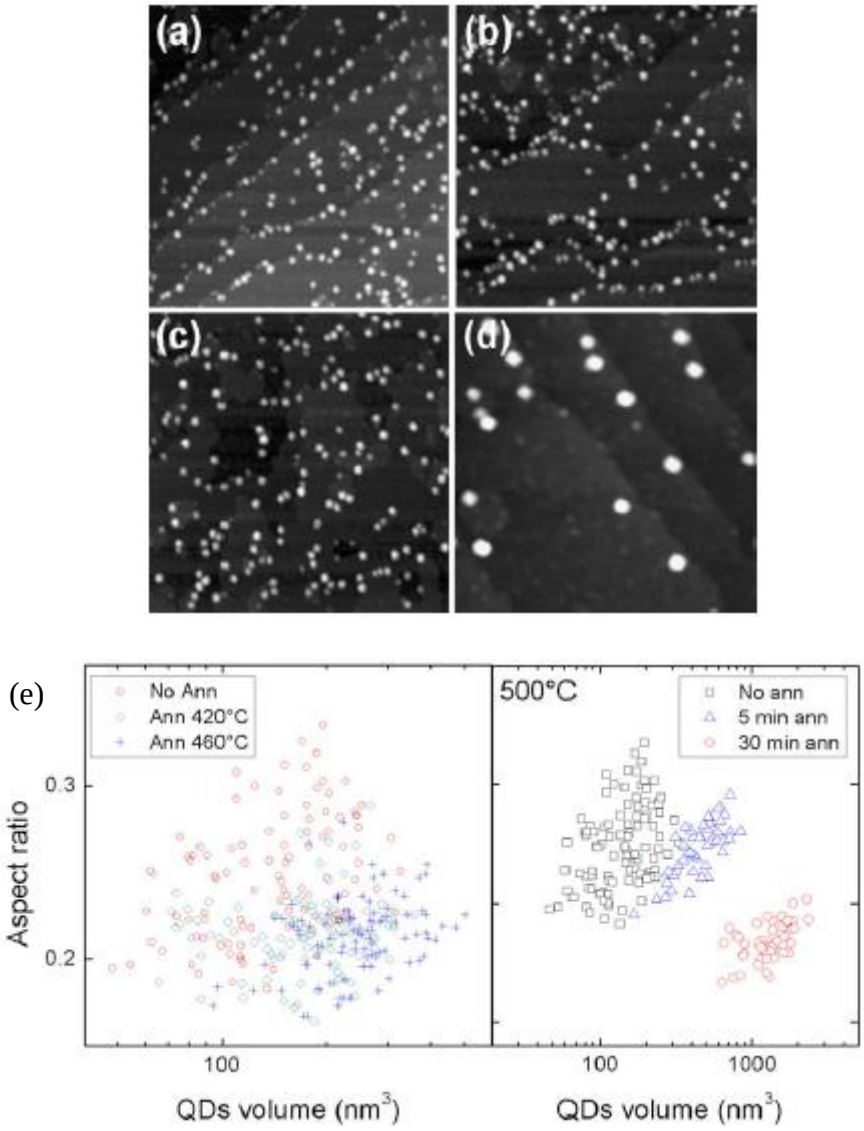

Figure 3.14: 1μm x 1 μm AFM images of 1.7 ML InAs QDs on GaAs(001) (a) immediately quenched and with a postgrowth annealing at (b) 420^0C, (c) 460^0C and (d) 500^0C. (e) QD aspect ratio (AR) vs volume for above temperatures. The figure is after Placidi, Pia, and Arciprete, Appl. Phys. Lett. (Placidi, Pia, and Arciprete 2009).

Annealing at higher temperatures (at 500^0C) or for a longer period increases the mean volume of QDs, changing the AR and faceting since coarsening is faster than WL and substrate erosion.

3.4.4 The nature of capping layer matters

The impact of the capping layer on the structural dot properties is under an in-depth investigation, as the overgrowth process is the essential issue to determine the optical properties of the nanostructures. It has been reported that the shape of InAs QDs changes drastically during the initial stage of GaAs overgrowth (Kiravittaya, *et al.* 2006).

The observed surface evolution of QDs in Figure 3.15 due to different capping material can be explained by effects of elastic energy and surface energy included in the surface chemical potential. In QDs with GaAs capping, the increase of the elastic energy of the QDs and surface energy of the cap drive the In atoms away from the InAs QDs to the GaAs surface. The In atom migration away from the InAs QDs and the unfavorable growth of GaAs on top of the QDs result in a collapse of the InAs QDs and a valley formation at the beginning of the GaAs overgrowth.

In case of the $In_{0.1}Ga_{0.9}As$ cap layer, an increased In content decreases the elastic energy and also the cap layer surface energy. This results in a reduction of the chemical potential gradient which leads to a preservation of the QD shape.

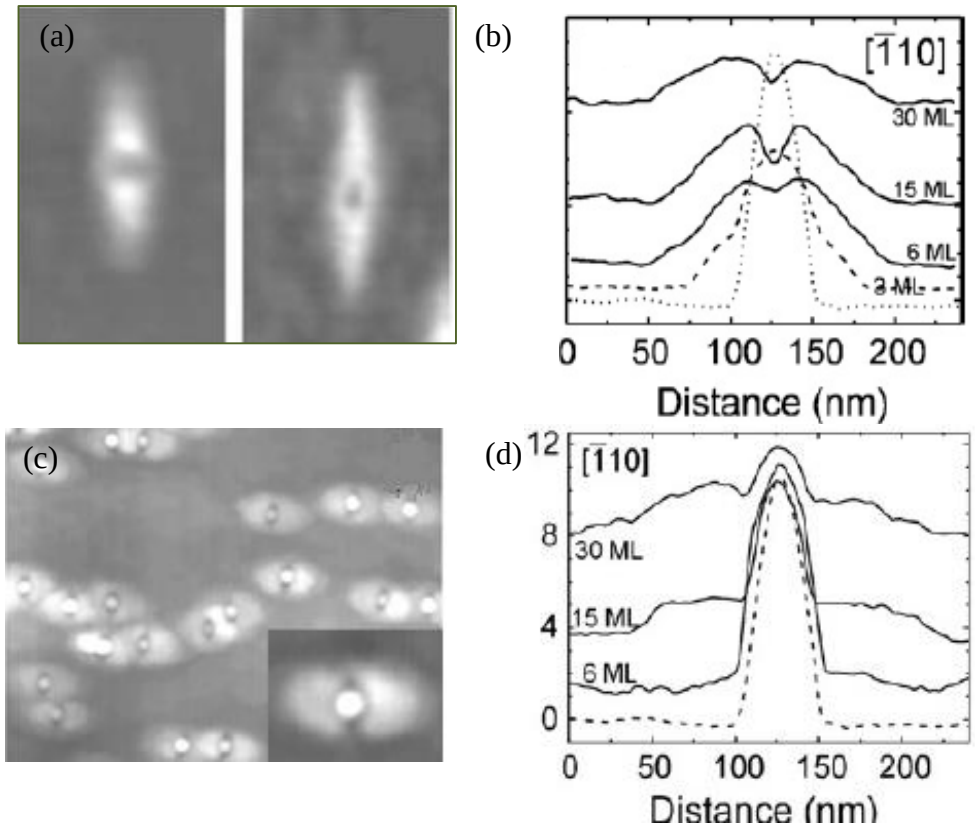

Figure 3.15: AFM images of InAs QDs partially covered with (a) GaAs capping (0.125 x 0.2 μm^2 AFM images) and (c) $In_{0.1}Ga_{0.9}As$ capping (1 x 0.75 μm^2 AFM images). Height profiles of (b) GaAs and (d) $In_{0.1}Ga_{0.9}As$ partially capped InAs QDs. The figure is after Songmuang, Kiravittaya, and Schmidt, J. Crys. Growth (Songmuang, Kiravittaya, and Schmidt 2003).

3.5 Summary

Morphological changes of GaAs growth by MBE is described in the first part of this chapter. The diagrams of atomic positions and details of V/III flux dependent *c*(4X4), α(2X4) or β2 (2X4) and ζ(4X2) are presented. Schematic of a MBE chamber is given next. The calculations of flux variation across a substrate show that the orientation of flux deposit on the substrate is not uniform at growth, pyro, and cell positions.

The reaction of Ga and As_2 on GaAs is discussed in two process: adsorption and desorption. Under adsorption, it is explained how the sticking coefficient of Ga on GaAs which is accounted to be unity dominate the growth of GaAs layers at elevated temperatures. Further the mechanism of desorption of As_2 with consumption of adsorbed Ga is investigated.

Further, the significant effects of growth conditions on dot structural parameters are presented which can be used for precise control over dot sizes, shapes and density. The increase in dot size with decreasing dot density and the formation of high aspect-ratio dots at higher temperatures, annealing times and V/III flux ratio are discussed. Finally how the dot capping material alter the shape of QDs is presented for GaAs and In0.1Ga0.9As capping materials.

Chapter 4

Fundamentals and Analysis of Reflection High-energy Electron Diffraction (RHEED)

The basics and analysis of RHEED technique are the outline in this chapter. The first discovery on high-energy electron diffraction from electron scattering by a single crystal is presented at first in Section 4.1. The rest of the section consists of diffraction fundamentals including 2D reciprocal lattice, Ewald construction, Laue circles and origin of streak lines. The next Section 4.2 shows the components of the RHEED system we own in our CAM facility. In the final section (Section 4.3) initial literature reports of QD structural properties from RHEED features will be demonstrated.

4.1 Diffraction fundamentals

The first experiments on scattering of electrons by a single crystal was done by Davisson and Germer (Davisson and Germer 1927) by directing a narrow beam of electrons normally against a single crystal of nickel. This study led to discovery of electron diffraction which became the foundation of high-energy electron diffraction (Nishikawa and Kikuchi 1928) (Kikuchi 1928).

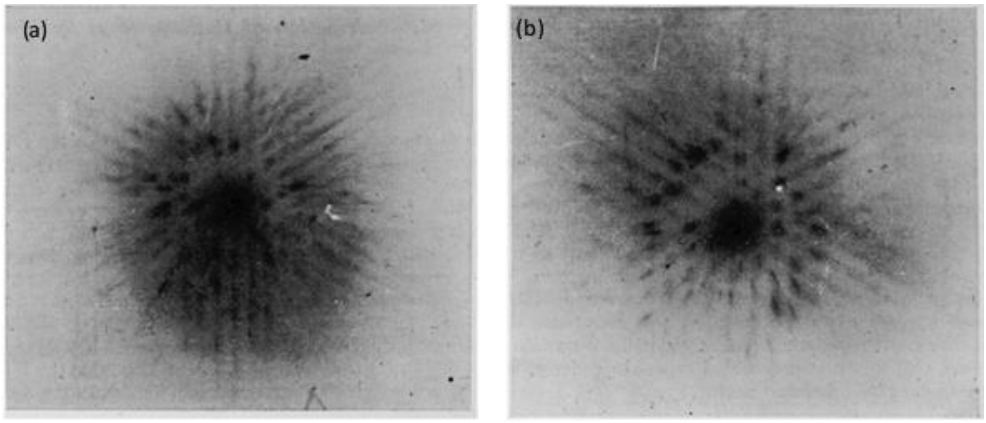

Figure 4.1: First observations of diffraction patterns by electrons performed by Kikuchi at applied potentials (a) 78kV and (b) 57kV. The figure is after Kikuchi, Proc. Roy. Soc. Ser. A. (Kikuchi 1928). (No scale provided in the original figure).

RHEED has the capability of monitoring atomic layer by layer growth in epitaxial films by tracing intensity oscillations in diffraction pattern. Thus, control over atomic layer growth rates in MBE has become the most important application of the technique in opto-electronic device industry. Smaller penetration depths and interaction of electrons with the first few layers of a crystal lattice due to grazing incidents are the primary advantages of RHEED as a tool for probing sensitive surface morphologies.

The origin of RHEED diffraction patterns from QD features can be understood by understanding the fundamentals of diffraction conditions. Let's assume a plane wave with a wave vector $\boldsymbol{k_i}$ incident on an atom at a position $\boldsymbol{r}_i$ which produces a scattered wave of wave vector $\boldsymbol{k_f}$ and the magnitude of $\boldsymbol{k}i$ is given by

$$k_i = \frac{2\pi}{\lambda_i}, \tag{4.1}$$

and the wave length λ_i takes the form

$$\lambda_i = \sqrt{\frac{h^2}{2mE_i}}, \tag{4.2}$$

where E_i is the kinetic energy and h is the Planck's constant.

The diffraction geometry for the grazing angle (ϑ_i) where incident and diffracted angles are finite, the scattering is categorized in two ways: in-plane scattering (Figure 4.2) and specular reflection (Figure 4.3).

In the case of spherical coordinates, diffraction conditions in reciprocal lattice space (k-space) take the form,

$$k_x = k_f cos\vartheta_f cos\varphi_f\ , \tag{4.3}$$

$$k_y = k_f cos\vartheta_f sin\varphi_f\ , \tag{4.4}$$

$$k_z = k_f sin\vartheta_f, \tag{4.5}$$

where ϑ_f is the scattered angle and φ_f is the azimuth angle.

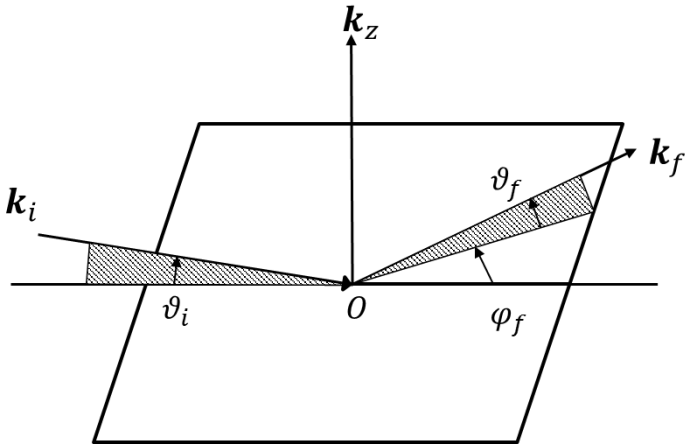

Figure 4.2: Diffraction geometry for a grazing angle in-plane scattering measurement. The figure is reproduced from Yang, Wang, and Lu, World Scientific Publishing Co.(Yang, Wang, and Lu 1993).

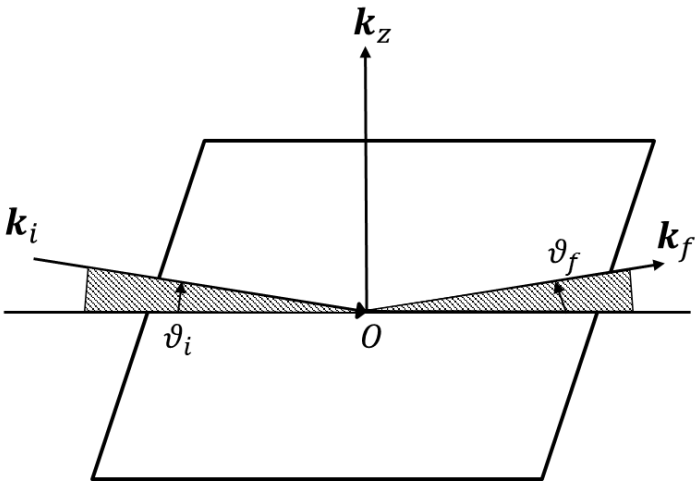

Figure 4.3: Diffraction geometry for specular reflection measurement. The figure is reproduced from Yang, Wang, and Lu World Scientific Publishing Co. (Yang, Wang, and Lu 1993)

As depicted in Figure 4.4, the path difference, $\boldsymbol{S}.\boldsymbol{r}_{i,}$ between the incident and scattered beam where $\boldsymbol{S} = \boldsymbol{k}_f - \boldsymbol{k}_i$ gives rise to the interference conditions.

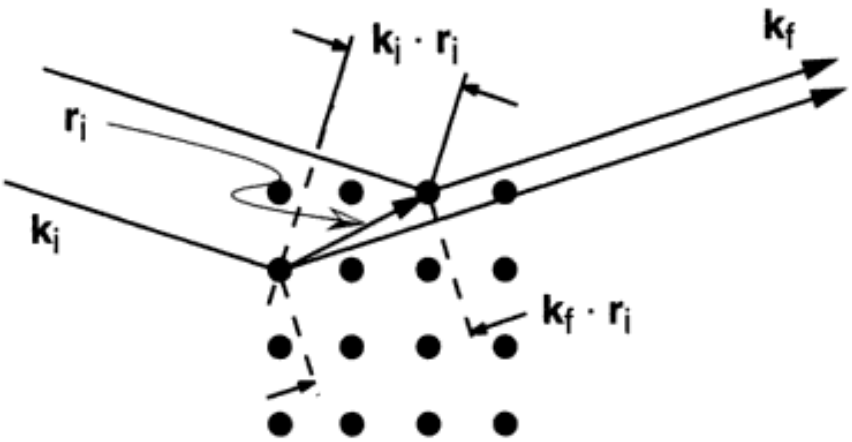

Figure 4.4: The path difference between incident and scattered waves. The figure is after Ichimiya and Cohen, Cambridge University Press (Ichimiya and Cohen 2004).

Summing over all scatters in the crystal, the diffracted amplitude of wave function $\psi(\boldsymbol{r}) = Ae^{i\boldsymbol{k}.\boldsymbol{r}}$ becomes

$$A(\boldsymbol{S}) \sim \sum_i e^{i\boldsymbol{S}.\boldsymbol{r}_i} , \tag{4.6}$$

Thus the intensity from interference is expressed as

$$I = AA^* \sim \sum_{i,j} e^{i\boldsymbol{S}.(\boldsymbol{r}_j - \boldsymbol{r}_i)} , \tag{4.7}$$

The most relevant parameter in the above intensity function is the momentum transfer along the direction of the array of atoms. This momentum space is represented in terms of reciprocal lattice which is the Fourier transform of the special wave function of the original lattice. For diffraction from a surface, the reciprocal lattice of a two-dimensional arrays is discussed in the following section.

4.4.1 Two-dimensional reciprocal lattice

The position vector $\boldsymbol{R}$ of a two-dimensional Bravais lattice in real space is given as

$$\boldsymbol{R} = n_1\boldsymbol{a_1} + n_2\boldsymbol{a_2}\,, \tag{4.8}$$

where n_1 are n_2 are integers and $\boldsymbol{a_1}$ and $\boldsymbol{a_2}$ are linearly independent primitive cell vectors.

The corresponding reciprocal lattice is defined by the primitive lattice vectors $\boldsymbol{a}_j^*$ with $\hat{\boldsymbol{z}}$ being the unit vector normal to the lattice plane.

$$\boldsymbol{a}_1^* = 2\pi\frac{\boldsymbol{a}_2 \times \hat{\boldsymbol{z}}}{\boldsymbol{a}_1.(\boldsymbol{a}_2 \times \hat{\boldsymbol{z}})}\,, \tag{4.9}$$

$$\boldsymbol{a}_2^* = 2\pi\frac{\boldsymbol{a}_1 \times \hat{\boldsymbol{z}}}{\boldsymbol{a}_2.(\boldsymbol{a}_1 \times \hat{\boldsymbol{z}})}\,, \tag{4.10}$$

Hence the reciprocal lattice vector can be written as

$$\boldsymbol{B_m} = m_1\boldsymbol{a_1^*} + m_2\boldsymbol{a_2^*}\,, \tag{4.11}$$

In a simple structure with lattice parameters a and b along two crystal axes $\hat{\boldsymbol{x}}$ and $\hat{\boldsymbol{y}}$, the reciprocal lattice vectors are

$$\boldsymbol{a_1^*} = \left(\frac{2\pi}{a}\right)\hat{\boldsymbol{x}}\,, \tag{4.12}$$

$$\boldsymbol{a_2^*} = \left(\frac{2\pi}{b}\right)\hat{\boldsymbol{y}}\,, \tag{4.13}$$

Thus the reciprocal lattice becomes a set of parallel rods with the separation of $(2\pi/a)$ and $(2\pi/b)$.

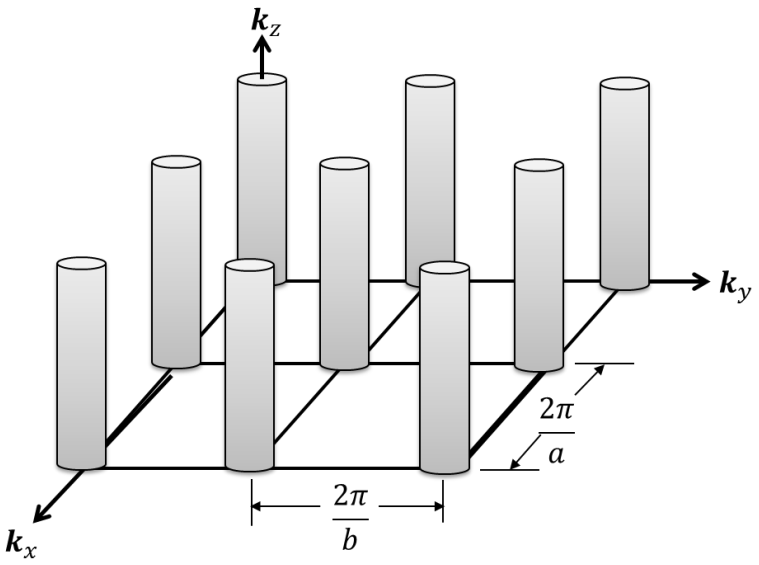

Figure 4.5: Reciprocal lattice space of two-dimensional crystal. The figure is reproduced from Yang, Wang, and Lu, World Scientific Publishing Co.(Yang, Wang, and Lu. 1993).

The diffraction intensity is $(N_x N_y)^2$and each rod represents the region in which the intensities are higher than the half of the maximum in the corresponding angular profile. The angular features in the diffraction pattern can be described with the help of Ewald construction.

4.1.2 The Ewald construction

The Ewald construction combines energy and momentum conservation which satisfy the following requirements

$$|\boldsymbol{k}_i| = |\boldsymbol{k}_f|, \tag{4.14}$$

$$\boldsymbol{k}_f - \boldsymbol{k}_i = \boldsymbol{G}_m\,, \tag{4.15}$$

where $\boldsymbol{G}_m$ is a vector of the reciprocal lattice and the subscript *m* denotes the *m*th diffracted beam.

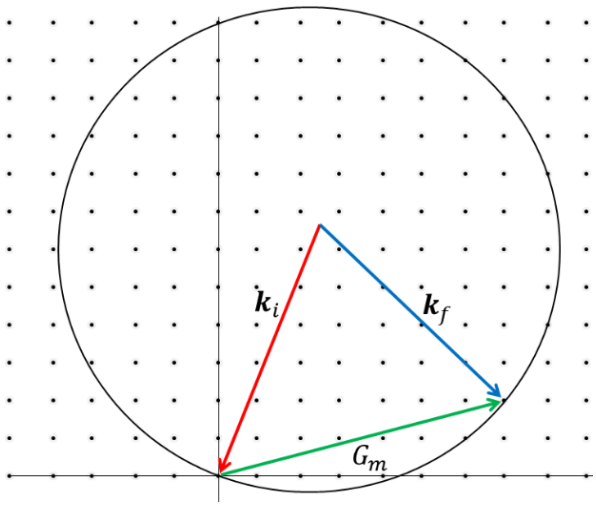

Figure 4.6: Ewald's sphere construction for the case of diffraction from a 2D lattice.

Equation 4.14 fulfills the energy conservation and hence the locus of all final vectors is a sphere of radius $|\boldsymbol{k}_i|$. In momentum conservation the difference between the wave vectors of diffracted and incident wave is defined as scattering vector in the reciprocal lattice $\boldsymbol{G}_m$(Equation 4.15).

4.1.3 Laue circles

Ewald sphere consists of planes of closely spaced lattice rods as shown in Figure 4.7. The intersections of these effective planes with the Ewald sphere forms zones called Laue zones. The central zone is called the zero-order Laue zone (ZOLZ) and the other levels above are called higher-order Laue zones (HOLZ). The RHEED pattern is a collection of points on the perimeters of concentric Laue circles around the center point.

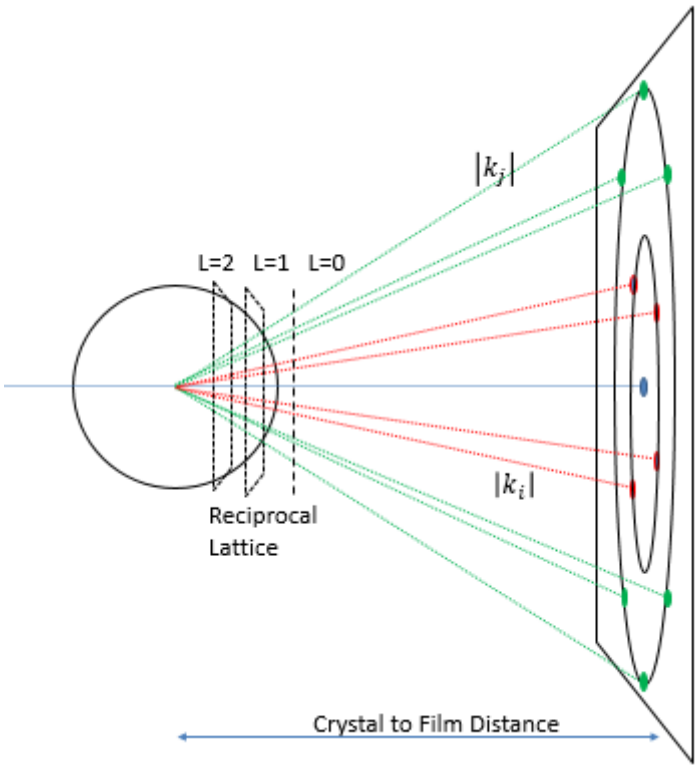

Figure 4.7: Construction of Laue circles. The points of different colors represent diffraction spots on higher-order Laue circles.

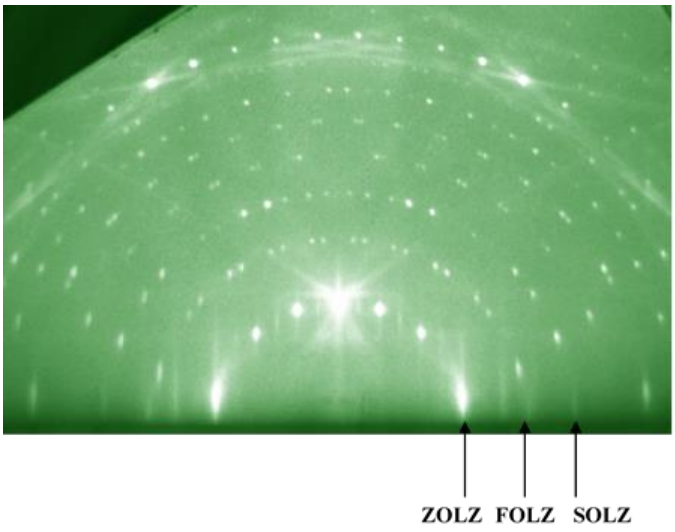

Figure 4.8: Laue zones of a RHEED Pattern from Au/Ag/Si(111) $\sqrt{21} \times \sqrt{21}$ Surface The figure is after Ichimiya *et al*.(Ichimiya, Sato, Sueyoshi, *et al.* 1994).

4.1.4 Origin of RHEED streak lines

The dependence of spot shape on the surface morphology is discussed in this section. Reflection from a perfectly smooth surface forms sharp diffracted spots on Laue circles as shown in Figure 4.7 while the fractional order diffraction beams are reflected from a reconstructed surface. The steps on an imperfect reconstructed surface produce a broadening of the reciprocal lattice rods and thus, result in elongated and broadened diffraction spots which are called 'streaks' (Daweritz and Ploog 1994). An illustration of the formation of streak lines is shown in the following Figure 4.9.

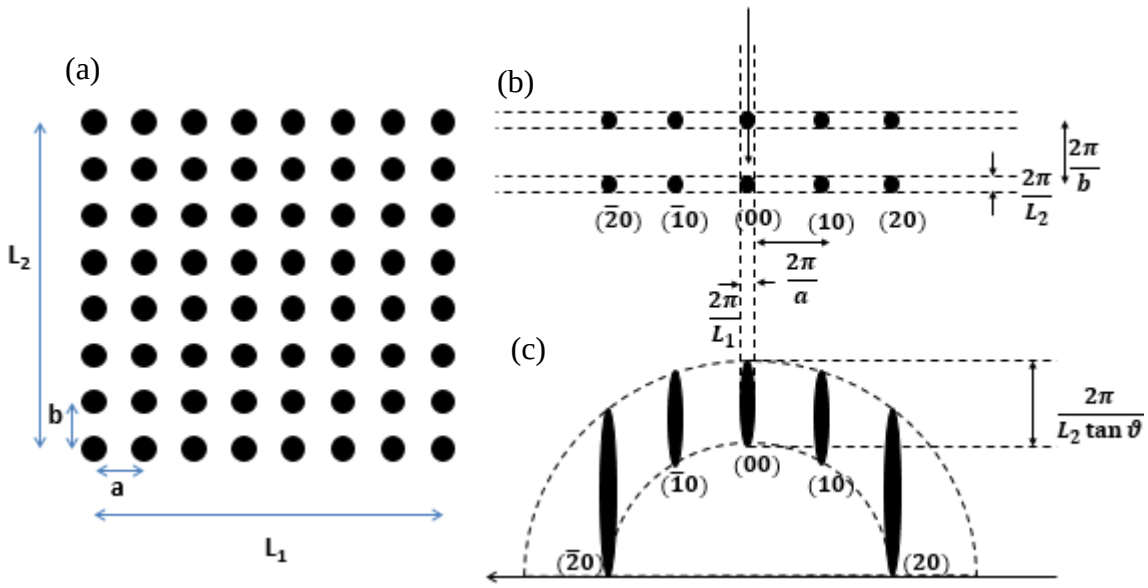

Figure 4.9: (a) 2D- array of lattice points of the lattice with L_1 and L_2 dimensions. (b) Reciprocal lattice for the lattice array in (a) and (c) is the corresponding RHEED construction. The figure is reproduced from Ichimiya and Cohen, Cambridge University Press (Ichimiya & Cohen 2004).

As seen from the figure, not only the surface morphology causes streak behavior, the length of the streaks depends on the glancing angle of incident. In two dimensional lattice the intersection of reciprocal lattice points with Ewald sphere at low glancing angles causes elongation in the shape of diffraction spots into a streak pattern. The low glancing angle primarily impacts the width of the diffracted beam normal to the samples surface.

4.2 Instrumentation

The RHEED gun is the key ingredient in RHEED system. For high-energy applications the energy requirement lies in the range of 8 to 20 keV.

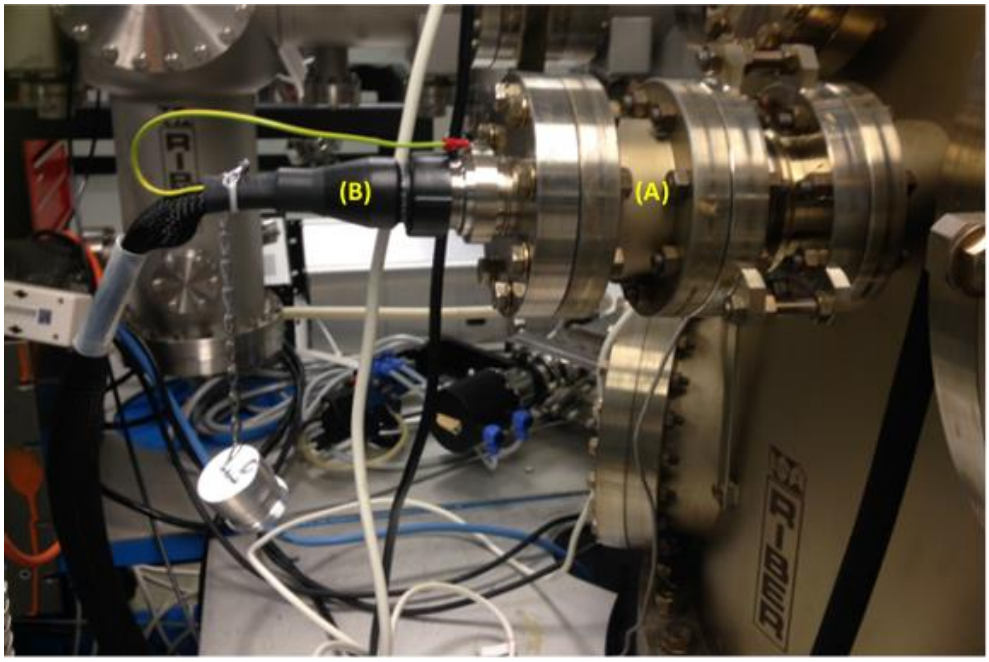

Figure 4.10: (A) 12 keV RHEED gun mounted in a viewport (B) RHEED cable at CAM facility.

Small angular divergence at the sample and small spot size at the screen produce better result in diffraction pattern. About 0.5-1.0 mrad angular divergence and about 0.1mm spot size are adequate for most RHEED studies (Ichimiya and Cohen 2004). The electron beam is deflected by a magnetic deflector and is incident on the surface at a glancing angle of 1-2^0 to the surface to ensure smaller penetration depth of 1-2 atomic layers due to small electron momentum normal to the surface (Parker 1985).

The beam diffracted from the surface hits a fluorescent screen that consists of a phosphor covered, indium-tin-oxide coated pyrex disk forming a diffraction pattern. The indium-tin-oxide coating prevents charging at the screen from electron bombardment. The pattern is then captured by a charge-coupled detector (CCD) and data acquisition is performed by a software called KSA 400.

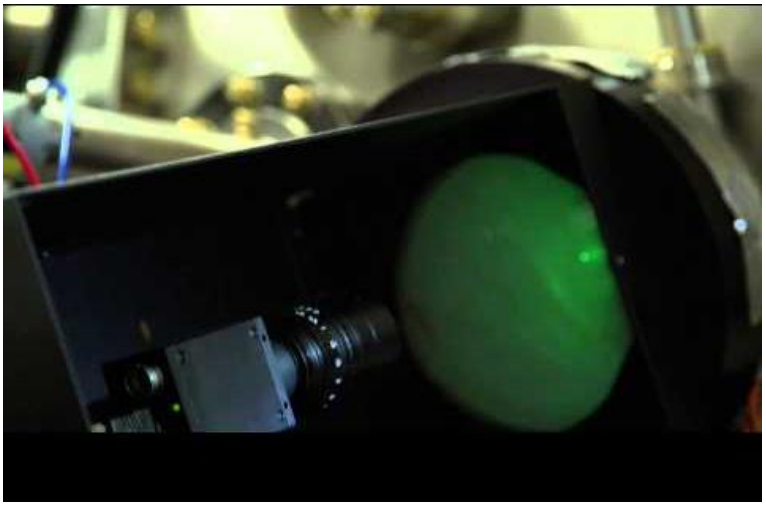

Figure 4.11: Phosphorous screen and the image acquisition camera attached to UHV chamber.

4.3 RHEED as an analytical tool

The sensitivity of RHEED to atomic features has been utilized in extracting structural properties and analyzing growth conditions quantitatively and qualitatively. As a result monolayer growth rate, surface orientation, quantum dot shapes and strain variation are studied in terms of RHEED intensity profiles. The phenomenon of oscillatory rate behavior of intensity of the specular beam in crystal growth has been discussed below and the relationship to the monolayer growth rate is stated. Section 4.4.2 describes how RHEED modifies due to different imperfection of the sample surface, for e.g. RHEED from β2(2x4) reconstructed GaAs(001) surface will be included.

4.3.1 Monolayer growth rate

First evidence on the oscillations of intensity of RHEED streaks was presented by J. J. Harris *et al.* 1981.They claimed that if the growth is initiated on a GaAs substrate with pre-deposited or surface-accumulated Sn, the oscillations in the intensity modulation of some of the RHEED streaks occur due to complex incorporation of Sn and the periodicity is equal to the monolayer deposition time of GaAs (Harris, Joyce, and Dobson 1981). The observed decaying of intensity was found to be strongly dependent on Ga flux and substrate temperature and the phenomena was qualitatively explained by local variations in growth rate, arising from the statistical nature of the arrival of Ga atoms. Subsequently it was pointed out that the damping of the spot intensity cannot be explained on the basis of impurity (Sn atoms) (Wood 1981) and this behavior was interpreted as the increase of the variation in the size of domains after the onset of growth to some dynamic limit at which the nucleation of new, and coalescence of growing domains are in equilibrium. Later on a

detailed observation of the intensity oscillations in the specularly reflected and various diffracted beams in the RHEED pattern have been made during MBE growth (Neave *et al.* 1983) .

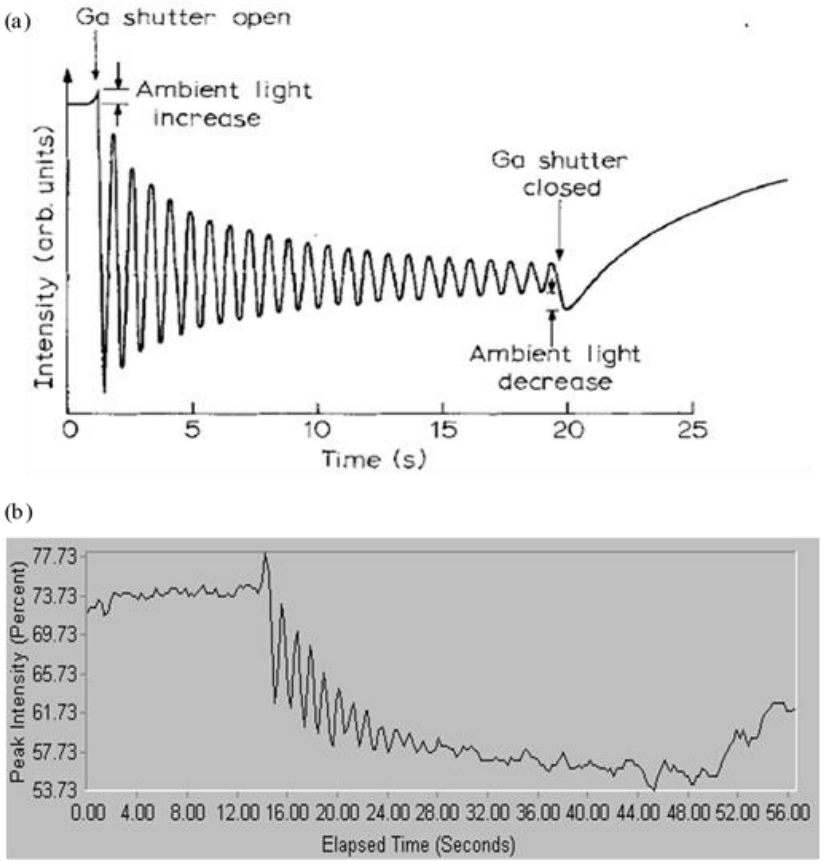

Figure 4.12: (a) Intensity oscillation of the specular beam in the RHEED pattern from GaAs(001) – (2X4) reconstructed surface, along [110] azimuth. The figure is after Neave *et al*. Appl. Phys. (Neave *et al.* 1983). (b) RHEED oscillations for GaAs layer ML growth observed in CAM lab facility.

Basic observations of damped oscillations in the intensity are depicted in Figure 4.12. The period of the oscillations exactly relates to the growth rate of a single monolayer that is a layer of Ga+As atoms. The growth mechanism corresponds to the features of the above figure is described below with the help of Figure 4.13.

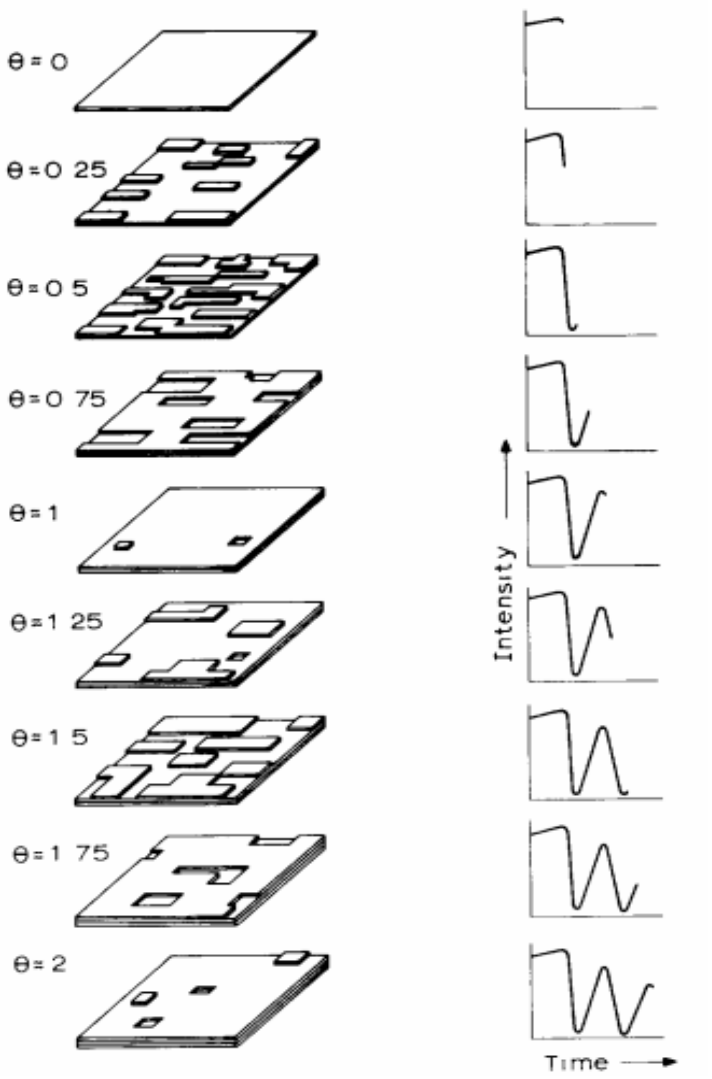

Figure 4.13: Intensity oscillations of the specular beam in the RHEED pattern of a GaAs surface during MBE growth. The figure is after Joyce *et al*. Surf. Sci. (Joyce, Dobson, and Neave 1986) .

At the start of the growth, random clusters with a stable cluster size are generated. When all the clusters are coalesced and holes are filled, the layer is complete. Initial equilibrium surface is smooth yielding high reflectivity in the intensity oscillations. However, most adatoms desorb before they are incorporated in the growing clusters. The intensity then decreases as the nucleation of the next layer is commencing. This sequence repeats, with

gradual damping as growth becomes distributed over several layers. The minimum in the reflectivity arise from the intermediate stage when the growing layer is approximately half complete. The formation of new layers before completing the preceding one produces the damping effect. Figure 4.13 shows a real space representation of the formation of a single complete layer which illustrates the behavior of oscillations in the specular beam.

4.3.2 Growth morphology of 2D surfaces

RHEED has been used to study the surface structure as well as the surface texture of homoepitaxially grown GaAs films. The imperfections of the sample surface modify RHEED pattern and it is very useful in fabricating PV modules with higher crystal quality.

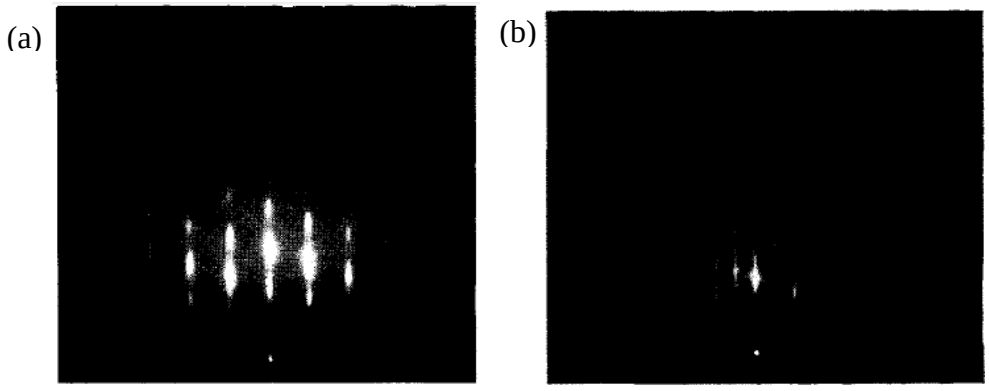

Figure 4.14: (a) $(\overline{1\,1\,1}) - \sqrt{19}$) GaAs surface at 520^0C and (b) $(\overline{1\,1\,1}) - 2$ GaAs surface grown at 400^0C. The figure is after Cho, J. Appl. Phys.(Cho 1970).

The first evidence of surface reconstruction of GaAs$(\overline{1\,1\,1})$ surface under different growth temperatures was reported in 1970 by A. Cho (Cho, 1970). He observed Ga-rich $(\overline{1\,1\,1}) - \sqrt{19}$ surface reconstruction at higher temperatures and As rich $(\overline{1\,1\,1}) - 2$ at lower temperatures with transition temperature being a function of the Ga and As deposition rate (Figure 4.14).

Recently the surface reconstruction of mostly used GaAs(001) surface has been resolved by STM (LaBella 1999) and RHEED has been used to monitor the surface quality by tracing the diffraction pattern. GaAs β2(2X4) surface has periodicity of 4 along [1 1 0] and periodicity of 2 along [1 $\bar{1}$ 0] and corresponding RHEED patterns are shown in Figure 4.15(c) and (d).

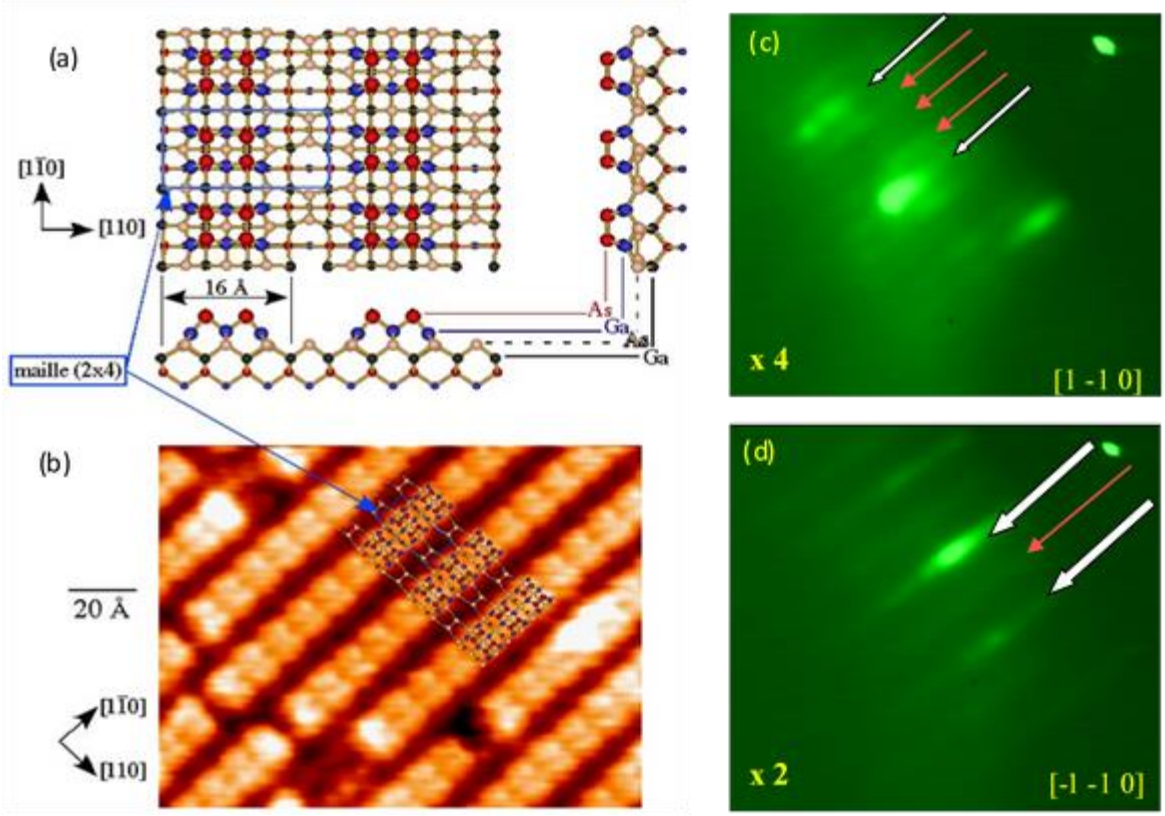

Figure 4.15 : (a) Geometry of atomic positions of GaAs β2(2X4) reconstruction (b) STM image of the above reconstruction obtained from MBE grown GaAs (Garreau *et al.* 1996) and experimentally observed (c) X4 [1-10] surface reconstruction and (d) X2 [$\bar{1}$ $\bar{1}$ 0] surface reconstruction in CAM facility.

4.3.3 Quantum dot structural properties from RHEED

RHEED has proven its reliability as an *in-situ* analytical tool in probing QD nucleation along with strain relaxation and structural parameters such as dot facet configuration and dot density distribution.

4.3.3.1 WL(2D) to QD(3D) transition

Transition from 2D InAs layer to 3D QD structures in SK growth mode can be traced by RHEED diffraction pattern. 2D InAs wetting layer takes different forms when grown on different GaAs surface reconstructions (discussed in Chapter 3) (Tsukamoto *et al.* 2006) (Prohl *et al.* 2010)(Honma, Tsukamoto, and Arakawa 2006). In our growth regime where GaAs is of β2(2X4) form, InAs wetting layer turns into either (4x3) or (1x3) surface depending on monolayer coverage and In,Ga intermixing (Krzyzewski *et al.* 2002).

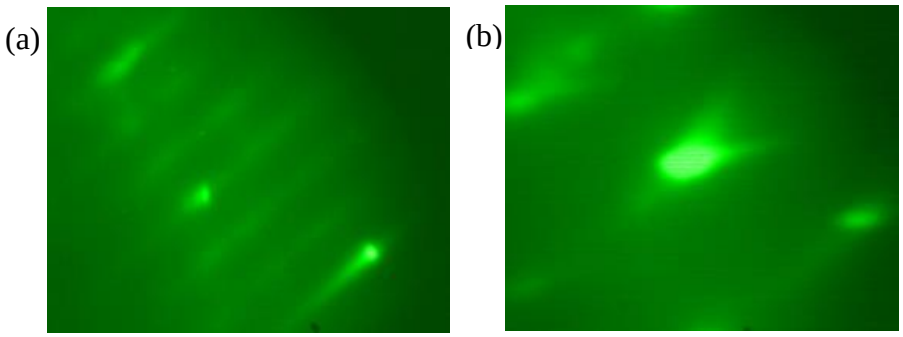

Figure 4.16: (a) X3 diffraction of 2D InAs wetting layer and (b) chevron diffraction feature from 3D islands along [1-10] azimuth.

As the islands start forming a streak diffraction pattern transforms to a chevron, a V shaped feature with two tails attached to the diffraction spot. The intensity variation at the (002) diffraction spot is during growth is shown in Figure 4.17.

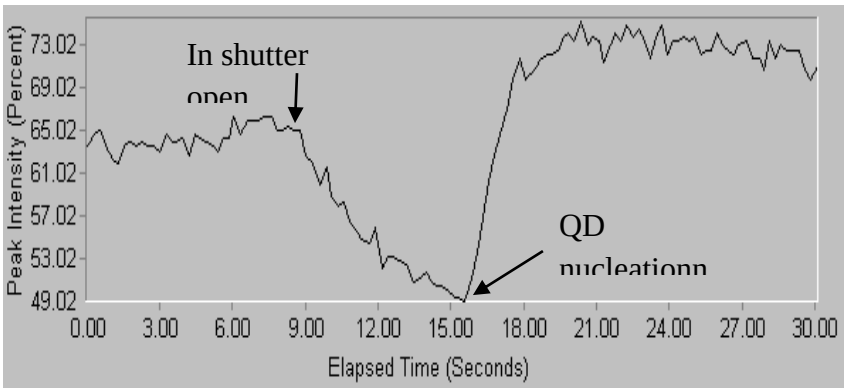

Figure 4.17: RHEED intensity variation during 2D-3D transition.

4.3.3.2 Real-time extraction of QD strain relaxation

Calculation of electronic structure of QD systems includes strain distribution and strain relaxation of atoms caused by heteroepitaxy of lattice mismatched layers. Hanada *et al.* provides a detailed insight of nominal relaxation of the mean strain of QDs measured by RHEED as a function of InAs coverage.

The in-plane strain values in Figure 4.18 (d) are calculated from the distance between the $(\bar{1}\,1\,1)$ and $(1\,\bar{1}\,1)$ spots (circles) and $(\bar{1}\,1\,3)$ and $(1\,\bar{1}\,3)$ spots (square) during and after InAs growth for 25s (open) and 30s (solid). From the figure it is evident that the nominal strain relaxation depends on the take-off angle of the electron beam. $(\bar{1}\,1\,1)$ and $(1\,\bar{1}\,1)$ spots with a small take-off angle show higher relaxation due to scattering of electron beam from the relaxed top most layers while $(\bar{1}\,1\,3)$ and $(1\,\bar{1}\,3)$ spots are originated from strained deeper levels which is the reason for low strain relaxation in $(\bar{1}\,1\,3)$ and $(1\,\bar{1}\,3)$ planes (Hanada, Totsuka, and Yao 2001).

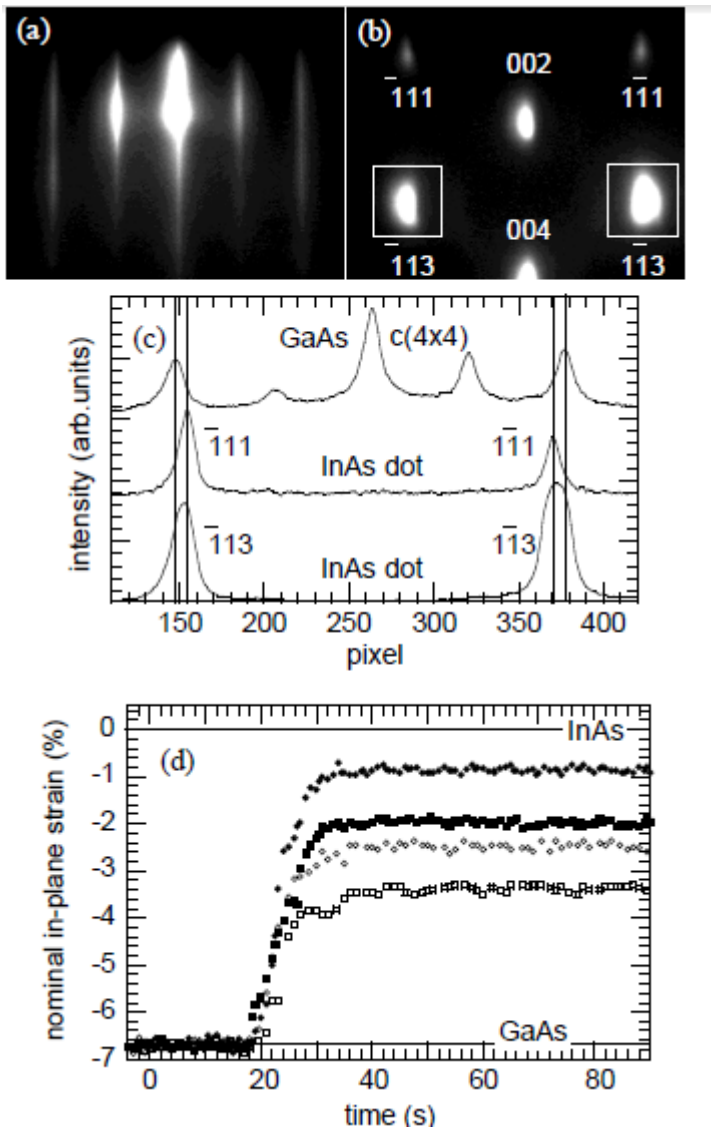

Figure 4.18: RHEED pattern of (a) GaAs(001)- c(4x4), (b) InAs QD along [1 1 0] azimuth, (c) RHEED intensity profiles across $(\bar{1}\ 1\ n)$ and $(1\ \bar{1}\ n)$ for n =1,3 diffraction spots and (d) relaxation of nominal in-plane strain calculated. The figure is after Hanada *et al*. Phys. Rev. B (Hanada, Totsuka and Yao 2001).

4.3.3.3 Real-time extraction of QD density from RHEED

QD number density and RHEED intensity of the (01) diffraction reflex vs InAs coverage have been reported by Patella *et al.* to support the investigation of surface mass transport at the 2D-3D growth transition of InAs self-assembled QDs (Patella *et al.* 2005).

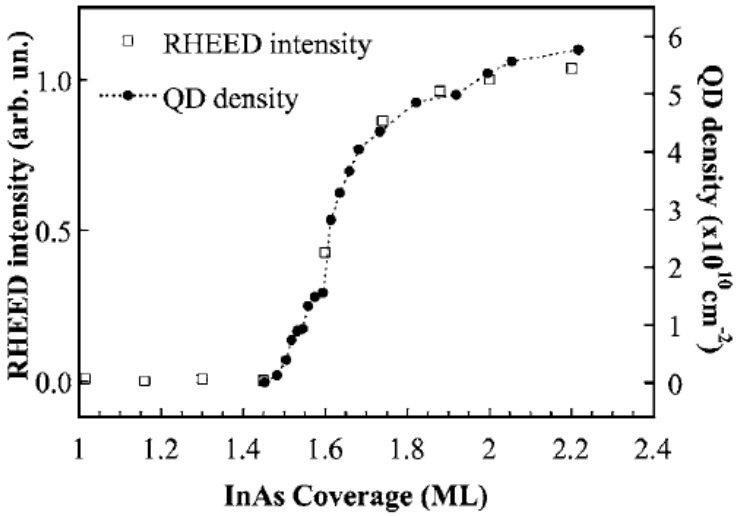

Figure 4.19: RHEED intensity and QD density as a function of InAs ML coverage. The figure is after Patella *et al*. Appl. Phys. Lett. (Patella *et al.* 2005).

As evident from the Figure 4.19, RHEED changes closely follow the QD density changes with InAs coverage. This similarity arise due to each QD, independent of its size, contributes to the transmission diffraction only with a small fraction of its volume at the top. Both intensity and density variations start from equivalent 1.59 ML which is the critical thickness for the nucleation of QDs and within 0.2 ML from this critical limit 3D nuclei are mostly formed triggered by large surface diffusion of cations.

4.3.3.4 RHEED *in-situ* analysis of QD facet orientation

Transmission through nano dots with low index-planes or facets produce chevrons (Miyake 1938). The angle between the chevron tails yields (hkl) miller index plane of a pyramidal facet (Pukite 1988). Angles along $[1\,\bar{1}\,0]$ azimuthal direction have been investigated in earlier reports and proposed facet configurations for those clusters are found to be bounded by $(1\,1\,3)A$ or $(1\,1\,4)A$ facets (Nabetani *et al.* 1994)(Whaley and Cohen 1990).

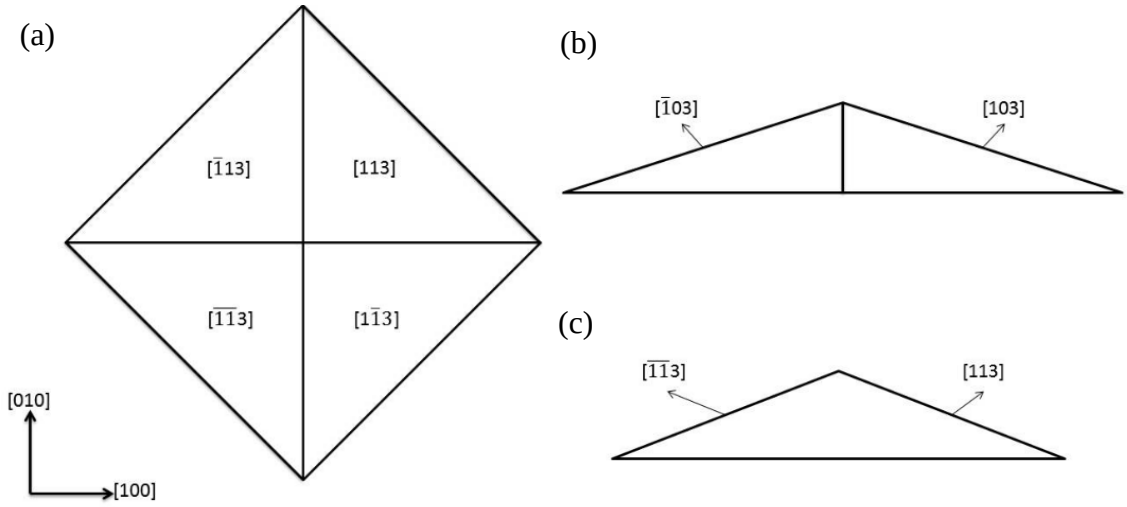

Figure 4.20: (a) The plain view of the pyramid with facets {1 1 3}. The side view from (b) [0 1 0] and (c) $[\bar{1}\,1\,0]$ directions, The figure is reproduced from Ichimiya and Cohen, Cambridge University Press (Ichimiya & Cohen 2004).

The transmission pattern from a (1 1 3) faceted dot is schematically illustrated in Figure 4.20 and the process has been explained by Ichimiya & Cohen (2004). For [0 1 0] incident at a low glancing angle, electrons first strike the pyramid and pass through $(1\,1\,3)$ and $(\bar{1}\,1\,3)$ facets and then refracted into the pyramid and leaves the pyramid through $(1\,\bar{1}\,3)$

and ($\overline{1}\,\overline{1}\,3$) facets respectively. Subsequent trajectories of electron beams are along [1 0 3] and [$\overline{1}$ 0 3] directions.

According to Figure 4.20(c), for incident along [$\overline{1}$ 1 0] direction, electrons enter the pyramid via ($\overline{1}$ 1 3) facet. The electron beams parallel to (1 1 3) and ($\overline{1}\,\overline{1}\,3$) facets are refracted into[$\overline{1}\,\overline{1}\,3$]and [1 1 3] directions. Diffraction patterns for both transmission pattern incident along [0 1 0] and [$\overline{1}$ 1 0] directions are shown in Figure 4.21.

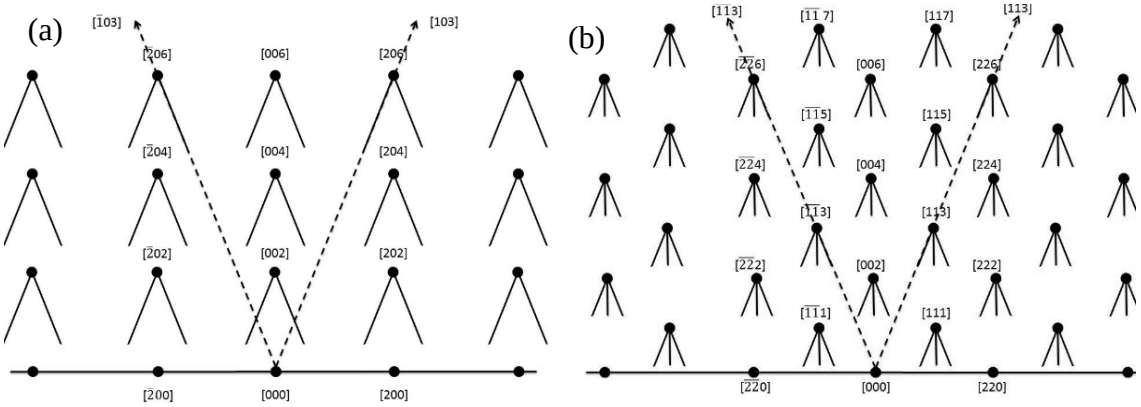

Figure 4.21: Schematic diagram of diffraction patterns from the {113} pyramid: (a) [010] and (b) [$\bar{1}$10] incident. The figure is after Ichimiya and Cohen, Cambridge University Press (Ichimiya & Cohen 2004).

Not only the refraction, the transmission diffraction through the faceted sides after refraction also contributes in chevron formation. If the beams are merely parallel to the facet planes, then the diffraction from exit planes would produce crosses in the diffraction pattern. However, the refraction of incident electron to a higher incident angle when entering the facet planes causes the transmission pattern i.e. each diffracted beam is shifted to lower diffraction angles as implemented in Figure 4.22. Hence, only a portion of the crosses are seen in experimental observations.

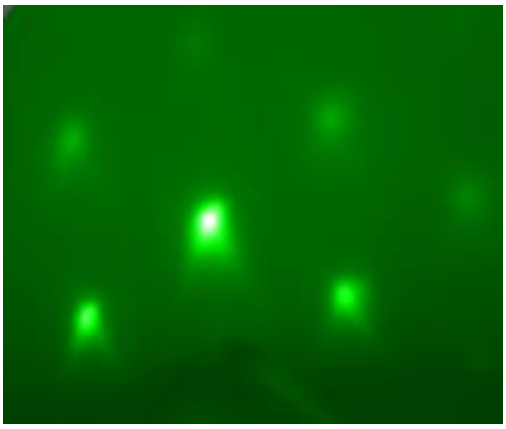

Figure 4.22: RHEED pattern observed during InAs dot growth on GaAs (001) at CAM facility.

The interrelationship between parallel planes and chevron formation provides a feasible approach to determine facets parallel to incident electron direction by calculating the chevron angle and the geometrical representation is given in Figure 4.23.

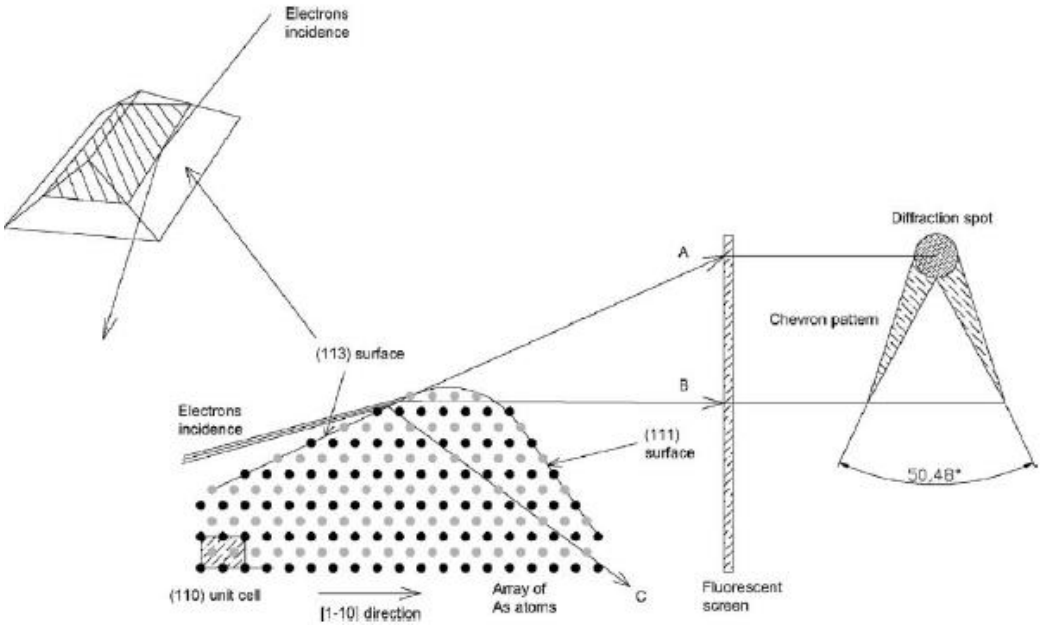

Figure 4.23: The origin of chevron shape and the relationship between parallel facets and the chevron angle. The figure is after Lee *et al*., Appl. Surf. Sci. (Lee *et al.* 2004).

Lee *et al*. (2004) has performed one of the early studies of dot facet extraction from RHEED angles and in the studies he has noted the presence of off-normal streaks directed at an angle 28^0 from the [0 0 1] direction of the diffraction along [3 $\bar{1}$ 0] and [1 $\bar{3}$ 0]. No off-normal streaks had been observed along the orthogonal [3 1 0] and [1 3 0] azimuths. Based on these angles it is concluded that the shape of the quantum dot shape is pyramidal with bounding facets corresponding to a family of four {1 3 6} planes (Lee *et al.* 1998).

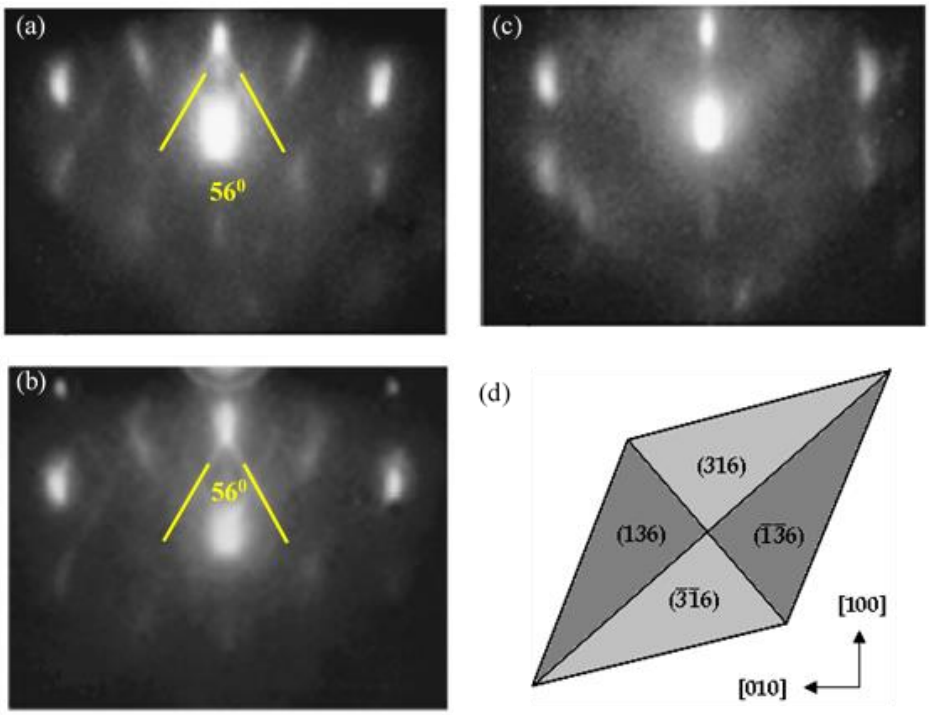

Figure 4.24: RHEED patterns along (a) [3 $\bar{1}$ 0] , (b) [1 $\bar{3}$ 0] and (c) [3 1 0] azimuths. The angles between chevron tails in fig. (a) and (b) are measured to be 56^0. (d) Proposed structure bounded by {1 3 6} facets. The figure is after Lee *et al*., Appl. Phys. Lett. (Lee *et al.* 1998).

Extension of probing of chevron angles while growing has shown to be an effective way to investigate the self –assemble process in real time according to (Kudo *et al.* 2008). When

the QD is surrounded by complicated facets at later stages of growth, the chevron tail structure becomes a superposition of the intensities refracted from those facets. In this respect the one-to-one relation between the tail angle and a certain facet orientation no longer holds true. On that account, the change in the chevron tail structure corresponds to a transition of the facets dominantly contributed to the diffraction signal (Kudo *et al.* 2008).

The growth process is divided in four steps based on the dramatic changes in the chevron angle (Figure 4.25). In the initial growth step A, a round shape spot is observed, and this attributes to the appearance very shallow dot shape. Then, chevron tails appear clearly in the growth step B, which means the formation of specific orientation facets on the island surfaces. The increase in chevron angle is due to transition of dot facets from high-index to low-index planes. In the next growth step C, the chevron angle becomes constant, where the islands are considered to be covered by stable low-index facets. Since the stable low-index facets are difficult to incorporate many In atoms, the assembling process comes to be self-limited, so that highly uniform island growth can be achieved in this growth step. This is evidenced from the height and width profile in Figure 4.25(b) and the AFM image at 2.3ML deposition.

A streak diffraction appears in between the chevron tails in the last growth step D, and the chevron signal intensity becomes weak gradually. Ripening of dots which creates larger QDs with decreased density at the expense of smaller dot (Oswald Ripening) reduces intensity of the chevron tails. The origin of streak lines are from the smooth WL formation in this process.

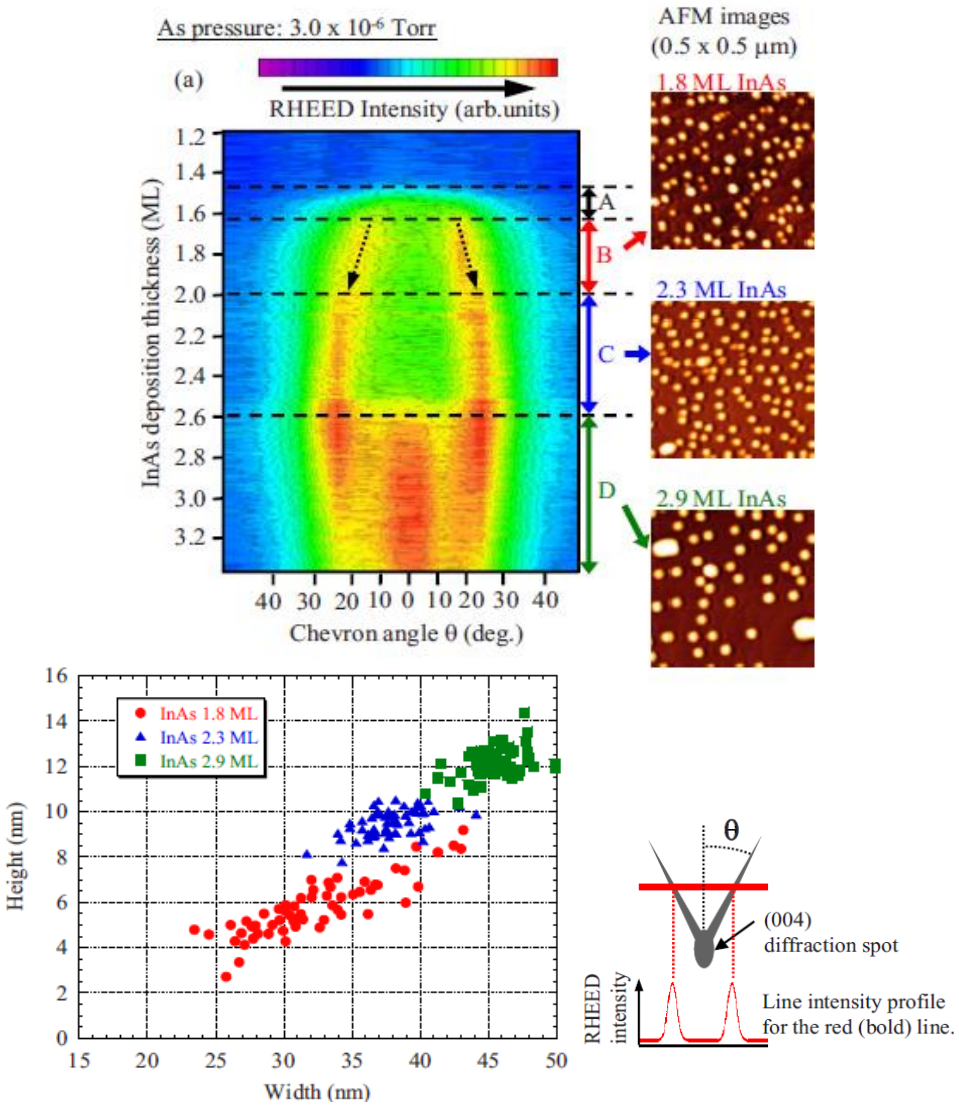

Figure 4.25: (a) Dynamic evolution of chevron angle as a function of InAs coverage deposited at As pressure 3.0 x10-^{6} torr. AFM images taken at each step is shown. (b) Island size distribution at each step and (c) Illustration of a chevron structure. The figure is after Kudo *et al*. J. Appl. Phys. (Kudo *et al.* 2008).

4.4 Summary

The main goal of this chapter is to understand the foundation of diffraction patterns and conditions. Intersection of the reciprocal lattice of a 2D real surface with the Ewald's sphere, which is a geometric construction that demonstrate the relationship between the wave vector of incident and scattered electron beam and the diffraction angle, is described as the origin of diffraction spots. Further the elongation of diffraction spots due to glancing angle which causes the appearance of streak line is also presented.

The main component of the RHEED system in the CAM facility is shown in one of the sections. The final section illustrates the prior studies on the use of RHEED as an *in-situ* analytical tool. There observing 2D WL to 3D island transition and surface reconstructions in terms of diffraction intensities and patterns is reported. Further it is shown that understanding strain relaxation using RHEED is possible.

Moreover, extraction of dot facet configurations based on the relationship between the chevron angles and facets parallel to the incident azimuth of the beam is out lined. An extended step on this is given as the real time probing on chevron angle evolution to understand the growth kinetics at different growth step in dot nucleation.

Chapter 5

Development of RHEED and Prior Work at UH

This chapter presents the state of the progress of RHEED characterization as a real-time *in-situ* technique and the development of RHEED as an analytical tool in our research group at UH will be explained. The use of valence force field (VFF) model for calculating atomic positions and strain dispersions of free standing InAs SKQDs on GaAs(001) is discussed in the first section under strain distribution of InAs/GaAs QDs. Section 5.2 shows the development of RHEED images using kinematical theory. Addition of dependency of atomic scattering factor on scattering vector was a specific contribution of this work. Using the correlations between dot facet arrangement and RHEED chevron angles is used in determining dot shapes and the results are compared to the structures reported in literature. In Section 5.2.2 aims to show the possibility of RHEED in extracting real-time dot height evolution based on intensity profile taken along chevron tails.

5.1 Strain distribution of InAs/GaAs(001) QD

The most natural description of interatomic short-range valence forces in a tetrahedrally coordinated crystal is the Valence-force field approach (VFF). This method has originally been introduced for diamond (Musgrave and Pople 1962) and zincblende structures (Keating 1966). The strength of this model lies in two qualities (Martin 1970),

I. All distortions are described in terms of bond lengths and angles thus the model is automatically rotationally invariant so that serious errors that may arise in the ordinary force-constant approach are avoided.

II. Atom pair bonds is the basis unit in the model and hence it involves the smallest number of parameters.

For zinc blend structures Keating's VFF approach, which includes interactions between nearest neighbors and second next neighbors, is well explained (Pryor *et al.* 1998). In this version the elastic energy U of the crystal is written as a function of atomic position $\{\boldsymbol{R_i}\}$

$$U = U_\alpha + U_\beta, \tag{5.1}$$

where

$$U_\alpha = \frac{1}{2}\sum_i \sum_j^{nn} \frac{3\alpha_{ij}}{8(d_{ij}^0)^2}[\left(\boldsymbol{R_i} - \boldsymbol{R_j}\right)^2 - (d_{ij}^0)^2]^2, \tag{5.2}$$

$$U_\beta = \frac{1}{2}\sum_i \sum_{j,k>j}^{nn} \frac{3\beta_{i,jk}}{8d_{ij}^0 d_{ik}^0}[\left(\boldsymbol{R_j} - \boldsymbol{R_i}\right)X(\boldsymbol{R_k} - \boldsymbol{R_i}) - cos\theta_0 d_{ij}^0 d_{ik}^0]^2 \ , \tag{5.3}$$

where d_{ij}^0 and d_{ik}^0 denote the ideal bond lengths between atom i and j,k, and the equilibrium value takes the form of $d_{ij}^0 = {\sqrt{3}a}/{4}$ in zincblende structures where a is the equilibrium lattice parameter a. θ_0 is the ideal bond angle and for zincblende structures $cos\theta_0 = -1/3$. α_{ij} and $\beta_{i,jk}$ are local-environment-dependent coefficients of bond stretching (U_α) and bond bending (U_β) terms respectively.

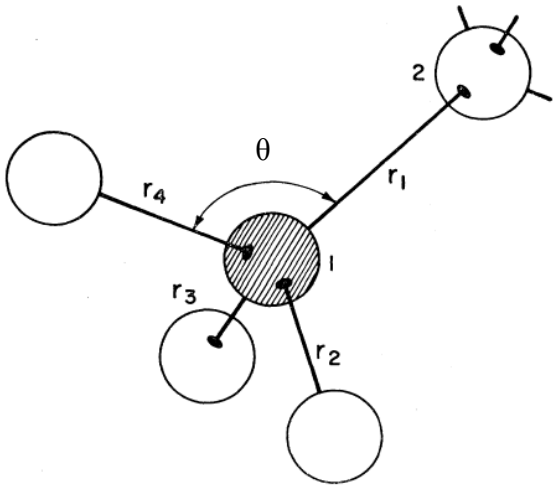

Figure 5.1: The zincblende unit cell with bond length and angle. The figure is after Martin, Phys. Rev. B.

α and β are calculated from the elastic constants of zincblende structures and are noted in Equations 5.4-5.6 (Martin 1970) and the values are given in Table 5.1.

$$C_{11} + 2\,C_{12} = \frac{\sqrt{3}}{4d_{ij}^0}(3\alpha + \beta)\,, \tag{5.4}$$

$$C_{11} - C_{12} = \frac{\sqrt{3}}{d_{ij}^0}\beta\,, \tag{5.5}$$

$$C_{44} = \frac{\sqrt{3}}{4d_{ij}^0}\frac{4\alpha\beta}{(\alpha + \beta)}\,, \tag{5.6}$$

For cubic symmetry only C_{11}, C_{12}, C_{44} are independent and the other elastic constants are zero.

Table (5.1): Ideal bond lengths (d_{ij}^0), elastic constants C_{11} , C_{12} a and $C_{44}$and short-range force parameters (α,β) of bulk GaAs and InAs (Martin 1970).

Material	d_{ij}^0 (Å)	C_{11} (10^{11} dyne/cm^2)	C_{12}	C_{44}	α (n/m)	β
GaAs	2.448	11.81	5.32	5.92	41.19	8.95
InAs	2.662	8.33	4.53	3.96	35.18	5.50

Upon calculation of elastic energy by Equation 5.1 for fixed atomic positions in the strained system the relaxed atomic positions are then calculated by conjugate gradient minimization of *U*.

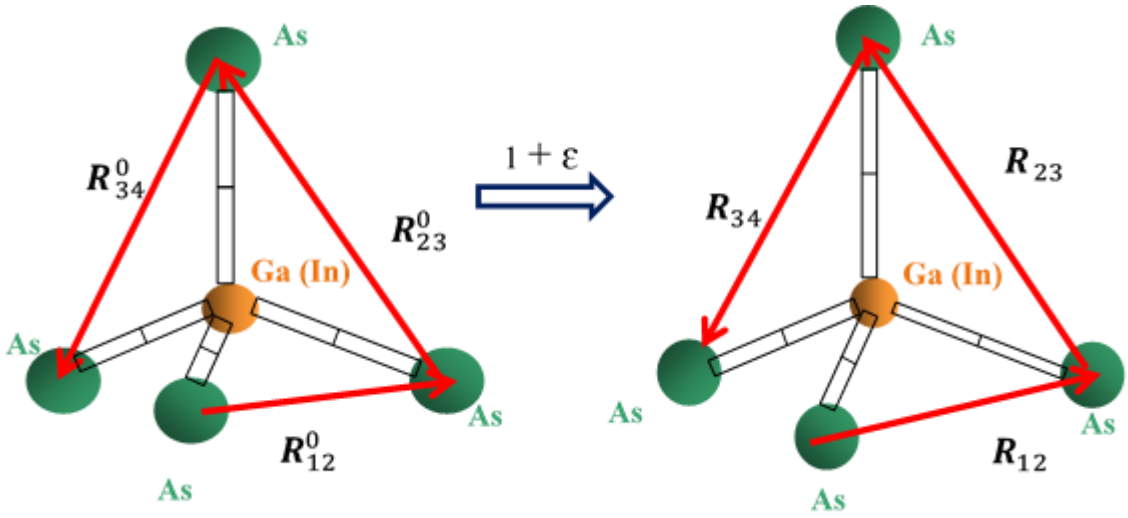

Figure 5.2: Schematic of a distorted tetrahedron after atomic relaxation. The figure is reproduced from Pryor *et al.*, J. Appl. Phys. (Pryor *et al.* 1998).

After atomic relaxation the distorted tetrahedron edges $\boldsymbol{R}_{12}$, $\boldsymbol{R}_{23}$ and $\boldsymbol{R}_{34}$ (refer Figure 5.2) are related to the ideal coordinates $\boldsymbol{R}_{12}^{0}$, $\boldsymbol{R}_{23}^{0}$ and $\boldsymbol{R}_{34}^{0}$ via

$$\begin{pmatrix} R_{12,x} & R_{23,x} & R_{34,x} \\ R_{12,y} & R_{23,y} & R_{34,y} \\ R_{12,z} & R_{23,z} & R_{34,z} \end{pmatrix} =$$

$$\begin{pmatrix} 1+\varepsilon_{xx} & \varepsilon_{yx} & \varepsilon_{zx} \\ \varepsilon_{xy} & 1+\varepsilon_{yy} & \varepsilon_{zy} \\ \varepsilon_{xz} & \varepsilon_{yz} & 1+\varepsilon_{zz} \end{pmatrix} X \begin{pmatrix} R_{12,x}^{0} & R_{23,x}^{0} & R_{34,x}^{0} \\ R_{12,y}^{0} & R_{23,y}^{0} & R_{34,y}^{0} \\ R_{12,z}^{0} & R_{23,z}^{0} & R_{34,z}^{0} \end{pmatrix}, \qquad (5.7)$$

The ideal tetrahedron edges in Figure 5.2 are $\{\boldsymbol{R}^{0}\} = \left\{ [1\ 1\ 0]a/_{2}, [0\ \overline{1}\ 1]a/_{2}, \overline{[1\ 1\ 0]}a/_{2} \right\}$.

From Equation 5.7 the local strain tensor is then calculated by

$$\begin{pmatrix} \varepsilon_{xx} & \varepsilon_{yx} & \varepsilon_{zx} \\ \varepsilon_{xy} & \varepsilon_{yy} & \varepsilon_{zy} \\ \varepsilon_{xz} & \varepsilon_{yz} & \varepsilon_{zz} \end{pmatrix} = \begin{pmatrix} R_{12,x} & R_{23,x} & R_{34,x} \\ R_{12,y} & R_{23,y} & R_{34,y} \\ R_{12,z} & R_{23,z} & R_{34,z} \end{pmatrix}$$

$$X \begin{pmatrix} R_{12,x}^{0} & R_{23,x}^{0} & R_{34,x}^{0} \\ R_{12,y}^{0} & R_{23,y}^{0} & R_{34,y}^{0} \\ R_{12,z}^{0} & R_{23,z}^{0} & R_{34,z}^{0} \end{pmatrix}^{-1} - I \ , \qquad (5.8)$$

where I is the identity matrix.

A cross sectional and top view of relaxed atomic positions of an ideal uncapped $\{1\ 3\ 6\}$ bounded 3nm height InAs QD on GaAs(001) calculated by minimizing U in Equation 5.1 is shown in Figure 5.3. Green dots represent As atoms and orange dots are for Ga/In atoms.

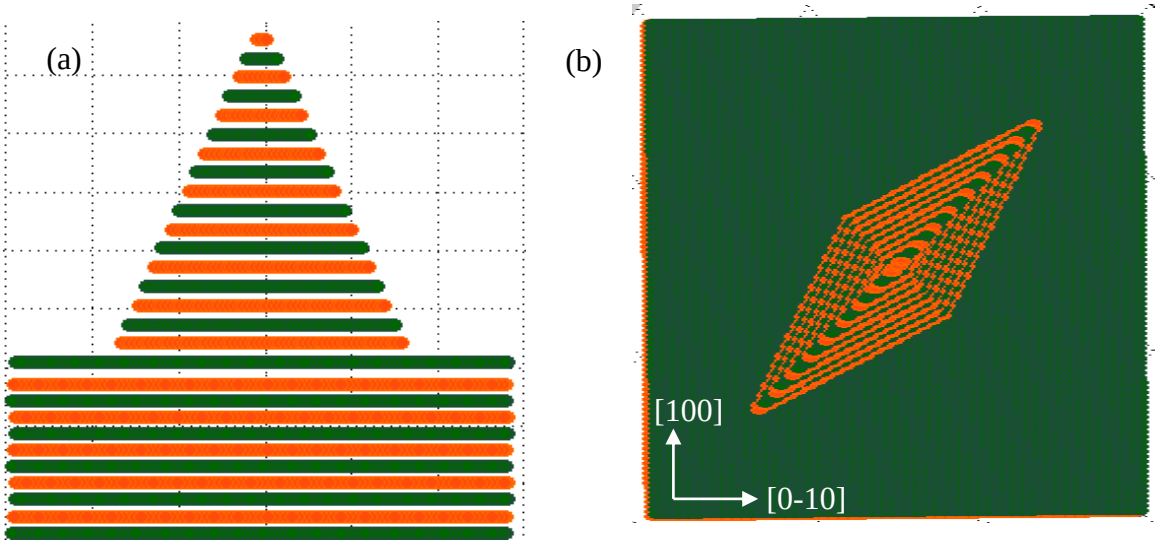

Figure 5.3: Calculated {136} bounded facets QD structure of 3nm height. (a) Cross-sectional view and (b) top view of QDs.

A schematic diagram of the dot is included above in Figure 5.4 to illustrate the planes and axis in which the strain components are calculated.

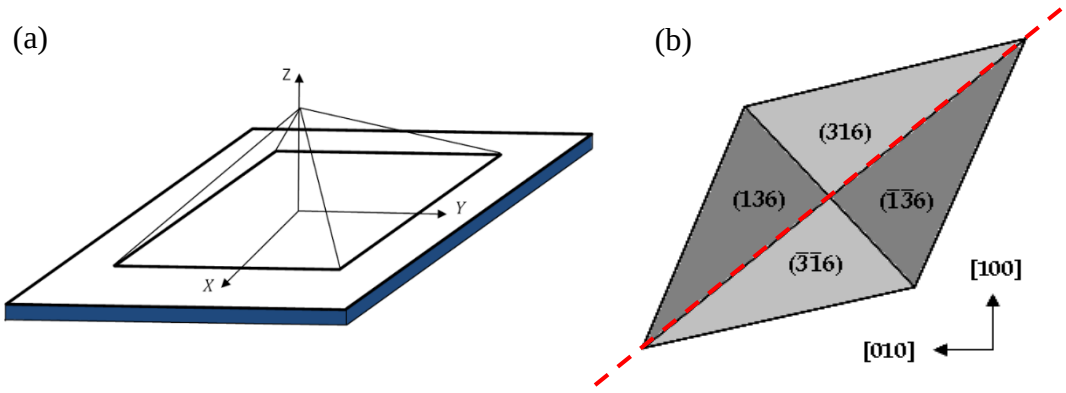

Figure 5.4: (a) Schematics of dot geometry in which the strain components are calculated and (b) Figure 5.5 is calculated along the plane across red dotted line.

ε_{xx} and ε_{zz} components of local strain of In/Ga atom as a function of position along [001] azimuth is calculated using Equation 5.8. The resultant strain profiles are graphed in Figure 5.5.

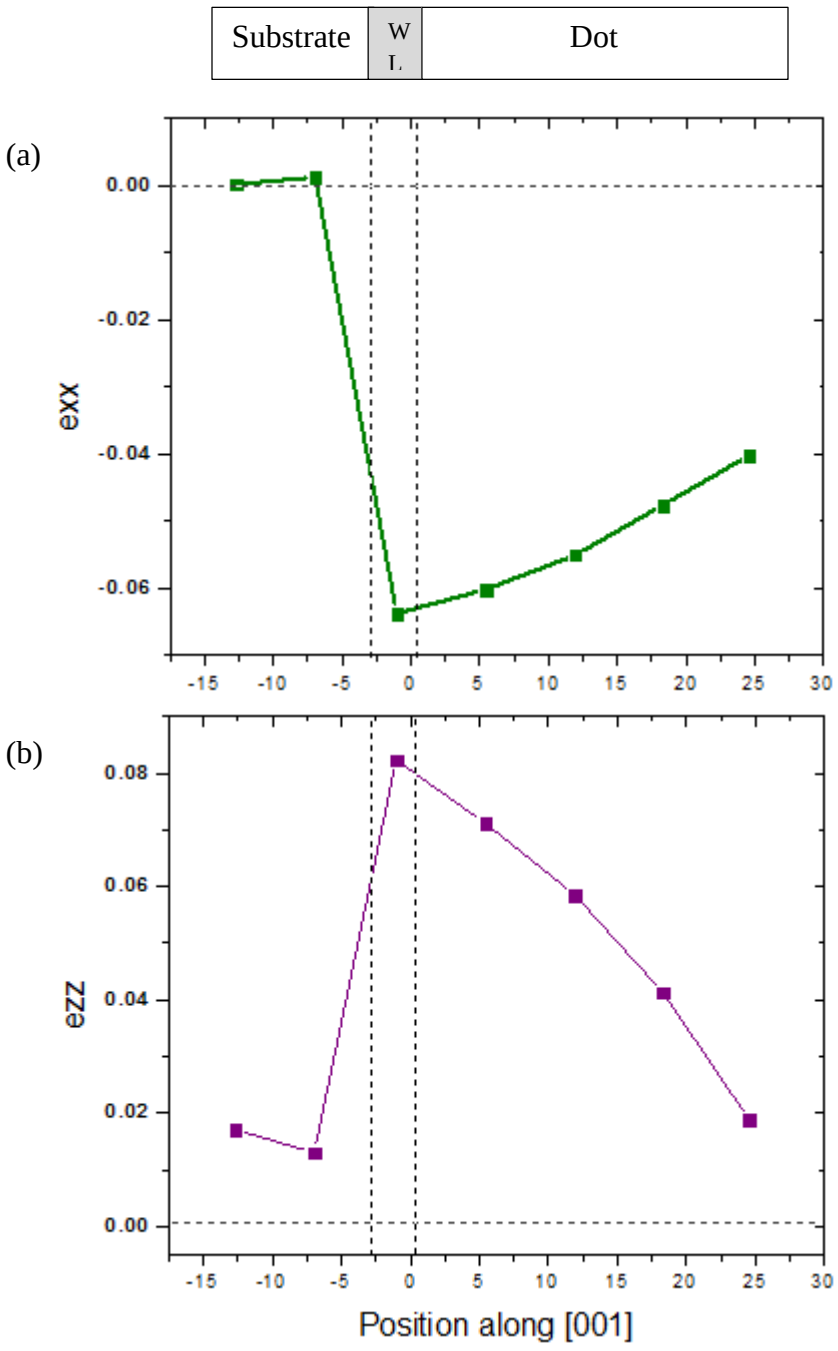

Figure 5.5: Strain profiles along [0 0 1] azimuth for uncapped InAs QD on GaAs(001).

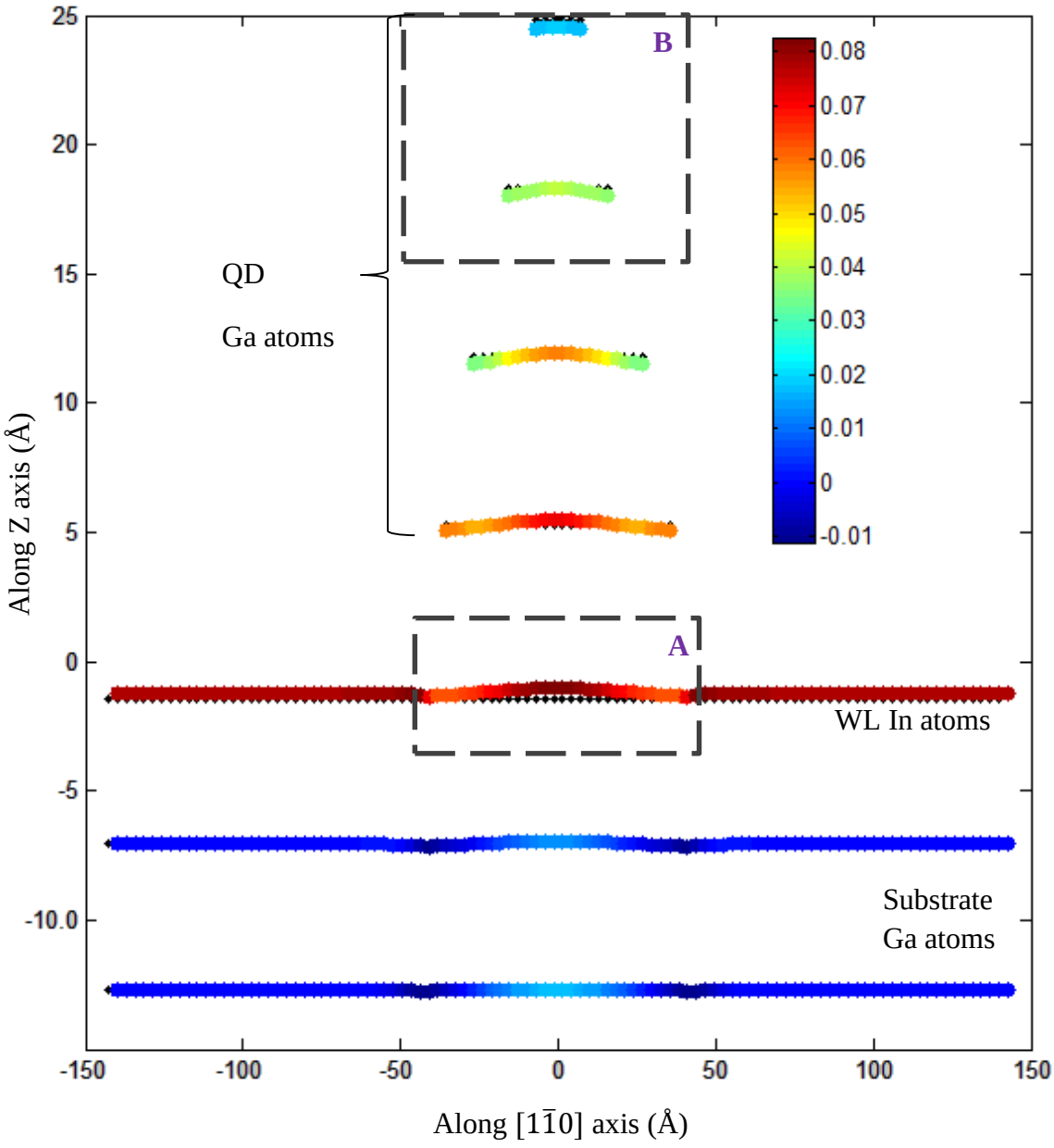

Figure 5.6: Calculated strain profile along a plane across origin of the QD. Ideal Ga/In atomic positions are indicated in black. The solid colored circles represent displaced Ga/In atomic positions due to relaxation. The amount of strain is expressed in color shown in the color bar.

Both the ε_{xx} and ε_{zz} components of Ga atoms in the substrate experience a positive (tensile) strain in the substrate. In the WL region, In atoms undergo a tensile strain ($\varepsilon_{xx}>0$) in the x direction and compressive strain ($\varepsilon_{zz}>0$) along z azimuth due to the effects from lattice mismatch. With increasing dot height in the uncapped QD region, both ε_{xx} and ε_{zz} components decrease as the atoms occupy more freedom to relax.

The strain profile on the plane shown in Figure 5.4(b) is calculated next in Figure 5.6. The displacements of atomic positions in the relaxed system are compared with the strained system and the color bar represents the percentage of strain the atoms undergo.

The strain in the WL is biaxial in nature. Compressive (negative) interfacial strain causes an expansion along the z direction ($\varepsilon_{zz} >0$). The WL is affected by the QD only in its vicinity of the dot base.

A closer look on In atoms in the WL region at the dot facet boundaries and Ga atoms inside QD structure are shown in Figure 5.7.

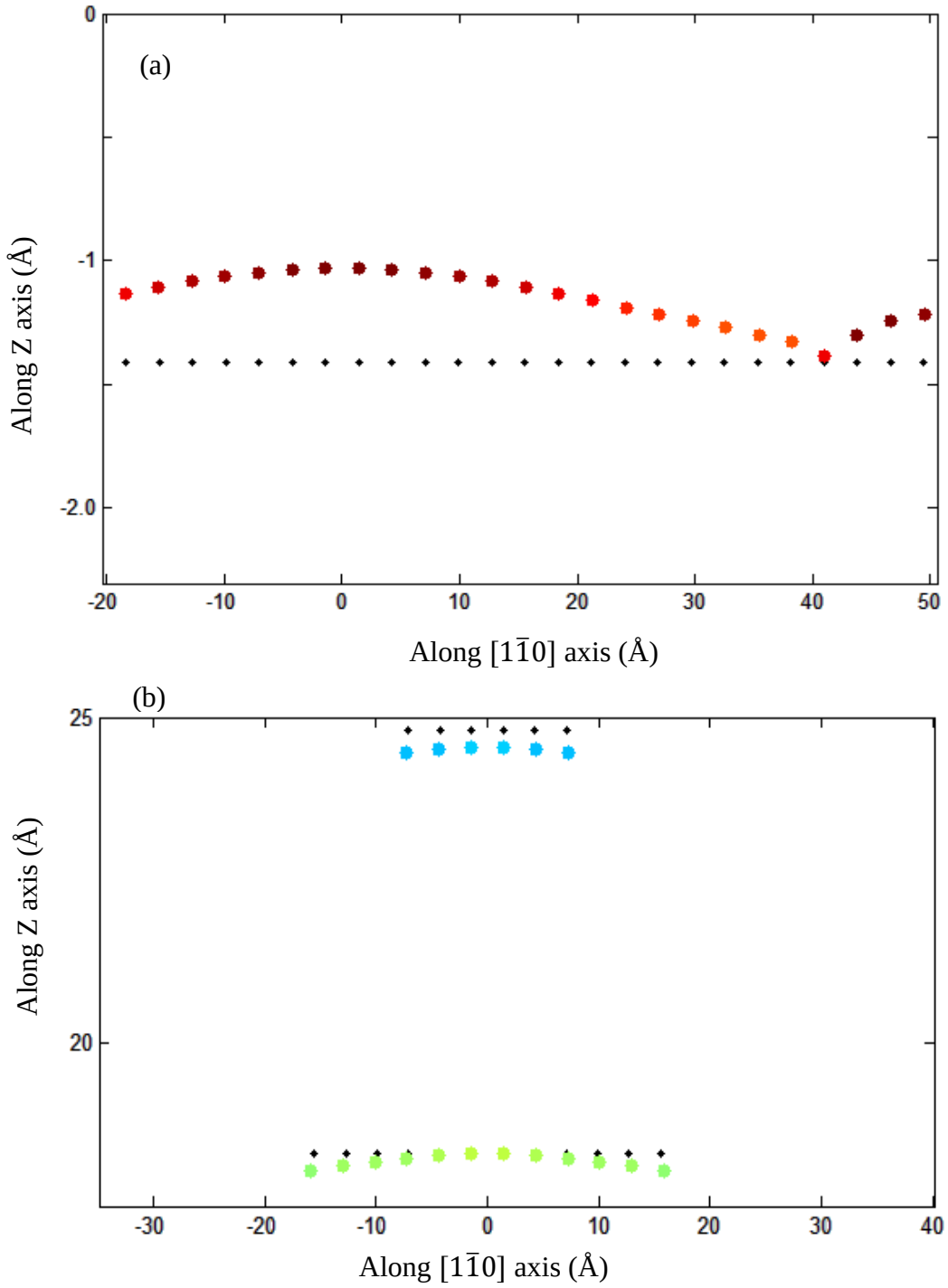

Figure 5.7: Magnified images of inserts (a) A showing the atomic distortions along Z axis and (b) B showing distortions in both directions.

5.2 Simulation of RHEED images

The modeling of the RHEED diffraction pattern is based on kinematic electron diffraction theory and takes the effect from atomic vibrations into account (Ichimiya & Cohen 2004) (Feltrin and Freundlich 2007b). The time-averaged diffracted intensity, <I(s)> tensor is written as follows:

$$< I(s) >= |f(s)|^2 X exp(-4\omega) X \sum_{i,j} \exp\left[i\boldsymbol{s}.\left(\boldsymbol{R}_i - \boldsymbol{R}_j\right)\right]$$

$$+ N|f(s)|^2 X\{1 - \exp(-4\omega)\}, \quad (5.9)$$

where $\boldsymbol{R}_i$ is the position of the i^{th} atom, $\boldsymbol{u}$ is the deviation from the mean equilibrium lattice position, N represents the number of atoms that undergo scattering and $\boldsymbol{s}$ is the scattering vector.

The $exp(-4\omega)$ describes the effects of thermal vibrations and is calculated using the Debye-Waller parameterization factors (Rajapaksha and Freundlich 2009).

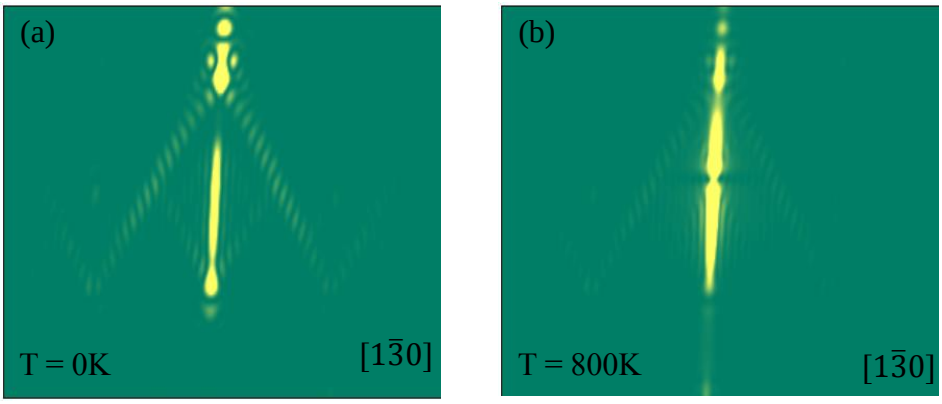

Figure 5.8: RHEED images simulated for InAs SK QDs on GaAs using kinematical theory to imply the effect of temperature. The incident azimuth is along [1 $\bar{3}$ 0] and the temperatures at which the calculations were done is (a) 0K and (b) 800K.

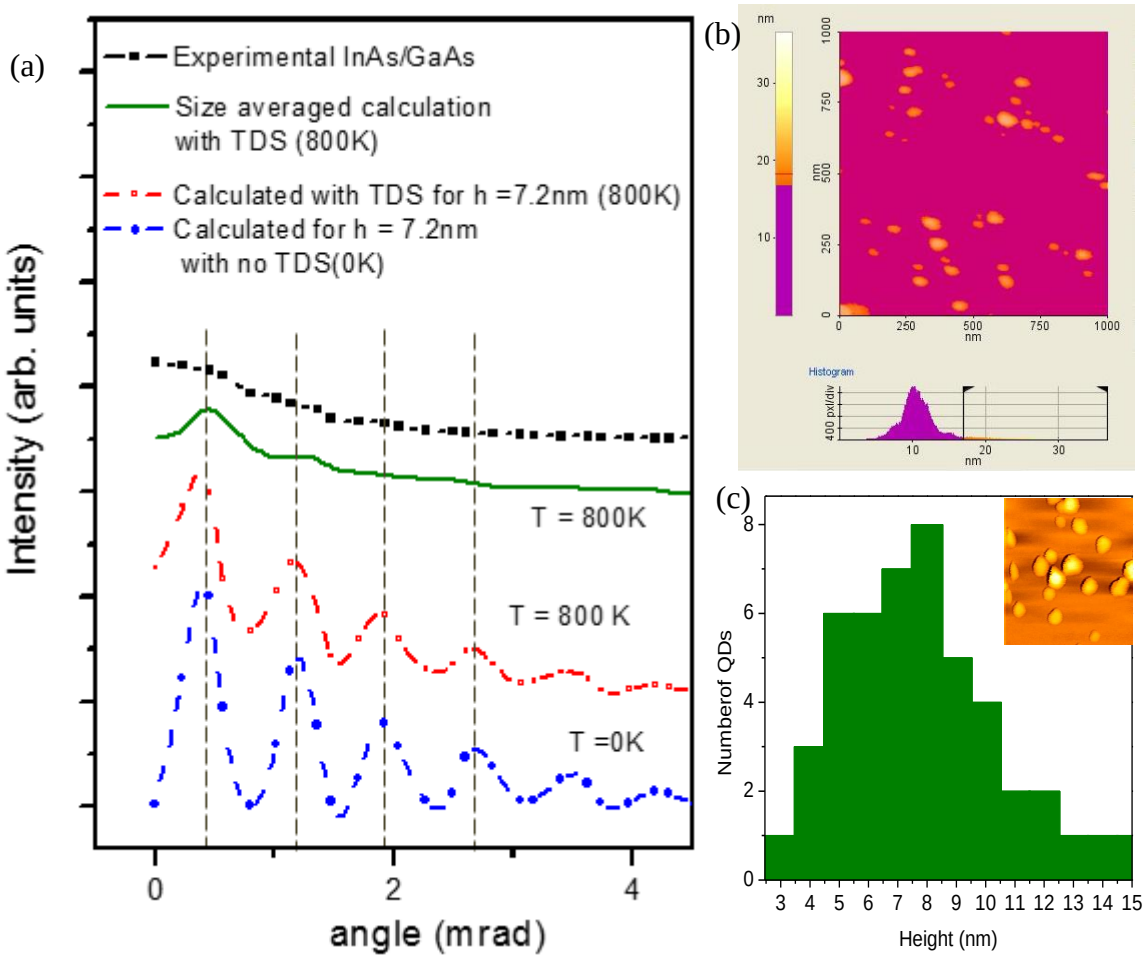

Figure 5.9: RHEED intensity profiles along chevron tail of self-assembled InAs/GaAs dots along [1 $\bar{3}$ 0] azimuth: observed and calculated for a dot of height 7.2 nm both with and without thermal diffuse scattering. Intensity profiles of calculated size averaged QD structure at 800 K (using the size dispersion shown in (c)) and real time measured diffraction tail at 480C are exhibited. (b) & (c) Size distribution of self-assembled InAs/GaAs (001) dot sample obtained by post growth AFM.

RHEED intensities along chevron tail calculated with and without inclusion of the effects of thermal diffuse scattering of electrons and chevron intensity for QDs calculated with size dispersion is shown in Rajapaksha & Freundlich (2009) for a comparison with experimental observations. The average size of the QDs in the sample obtained from AFM data has been used for RHEED calculations. The calculated intensities for size averaged

sample were found to be in good agreement with the experimental observations. These results point out that the average height of QDs can be estimated during the growth using RHEED intensity profiles along chevron tail. The broadening of the intensity peaks is found to be associated with the size distribution of the dots. This implifies the possibility of extracting the average dot height as a function of growth time during the fabrication of QDs from RHEED.

The strength of the interaction is recently included in this work by means of atomic scattering factor *f(s)* which is evaluated from Doyle-Turner parameterization and f(s) is given by

$$f(s) = \sum_{j=1}^{4} a_j \exp\left[-b_j \left(\frac{S}{4\pi}\right)^2\right]. \qquad (5.10)$$

The Doyle-Turner coefficients a_j and b_j are listed Appendix A.

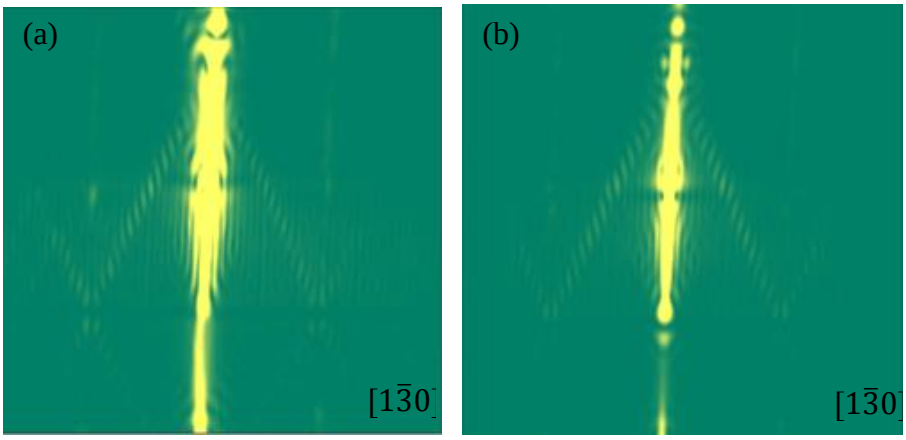

Figure 5.10: RHEED images along [1 $\bar{3}$ 0] direction (a) with constant *f(s)* and (b) scattering vector(**s**) dependent atomic scattering factor calculated by Equation 5.10.

Addition of the scattering vector ($\boldsymbol{s} = \boldsymbol{k} - \boldsymbol{k}_0$) dependent atomic scattering factor (*f(s)*) improves the diffraction pattern by eliminating diffraction noises as shown in Figure 5.10.

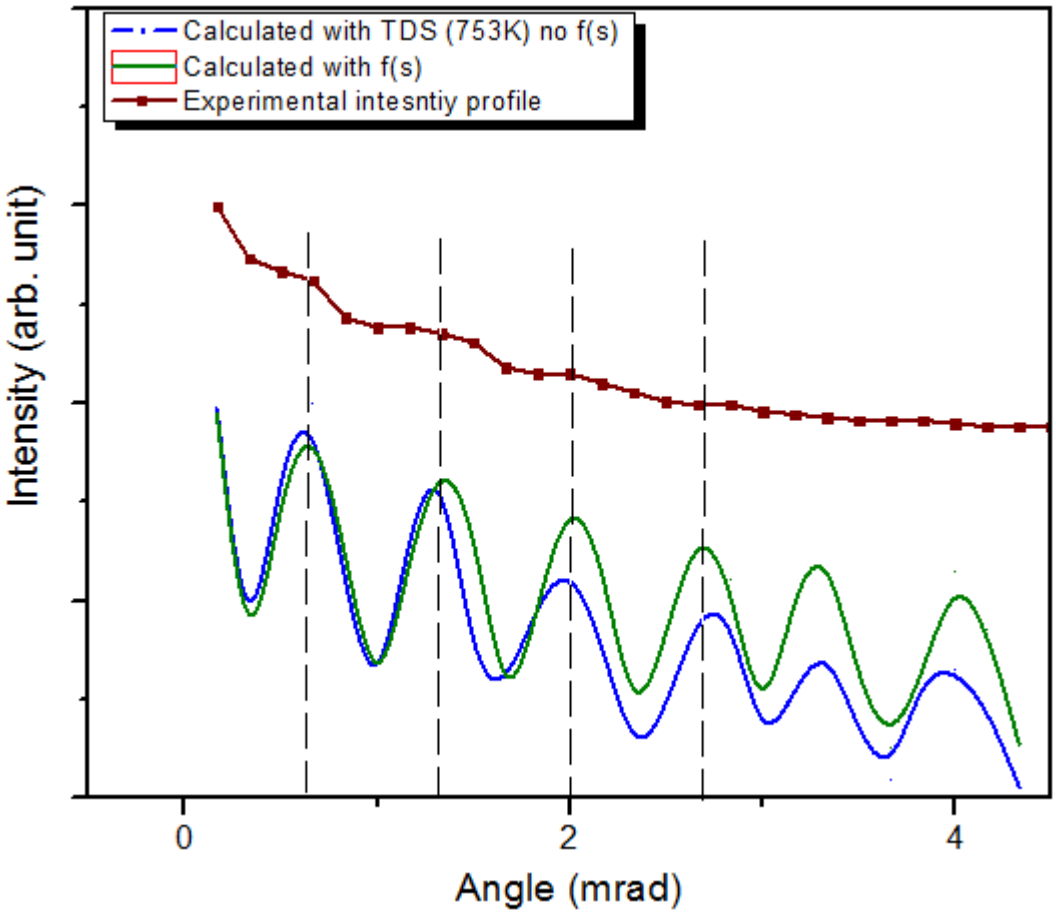

Figure 5.11: RHEED intensity profiles along [1 $\bar{3}$ 0] direction for calculated QDs with scattering vector(**s**) dependent atomic scattering factor *f(s)* (green solid line) and constant *f(s)* (blue solid line) calculated by Equation 5.10. The experimental observation is represented by maroon line with symbols.

The calculation for thermal scattering described above in Figure 5.9 where constant *f(s)* are used, and the calculation which included scattering vector dependent scattering vector are then compared to the experimental observations as shown in Figure 5.11. RHEED images were calculated for a QD of 7.2 nm height with {1 3 7} and {$\overline{1\ 3\ 5}$} facets.

Improvement of intensity values and comparable periodicities to the experimental observations are observed in the refined simulation. The shape of decay of the intensity closely follow the experimental behavior which cannot be seen in the calculation with constant *f(s)*.

5.2.1 Identification of dot facet orientation

The chevron angle of the diffraction pattern is at fundamental importance of providing a relationship to identify facet orientation of a QD. This correlation has clearly stated in Feltrin & Freundlich (2007b) for QDs bounded with (11x) for x= 1:1:5 and the inverse of the tangent of the half-chevron angle vs the facet orientation used in that study is shown in Figure 5.12.

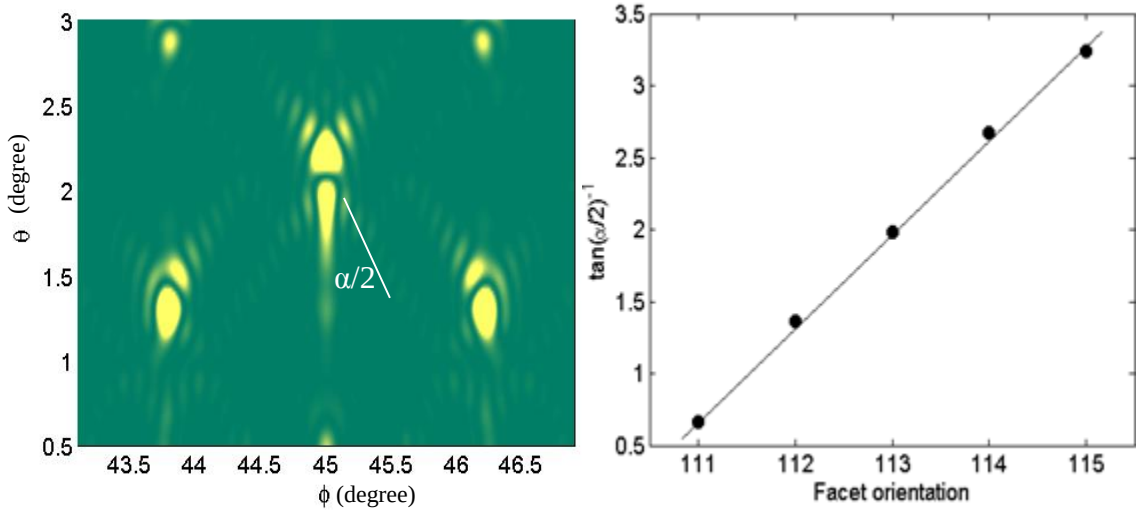

Figure 5.12: (a) RHEED half chevron angle α/2 of a pyramidal QD with (1 1 3) facet boundaries. (b) Linear correlation between the inverse tangent of half chevron angle and (1 1 x) facet planes where x = 1:1:5 (Feltrin and Freundlich 2007b).

The above correspondence has recently been applied to construct a complete shape profile of a small InAs quantum dot. STM and RHEED investigations in literature on determining individual dot facet plane has been used as a reference in the study done by Rajapaksha & Freundlich (2009).

The RHEED images observed for experimentally grown QD shown in the AFM image in Figure 5.13(a) are calculated to be of chevron angles 56^0 along $[1\,\bar{3}\,0]$, 50^0 along $[1\,\bar{1}\,0]$ and a streak line along $[1\,1\,0]$. Determining of dot facet configuration for corresponding quantum dots have been carried out first with comparing the proposed structures for smaller dot sizes in literature. For islands at the beginning of nucleation {1 3 7} planes are found to be stable in the investigation of Xu *et al*. (2005) based on STM studies (Xu *et al*. 2005).The simulated image along [1 1 0] does not agree with the observed. The next comparison has been performed for QD structure terminated by {1 3 7} and $\{\overline{1\,1\,1}\}$ facets suggested by Kratzer P. and collaborators (Kratzer *et al.* 2006) A significant discrepancy in the RHEED analysis is noticed between experimental and calculated observations as indicated in Figure 5.13(b). The RHEED determination of {1 3 6} plane boundaries in QD pyramidal geometry described in Lee *et al*. (1998) (Figure 5.13(c)) does not yield characteristic chevrons observed in $[1\,\bar{3}\,0]$ and [1 1 0] crystallographic directions in Figure 5.13(a).

(a) Experimental observations

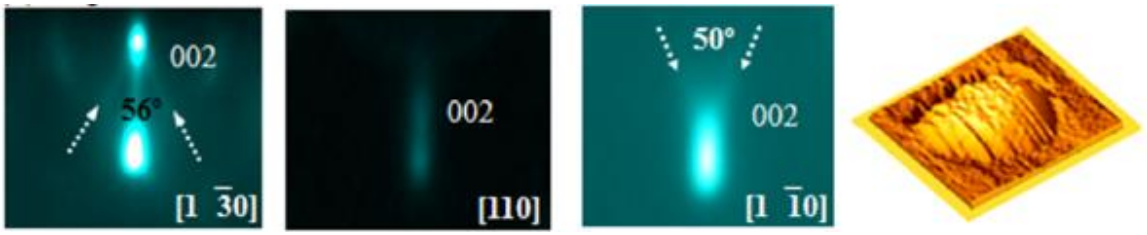

(b) Calculated for proposed model of Xu *et. al*., 2005

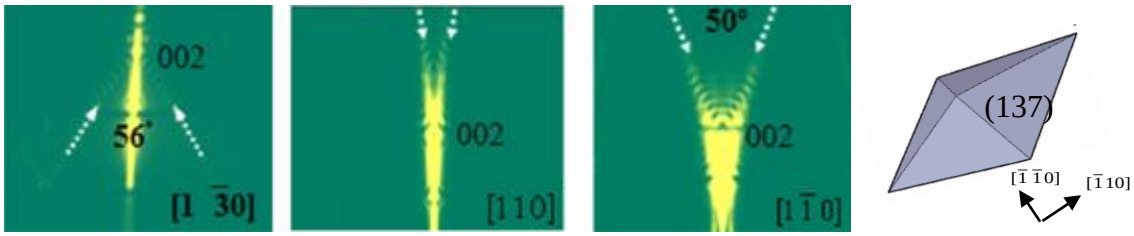

(c) Calculated for proposed model of Kratzer *et. al*., 2006

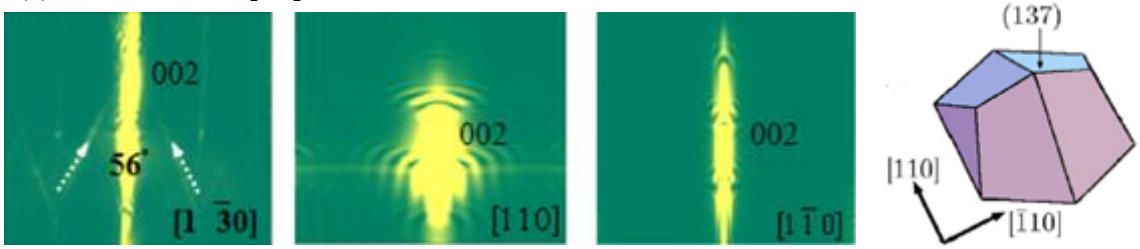

(d) Calculated for proposed model of Lee *et. al*., 1998

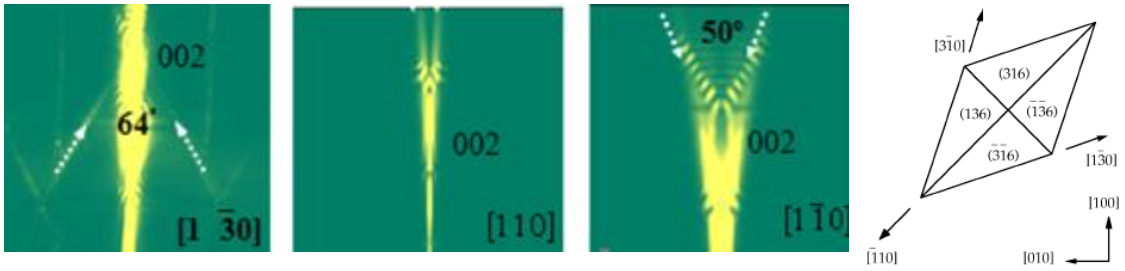

Figure 5.13: RHEED images along [1 $\bar{3}$ 0] , [1 1 0] and [1 $\bar{1}$ 0] for (a) InAs/GaAs(001) CBE growth QD at 480^{0}C, (b) dot structure bounded by {1 3 7} facets by Xu *et al*., (2005), (c) QD with {1 3 7} and {$\bar{1}$ $\bar{1}$ $\bar{1}$} facets by Kratzer *et al.* (2006) and (d) {1 3 6} bounded QD structure by Lee *et al*. (1998).

The initially proposed structure for the observations was faceted with {1 3 7} and {1 1 2} planes by Rajapaksha & Freundlich (2009). Our newer calculations in Figure 5.14 show that the facets are {1 3 7} and {1 1 3} (Gunasekera and Freundlich 2013). The angle of 56^0 from {1 3 7} planes along [1 $\bar{3}$ 0] and 50^0 angle from (1 1 3) facets along [1 $\bar{1}$ 0] azimuths are in good agreement with literature reports (Heyn *et al.* 2007).

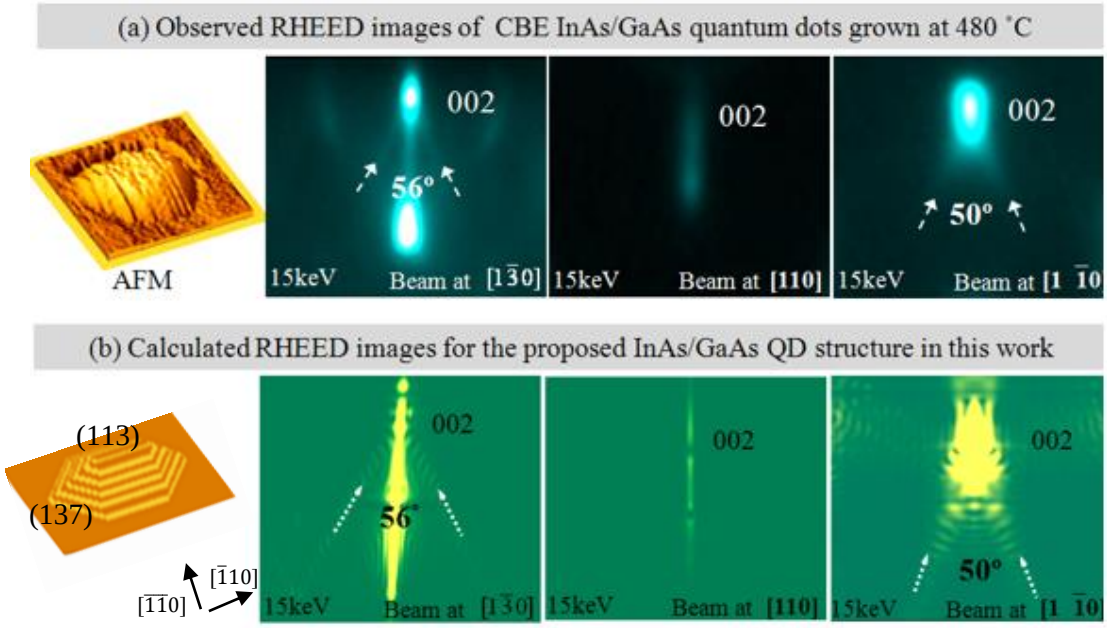

Figure 5.14: (a) RHEED geometry of CBE grown InAs SK QD along three main azimuths[1 $\bar{3}$ 0], [1 $\bar{1}$ 0] and [1 1 0] and (b) calculated RHEED images for the proposed {1 3 7} and {1 1 3} faceted dot structure.

5.2.2 Real-time evolution of dot size from RHEED

RHEED intensity profile along chevron tail reveals a set of periodic fringes which is discovered to be associated with the average dot height of a dot sample and the nonuniformity of the dot sizes are accredited for broadening of the peaks (Feltrin and Freundlich 2007b).

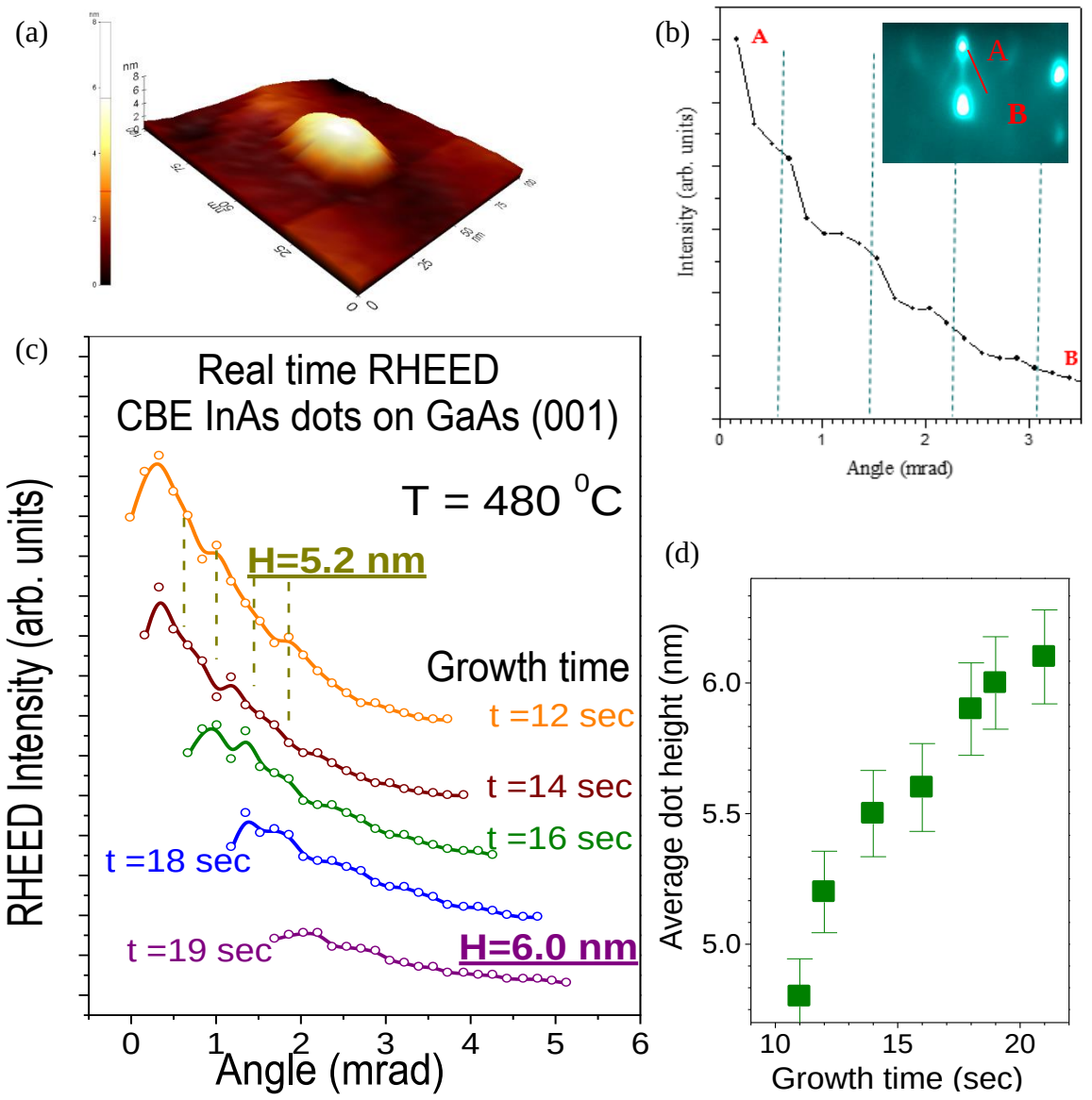

Figure 5.15: (a) AFM image of CBE grown InAs/GaAs QD and corresponding (b) intensity profile along chevron angle showing equally spaced fringes, (c) intensity profiles at different growth stages and (d) average dot heights extracted from fig. (c).

The periodicity of the intensity fringes in Figure 5.15 (c) decreases with the increasing growth time indicating the increasing size of the dots. The height of the dots remain almost constant initially and then exhibits a linear increase. This indicates a critical dot height

where dots start to grow laterally, probably by adding more side facets. After this critical height, dots have reached an equilibrium shape or a critical diameter at which point the dots grow predominantly vertically or by stacking on the existing facets (Rajapaksha & Freundlich 2009).

5.3 Summary

The development of theoretical model we use to analyze dot morphology is illustrated here. Calculations of atomic positions using VFF model and simulation of RHEED images using kinematic theory are explained. A structure for a smaller quantum dot is proposed by analyzing RHEED chevron angle at three major crystallographic directions $[1\,\bar{3}\,0]$, $[1\,\bar{1}\,0]$ and $[1\,1\,0]$. From the calculations and comparisons with structures reported in literature the dot has found to be {1 3 7} and {1 1 3} faceted. The relationship between dot average height and the periodic fringes on intensity profiles along chevron tails is stated and its use for extracting dot height evolution during growth is illustrated.

Chapter 6

RHEED Analysis at the Onset of Dot Formation and Evidence on Asymmetric Dot Facet Configuration

The purpose of this chapter is three -fold: First, in section 6.1 the experimental process of MBE fabrication of InAs QDs on GaAs(001) will be given. In the next section we will demonstrate the RHEED analysis of real-time dot shape evolution by probing chevron angles. A discussion on extracting a very small chevron angle which was not reported in literature so far will be highlighted. Further the proposed dot facet orientations at different growth stages will also be presented based on theoretical calculations and the validity of the results will be also will be discussed using reports in literature. An interesting phenomena we came across during this analysis will be the body of the next section. In Section 6.3 the evidences of asymmetric dot facet formation at the onset of dot nucleation will be demonstrated.

6.1 Fabrication of InAs/GaAs (001) quantum dots

The development of InAs QDs are carried out using Riber 32C™ UHV molecular beam epitaxy chamber. 12 keV Staib™ RHEED gun is mounted to a 4.5" CF flange and the flange is fully coated with a phosphorus layer which help with the fluorescence effect. The resulting diffraction images on the screen is acquired by a CCD (charged-coupled device) camera, and data are processed via KSA 400 software.

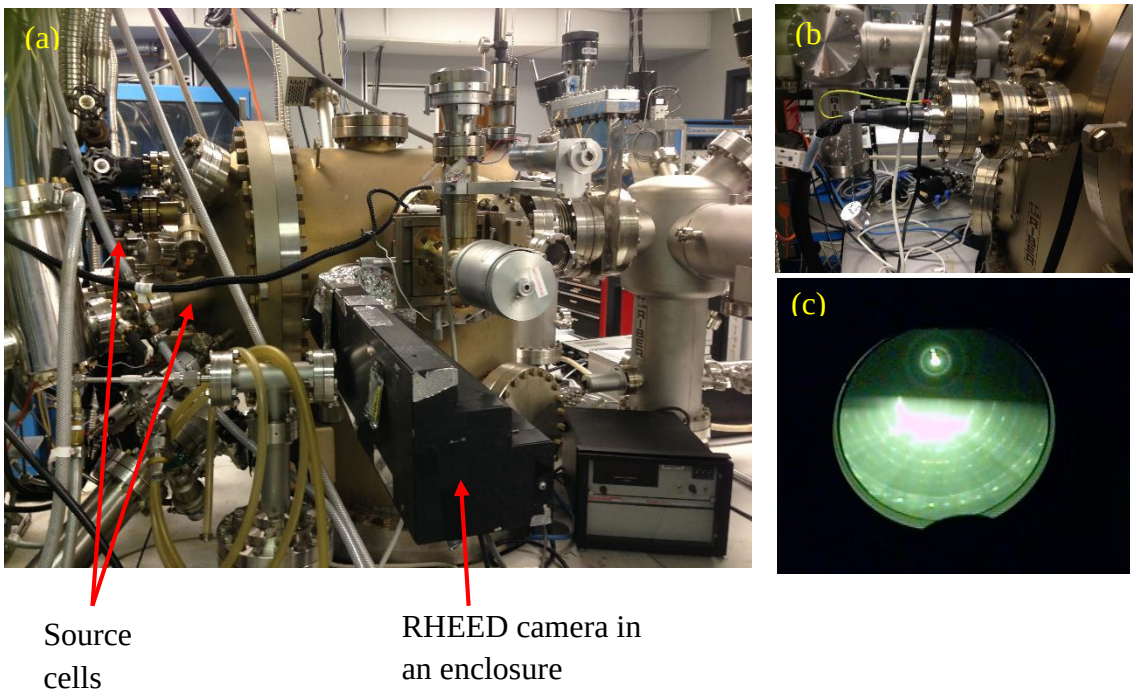

Figure 6.1: (a) Riber 32C™ UHV MBE chamber at CAM facility, (b) 12 keV Staib™ RHEED gun mounted to the chamber and (c) RHEED pattern on fluorescence screen.

Prior to the epitaxial deposition in MBE, semi-insulated GaAs(001) substrates are degassed at 180^0C in a separate vacuum enclosure to remove water vapour and other atmospheric gases. This phenomena was observed from RHEED images where the x2 lines starts appearing along $[\overline{1\,1}\,0]$ azimuth and 3D spots will be observed along $[1\,\overline{1}\,0]$

direction. Then the substrate is transferred to the epitaxy chamber and the native oxide layer on the substrate surface is thermally removed at 580^0C under As_2 overpressure. Much lesser sticking coefficient of elemental arsenic than that of Ga (which is unity) and highly reactive nature of Ga at higher temperatures are the reasons for maintaining a constant As_2 over flux during growth such that the stoichiometric ratio of the constituent elements will be preserved.

The epitaxial growth of InAs on GaAs (001) is initiated by growing a GaAs buffer layer of 0. 3-0.5μm is grown at a growth rate of 1ML/s at 560^0C. Required layer thickness of InAs is deposited on GaAs buffer layer at temperatures 440^0C and 480^0C at a growth rate of 0.05 ML/s. Quantum dot heterostructures at intermediate layers are capped by 100nm thick GaAs layer to avoid strain effects from dots below. The surface QD layer is left upcapped under As_2 pressure until the sample temperature drops to 200^0C. The RHEED data acquisition is carried out during the growth at crystallographic directions$[\overline{1\,1}\,0]$, $[1\ \bar{1}\ 0]$ and $[1\ \ 0]$. AFM and TEM analysis are followed postgrowth.

6.2 Evolution of dot facet orientation at the onset of dot formation

Extracting data from RHEED patterns in real time provides a reliable interpretation of understanding quantum dot morphology. RHEED characterization of dot facet orientation and average dot height (refer chapter 5) is used in this section to examine evolution of dot shape (facet orientation) and average height distribution during island ripening. Here, we have explicitly studied the change in structural behavior at the onset of dot formation.

Several structures have been investigated in literature to identify the shape of fully grown quantum dots and in recent years our group proposed a structure bounded by {1 3 7} and {1 1 3} facet orientations for average size quantum dots (7 nm height) (Gunasekera and Freundlich 2012). Here an extended detailed analysis on QD shape evolution is performed using RHEED. In fact RHEED chevron angle evolution of InAs QDs along [1 $\bar{1}$ 0] azimuth is studied at the initial growth stages in terms of growth stages as shown in Figure 6.2. The inserts of the figure are for dots grown at 440^0C.

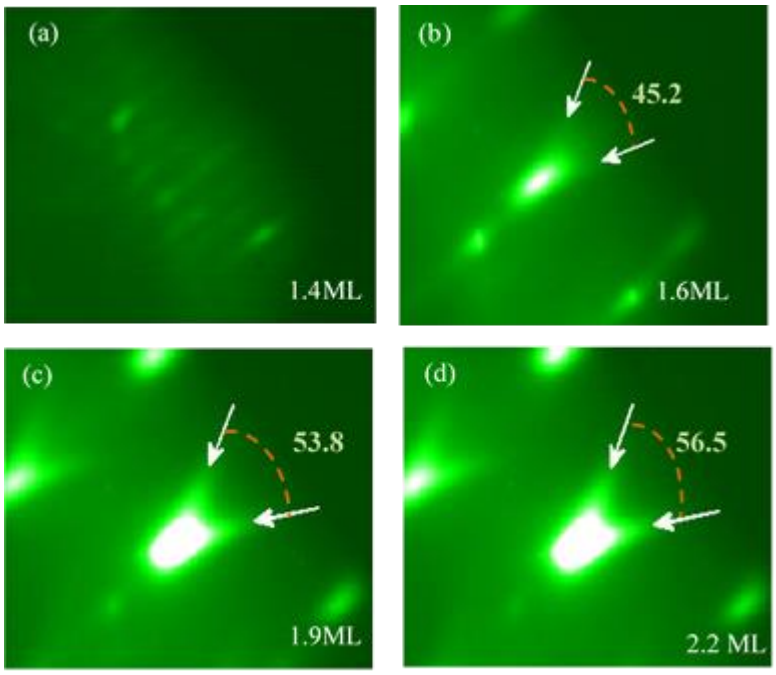

Figure 6.2: (a) RHEED image of InAs wetting layer before the formation QDs grown at 440^0C. (b)-(d) Evolution of InAs/GaAs quantum dot chevron angles along [1 $\bar{1}$ 0] azimuth as a function of InAs monolayer deposited.

An increase in chevron angle of (002) diffraction spot was monitored during QD growth by probing multiple images taken by KSA 400 software. At 1.5ML InAs monolayer deposition RHEED pattern change from 2D lines to 3D spots at the onset of island

formation. Further deposition creates smaller quantum dots and numerous spectroscopic investigations establish that the InAs quantum dots are predominantly bounded by {1 3 7} facets which we also have confirmed in a separate study. Measured RHEED angular values are displayed in Figure 6.3as an implementation of temperature gradients.

Higher enhanced In migration and faster coarsening at higher temperatures, 480^0C cause QDs to nucleate faster than at lower temperatures, 440^0C. The angular evolution at both 440^0C and 480^0C as shown in Figure 6.3 (a) are in agreement with transition of QD shape from shallower bounded facets to steeper facets.

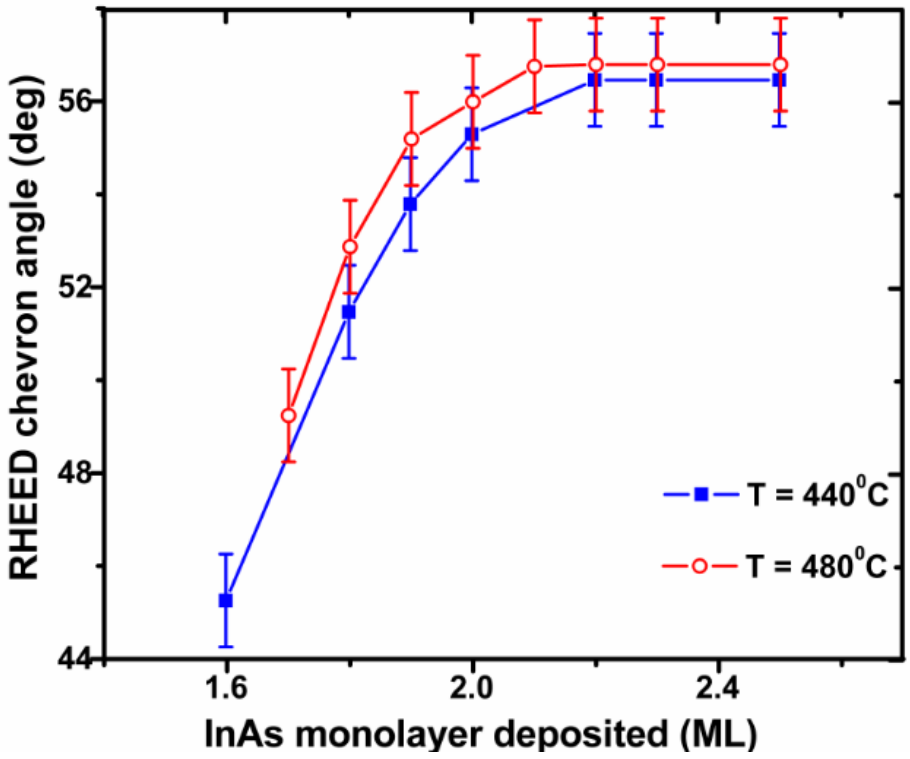

Figure 6.3: RHEED chevron angle evolution of QDs grown at 440^0C and 480^0 as a function of InAs monolayer deposited (RHEED images are taken along [1 $\bar{1}$ 0] azimuth).

At InAs deposition of 1.6ML we have extracted a chevron angle of $45.2^0 \pm 1^0$. Considering the formation of diffraction patterns at different incident azimuths as described in Ichimiya and Cohen (2004), we calculated diffraction images for QDs presented in literature at initial nucleation stages and obtained a chevron angle of 45^0 for both {2 5 11} and {1 3 7} facet orientations and 48^0 for QDs bounded by {1 3 7} and $\{\overline{1}\,3\,\overline{5}\}$ facets along $[1\,\overline{1}\,0]$ azimuth following the dot shape transition presented in Xu *et al*. (2005) (Gunasekera and Freundlich 2015).

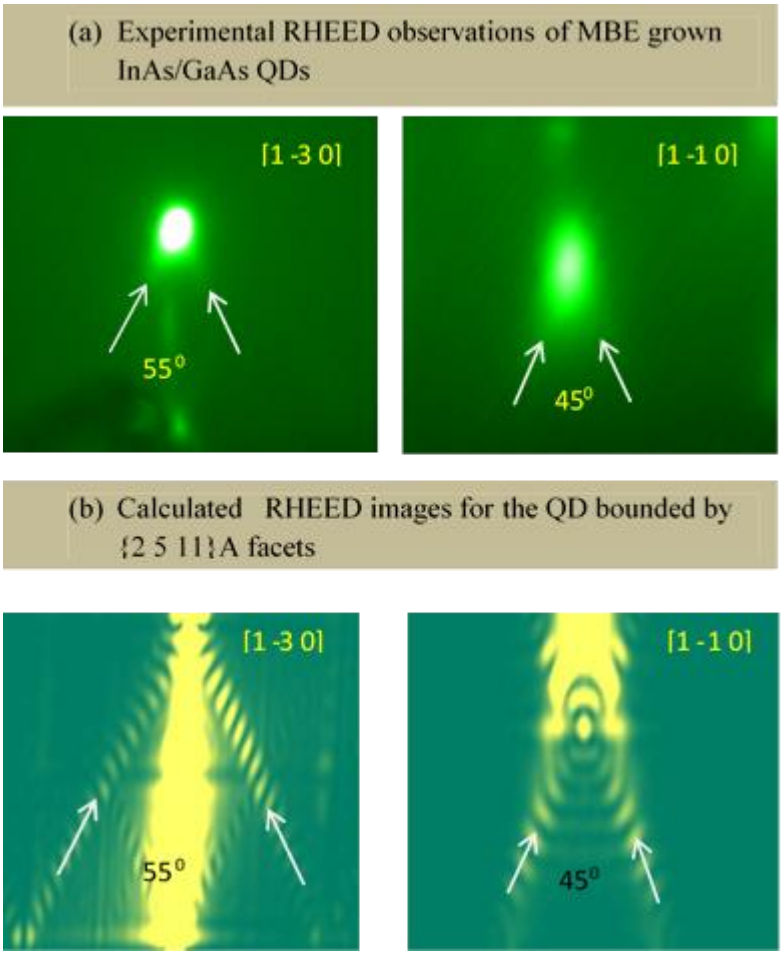

Figure 6.4: (a) Experimental observations of RHEED chevron angles and (b) Calculated RHEED angles along $[1\,\overline{3}\,0]$ and $[1\,\overline{1}\,0]$ crystallographic directions.

In 2001 Márquez *et al*. reported the existence of $(2\ 5\ 11)$ as a new stable facet orientation at the beginning of dot growth under investigation of atomically resolved STM images. Four pronounced facets which are inclined by $24^0 \pm 2^0$ with respect of $[\overline{1\ 1}\ 0]$ principal direction were observed. Atomic features of the facets were discovered to be row of humps aligned along $[1\ 2\ \bar{1}]$ and the Miller indices of the surface were identified to be {2 5 11} (Márquez, Geelhaar and Jacobi 2001). The observations show that the GaAs $(2\ 5\ 11)$ surface consists of a series of three As dimers aligned along $[1\ 2\ \bar{1}]$ which are tilted with respect to the $(2\ 5\ 11)$ surface plane. Adjacent series of three As dimers are slightly shifted towards $[2\ 3\ \bar{1}]$ and give the surface a striped appearance. The orientation of these stripes is $(1\ 3\ 7)$ (Figure 6.5).

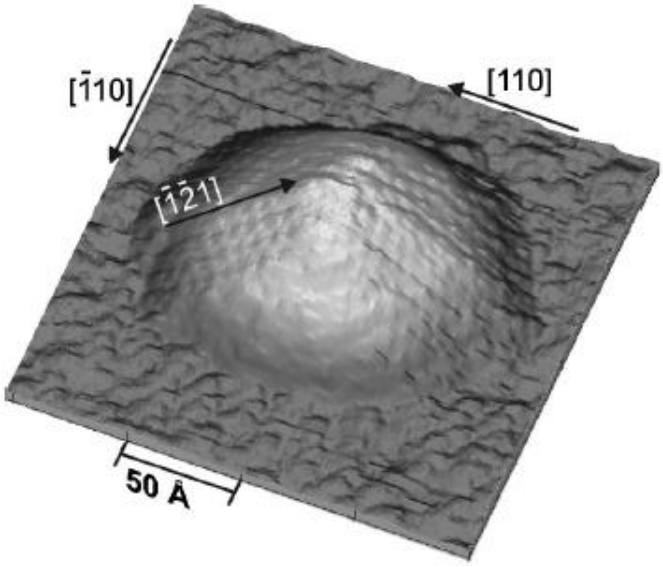

Figure 6.5: 3D STM image of an uncapped InAs QD on GaAs (001). The figure is after Marquez *et al*. Appl. Phys. Lett. (Márquez, Geelhaar and Jacobi 2001)

Studies on (2 5 11) surface indicate that it fulfills the electron counting rules (ECR). The unit mesh on the (2 5 11) surface contains series of three three As dimers, three As atoms with one dangling bond each, and seven Ga atoms with one dangling bond each. The electrons from the Ga dangling bonds can be distributed in such a way that all the Ga dangling bonds are emptied and all the arsenic dangling bonds are completely filled. Thus (2 5 11) facet orientation fulfills the ECR (Jacobi 2003).

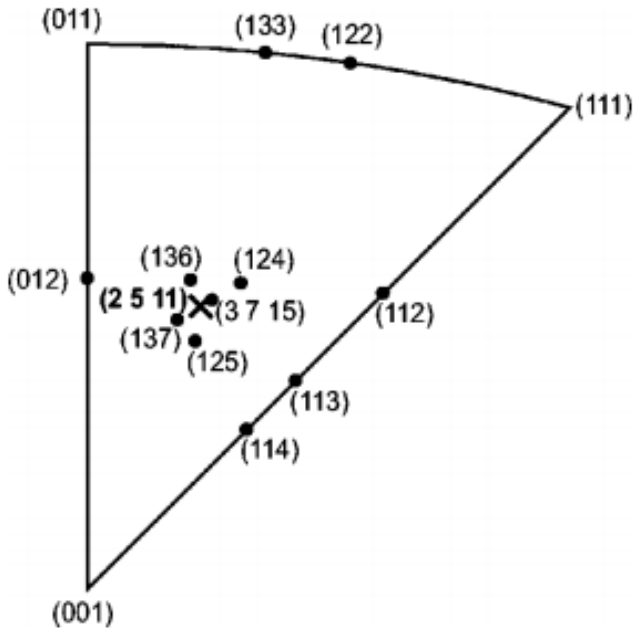

Figure 6.6: Stereographic triangle for fcc III-V compound semiconductor surfaces exhibiting the low index corner points, the [$\bar{1}$ 1 0]-zone borderline connecting the (0 0 1) and (1 1 1) corner points, and the different surface orientations studied experimentally. The figure is after Geelhaar *et al*.,Phys. Rev. B (Geelhaar *et al.* 2002).

Another evidence on existence of stable GaAs (2 5 11) surface is that it is found to be a stable high index surface within the stereographic triangle (Figure 6.6) which is a projection of the orientation vector of the high index GaAs surface studied and of facets, observed on InAs/GaAs (001)(Geelhaar *et al*. 2002) (Jacobi 2003) .

As the growth proceeds, low index facets such as {1 1 0} and $\{\overline{1}\,\overline{1}\,\overline{1}\}$ begin to stack at the sides of the islands preserving QD shape on the top (Kratzer *et al.* 2006) (Xu *et al.* 2005). Only the first few top layers of the quantum dot contribute predominantly in the diffraction pattern, and thus, angle values saturate after a critical dot height. Structures at different growth stages are calculated and calculations for intermediate and fully grown are discussed in Chapter 5. The proposed structures are shown in the figure below.

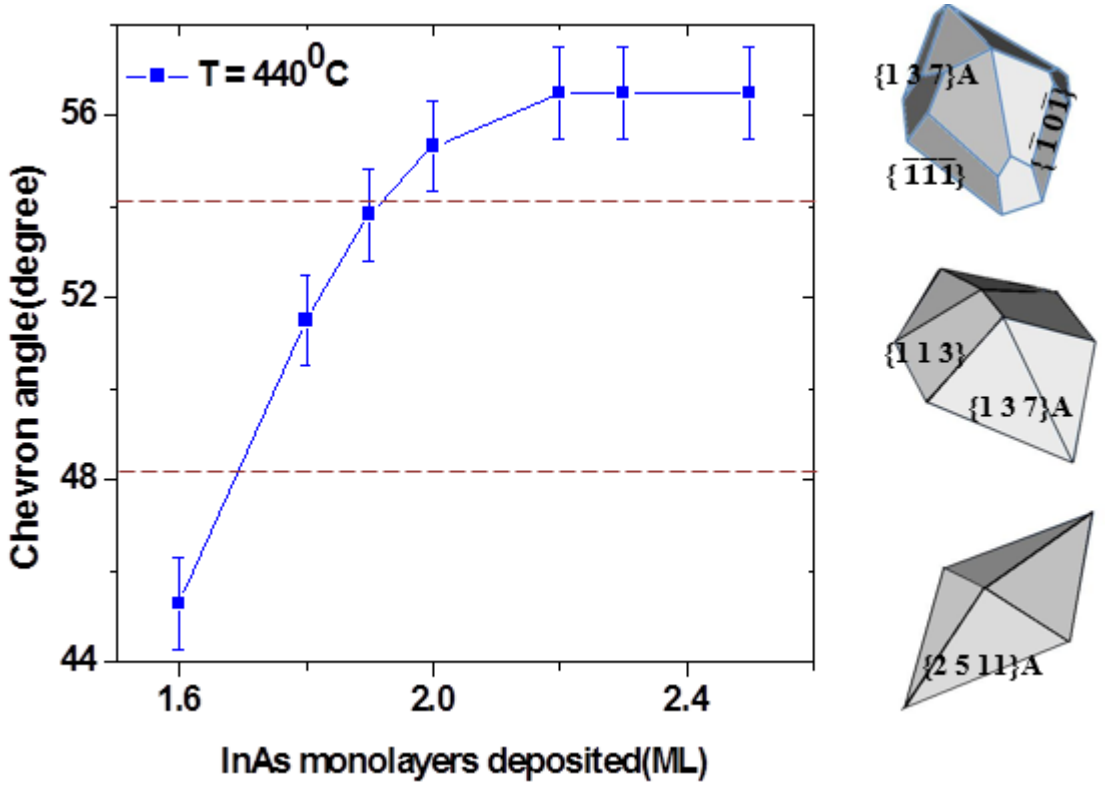

Figure 6.7: Calculated structures for dot shapes at the onset of dot formation, intermediate growth stage and at fully grown quantum dot stage.

Considering the correlation between periodicity of intensity profiles along chevron tails and the dot height, the average dot heights were extracted from intensity profile calculations and the corresponding height evolution is exhibited in Figure 6.8. Average heights of QDs grown at 440^0C and 480^0C continuously increase during growth and the rate at which the dot grows is higher at 480^0C due to increased dot coarsening (Madhukar *et al.* 1994). At 480^0C, the dot started to grow at a lower rate at equivalent 2.3 ML InAs deposition as the dot reaches its critical height limit. In the case at 440^0C this effect is not observable up until equivalent 2.5ML coverage since it is a slow growth process.

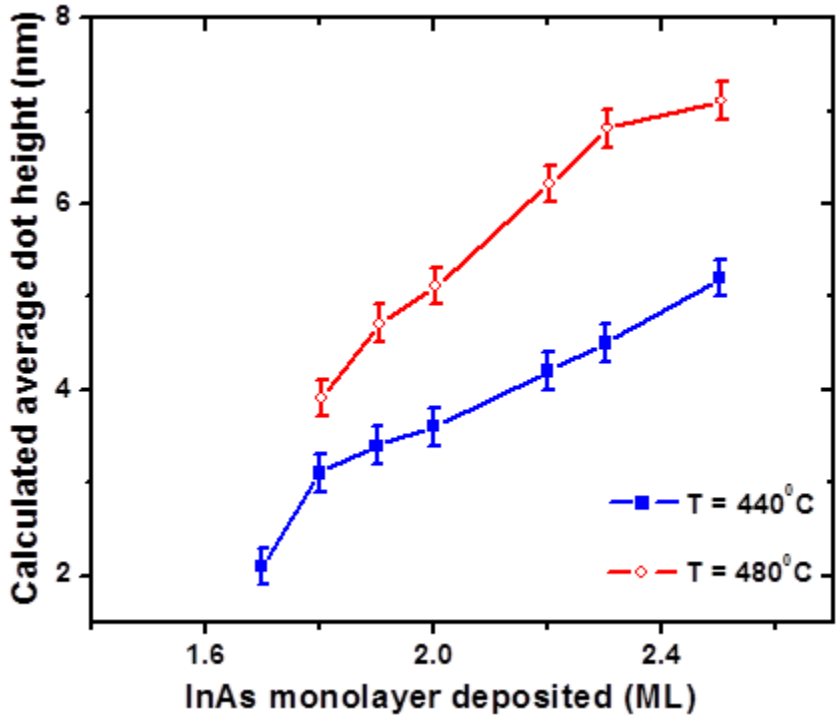

Figure 6.8: Height evolution of QDs grown at temperatures 440^0C and 480^0C. Average sizes are calculated using intensity periodicities.

6.3 Asymmetric dot facet orientation

In this section we discuss an interesting phenomenon we observed during analysis of chevron angles. In Section 6.2 we derived total chevron angle evolution with InAs coverage. A detailed observation of half chevron angles at each growth stage are performed here. Each chevron intensity tail is a contribution of diffraction patterns from surface atoms at a crystallographic plane of the quantum dot side walls. This phenomena is clearly described in Lee *et al*. (2004).

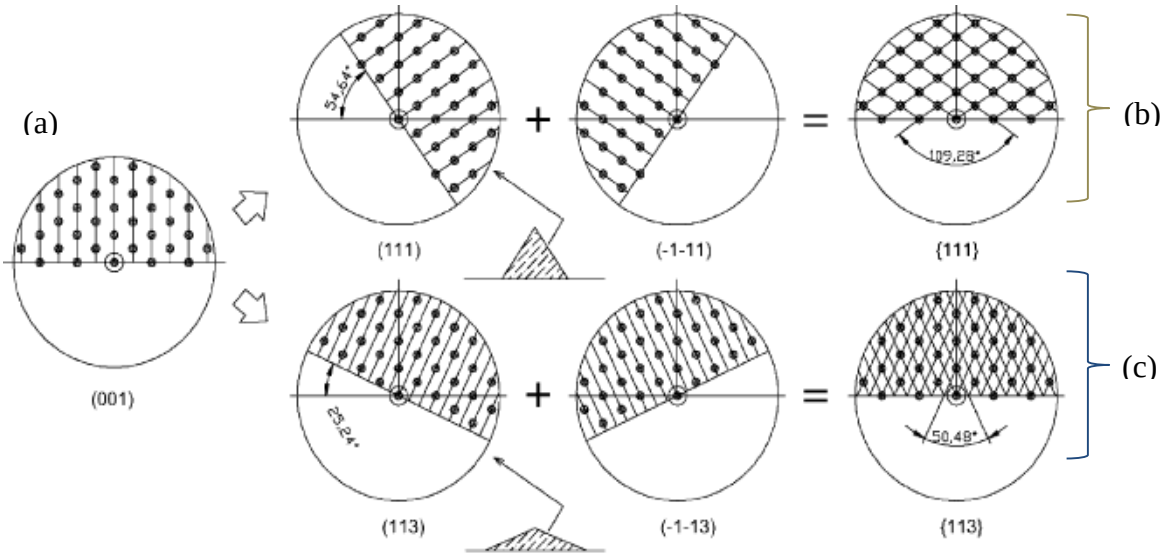

Figure 6.9: (a) (001) RHEED streaks along [1 $\bar{1}$ 0] azimuth and Evolution of RHEED chevron patterns for (b) (1 1 1) facets and (c) (1 1 3) facets. The figure is after Lee *et al*. Appl. Surf. Sci. (Lee *et al.* 2004).

Figures 6.9 (b) and (c) depict the geometry of chevron angles of dots with (1 1 1) and (1 1 3) facets. Intersection of (1 1 3) streak lines from (1 1 3) facet and the ($\bar{1}$ $\bar{1}$ 3) streak lines from ($\bar{1}$ $\bar{1}$ 3) plane originates RHEED chevron pattern with specific angle (Figure 6.10).

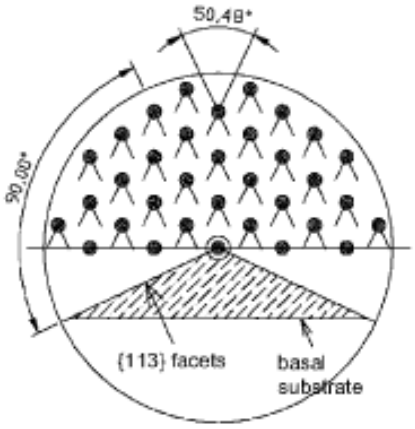

Figure 6.10: Resultant chevron pattern for symmetric (1 1 3) facets.

Thus, half chevron angle evolution was investigated with InAs monolayer coverage. Figure 6.11 is an experimental RHEED chevron pattern along [1 $\bar{1}$ 0] azimuth and the half angles were measured on (0 0 2) diffraction spot. The angular calculations of two growths fabricated at temperatures 440^{0}C and 480^{0}C are plotted in Figure 6.12 as a function of InAs monolayer coverage (Gunasekera and Freundlich 2012).

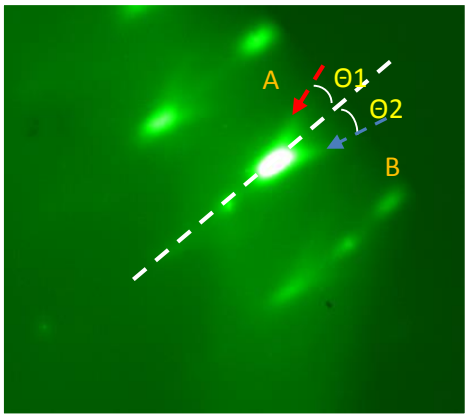

Figure 6.11: Half angles of RHEED chevron pattern. θ1 and θ2 are the angle values to the chevron tails A and B respectively. The white dash line indicates the (0 0 1) streak line.

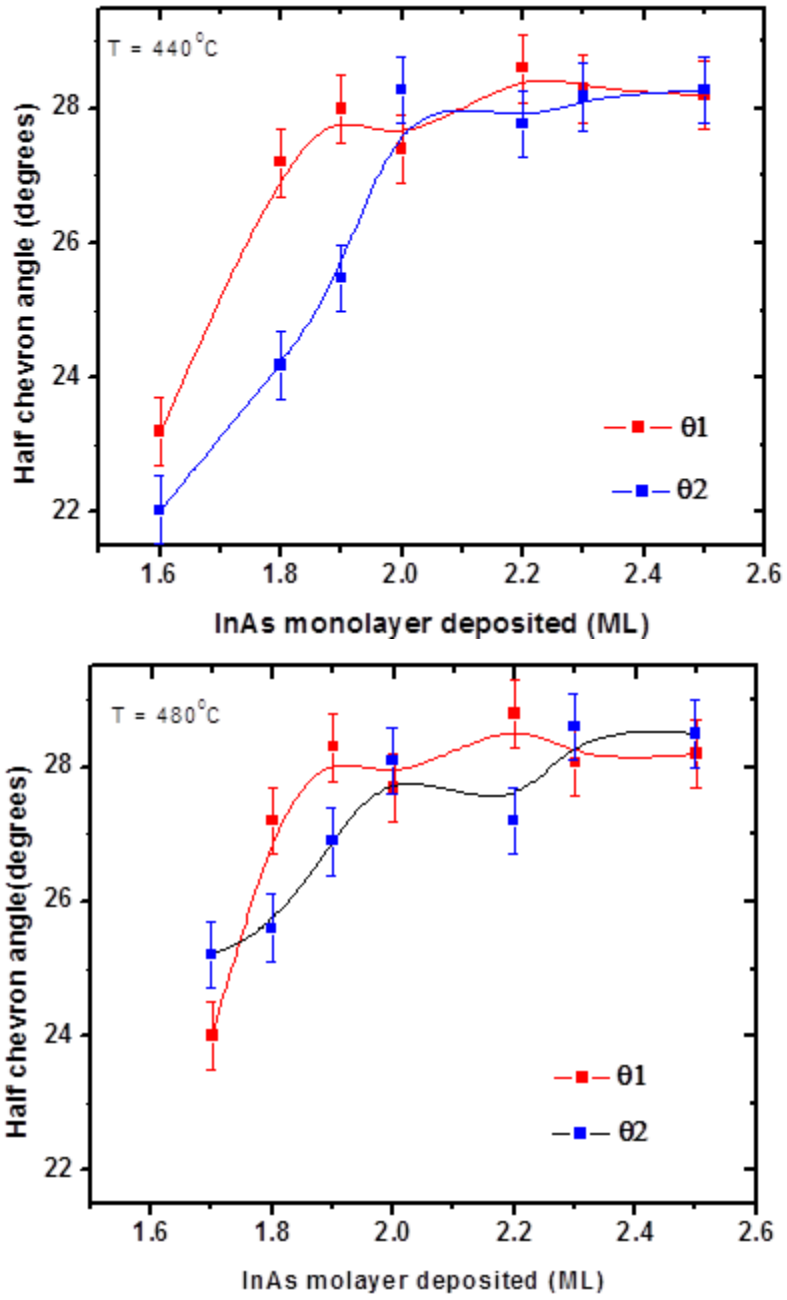

Figure 6.12: Half-chevron angles θ1 and θ2 along two chevron tails A and B respectively at growth temperature (a) 440^0 C and 480^0C.

Predominant inequalities between half chevron angles are observed at the onset of dot nucleation and as the dot evolves the chevron transition becomes more symmetric. Our investigations suggest that this behavior could be a result of formation of islands with asymmetric shapes at the initial growth stages and the dots become more symmetric in shape as they continue to grow. The highly sensitive nature of electron diffraction to morphological changes makes it possible for us to observe irregular asymmetries in RHEED angles as the dot grows due to proceeding stacking of new layers on the existing surfaces.

At equivalent 1.6 InAs monolayer deposition QD chevron angles measure 22^0 and 23.2^0 half chevron angles with $\pm 0.5^0$ error bars as shown in Figure 6.12. As reported in literature, smaller quantum dots are bounded by either {2 5 11} or {1 3 7} facet orientations. For both the facet orientations our theoretical simulation calculates RHEED angle of $22^0 \pm 1^0$ along [1 $\bar{1}$ 0] azimuth which agrees well with literature (Placidi, Pia, and Arciprete 2009), thus, we suggest {2 5 11} and {1 3 7} faceted structures at equivalent 1.6 ML deposition of InAs (Figure 6.12(b) and (c)). The periodicities are not prominent at this stage of RHEED patterns hence the dot height has not been calculated.

A conspicuous asymmetry among the two chevron half angles is observed at 1.9 ML InAs deposition and in Figure 6.12(e), the observed different periodicities ($\omega 1 = 0.034$ mrad, $\omega 2 = 0.027$ mrad) along two chevron tails are implemented.

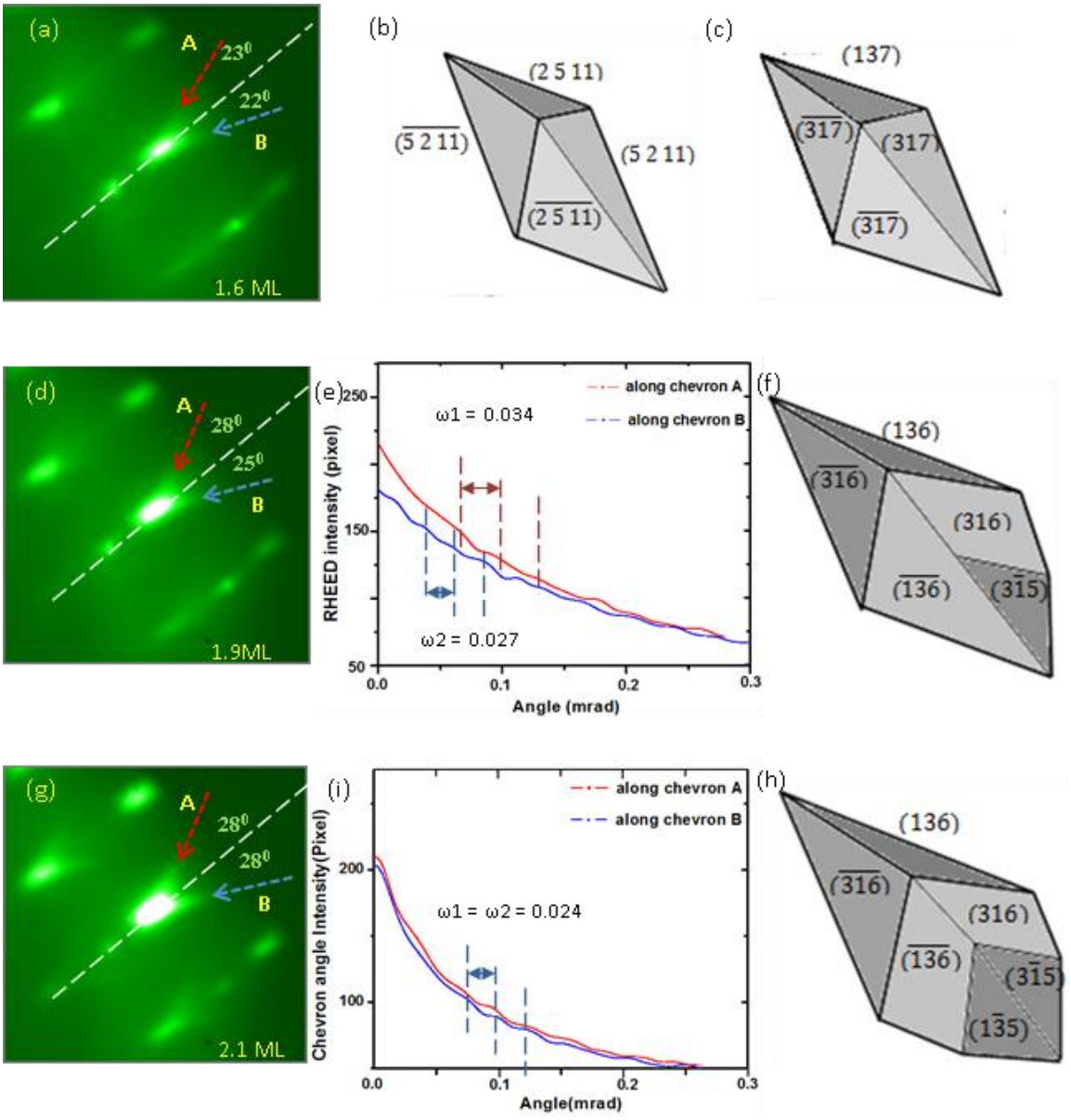

Figure 6.13: (a),(d) and (g) RHEED half chevron angles at 1.6 ML, 1.9ML and 2.1ML InAs deposition along $[1\ \bar{1}\ 0]$ grown at 440^0C respectively; (b) and (c) calculated structures bounded by {2 5 11} and {1 3 7} facets at 1.6 ML deposition; (e) and (h) intensity profiles along chevron tails along A and B of RHEED images in figures (d) and (g); (f) and (i) proposed structures based on theoretical model for (d) and (g) respectively.

The correlation between the half-chevron angle θ, periodicity of chevron intensity profile ω and the dot height *H* is as follows (Feltrin and Freundlich 2007b)

$$H = {}^{P sin\theta}/_{\omega}\,, \tag{6.1}$$

where *P* is a constant and whose value calculated to be 0.71.

The ratio between the two half-chevron angles $28^0$and 25^0 is 1.1 ± 0.2 and this value is compatible with 1.2 ± 0.2, the ratio of the periodicities along corresponding chevron tails (ω1/ω2) agreeing with the correlation stated in Equation 6.1. By analyzing these two parameters we calculated a structure of {1 3 6} and {1 $\bar{3}$ 5} facet combination for QDs at equivalent 1.9ML InAs deposition and is illustrated in Figure 6.32(f).

For {1 3 6} facet orientation we calculated a value of 25^0±1^0 for an incidence along [1 $\bar{1}$ 0] crystal direction using the mathematical model we have developed which agrees well with the value (26^0) reported in literature (Placidi, Pia, and Arciprete 2009). Angle of 28^0 is obtained for {1 3 6}*A* and {1 $\bar{3}$ 5} combined facet orientation and the two half angles are comparable to the experimental angular observations measured in Figure 6.13(i). The periodicity calculations determine the height of the QD to be 3 ±0.3nm.

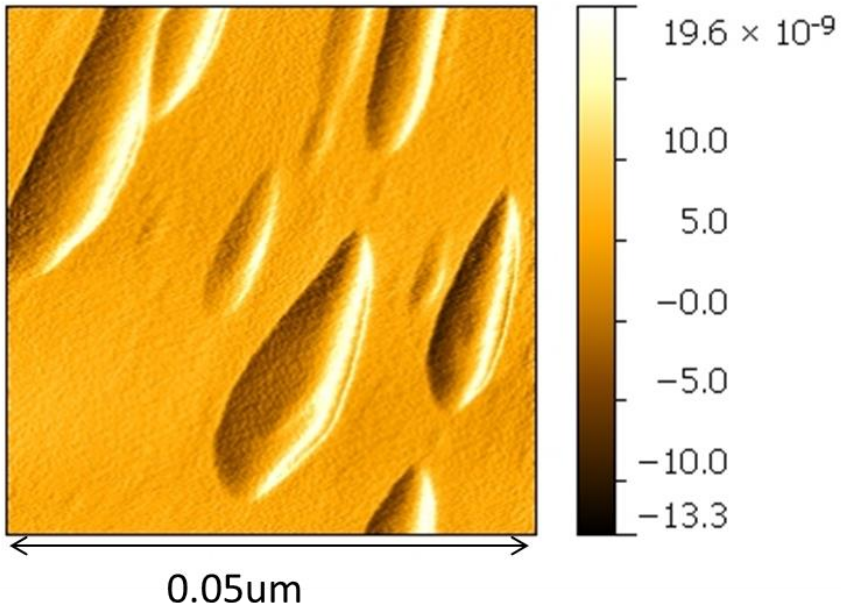

Figure 6.14: Asymmetric dot ripening observed by AFM topography.

The AFM image shown in the above figure exhibit an asymmetric facet orientation along on the sides of $[1\ \bar{1}\ 0]$ direction. The elongation along this azimuth is commonly presence in smaller dot structures and in this case it is more evident due to directional growth along the same axis.

The symmetric periodicity values ($\omega 1 = \omega 2 = 0.024$ mrad) and chevron angles in Figure 6.13(g) and (h) for equivalent InAs deposition of 2.1ML could be a result from symmetric facet orientation on either side of $[1\ \bar{1}\ 0]$ azimuth direction. Calculations derive a combination of {1 3 6}, $(1\ \bar{3}\ 5)$ and $(3\ \bar{1}\ 5)$ facet configuration for the shape of island at this growth stage as shown in Figure 6.13(h).

6.4 Summary

In this chapter we derived QD shape (facet orientation) evolution using RHEED chevron angle, intensity periodicities and the theoretical model described in Chapter 5. A new chevron angle of $45.2^0 \pm 1^0$ at the onset of dot formation was extracted and a facet configuration bounded by the family of $\{2\ 5\ 11\}A$ facets was calculated. Further the behavior of chevron angle variation during growth was discussed and the results were compared with the reports in literature.

As a consequence of this analysis we were able to observe asymmetric half chevron angles at the initial growth stages and RHEED intensity periodicities were compared for further confirmation. At later growth stages the angles become symmetric and dot structures with asymmetric and symmetric facet configurations are proposed.

Chapter 7

Development of Advanced QD Structures

This chapter is intended to provide a different growth technique in fabricating SK QDs separated from its wetting layer to improve photon emission. Modification of structural and optical properties by inserting an intermediate layer (IL) of GaAs or AlAs will be compared with conventional self-assembled QDs using RHEED, AFM, TEM, and PL data. Further the RHEED studies to determine the lower and upper limits of critical thickness for the formation of wetting layer free QDs is presented.

7.1 Interface engineered wetting layer free InAs quantum dots on GaAs(001)

Stranski-Krastanov QDs are shown to be produce ideal single-photon sources, which use the anharmonicity of single quantum dot multiexciton transitions to regulate the photon

generation process (Michler *et al.* 2000) (Santori *et al.* 2001). To design single photon sources in optical applications, fabrication of isolated low density QDs which allow emissions from single dots are therefore a necessary (Alloing *et al.* 2005). The presence of wetting layer in the self-assembly process of nucleation causes uncontrollability over dot distribution and dot density. Further, coalescence of QDs caused from uncontrollable nucleation sites in conventional SK growth mode reduces minority carrier diffusion lengths, which affects short-circuit current density (Bailey *et al.* 2012). Wetting layers also affect electronic properties of quantum dots. The strain in the wetting layer reduces the energy gap between a confined electron and hole level and, hence, affects the confining-potential (Lee S. *et al.* 2004). It is also reported in Lee S. *et. al.* (2004) that in a thin quantum dot, the effect of the wetting layer on the wave function is qualitatively different for the weakly confined electron and the strongly confined hole states. The electron wave function moves from the buffer to the wetting layer, while the hole wave function spreads from the dot to the wetting layer region. The redistribution of the hole wave function causes the increase of the effective lateral confinement range and thus the decrease of the hole level spacing ΔEh.

To overcome these issues with the quantum dots with attached wetting layer it is important to separate the quantum dots from their wetting layer (Kim and Bae 2003). Hence, we added an intermediate layer (GaAs and AlAs, in this work) onto the wetting layer before it reaches its critical thickness of 1.5ML. The strain memory from the wetting layer below transfers into the intermediate layer and nucleates quantum dots on the IL detached from the wetting layer.

Intermediate layer incorporated quantum dots were fabricated using MBE by modifying few growth steps in conventional method described in Section 6.1. After the growth of GaAs buffer layer, a InAs layer equivalent to 1.1 ML is deposited on GaAs buffer layer at 480^0C. Next GaAs/ AlAs intermediate layer of 3ML (or required layer thickness) is added at a growth rate of 0.05ML/s at the same growth temperature of InAs growth. InAs QDs is fabricated then at same growth parameters. Intermediate dot layers are capped by 100nm thick GaAs layer as described in the previous section. The surface QD layer is left uncapped to perform surface analysis. The RHEED data acquisition is carried out during the growth at crystallographic directions $[\overline{1\,1}\,0]$, $[1\,\overline{1}\,0]$ and $[1\,\overline{3}\,0]$. Post growth AFM and TEM investigation are performed.

7.2 Isolated dots and aspect ratio: TEM topography

Aspect ratio of QDs has shown to be influential upon energy levels and strong confinement (Kim and Bae 2003)(Vorobiev, Torchynska and Horley 2013). In fact, a higher aspect ratio is preferable for larger island due to more efficient strain relaxation in the steep part of the island (Kratzer *et al.* 2006).

7.2.1 Conventional InAs QDs on GaAs(001)

The structural parameters of quantum dots were initially investigated by TEM and STEM topographies for conventional and GaAs/AlAs intermediate layer mediated InAs QDs. HR-TEM and HR-XTEM spectroscopies of conventional QDs are exhibited in Figure 6.14. A large variation of unevenly distributed QD sizes is observed in this study.

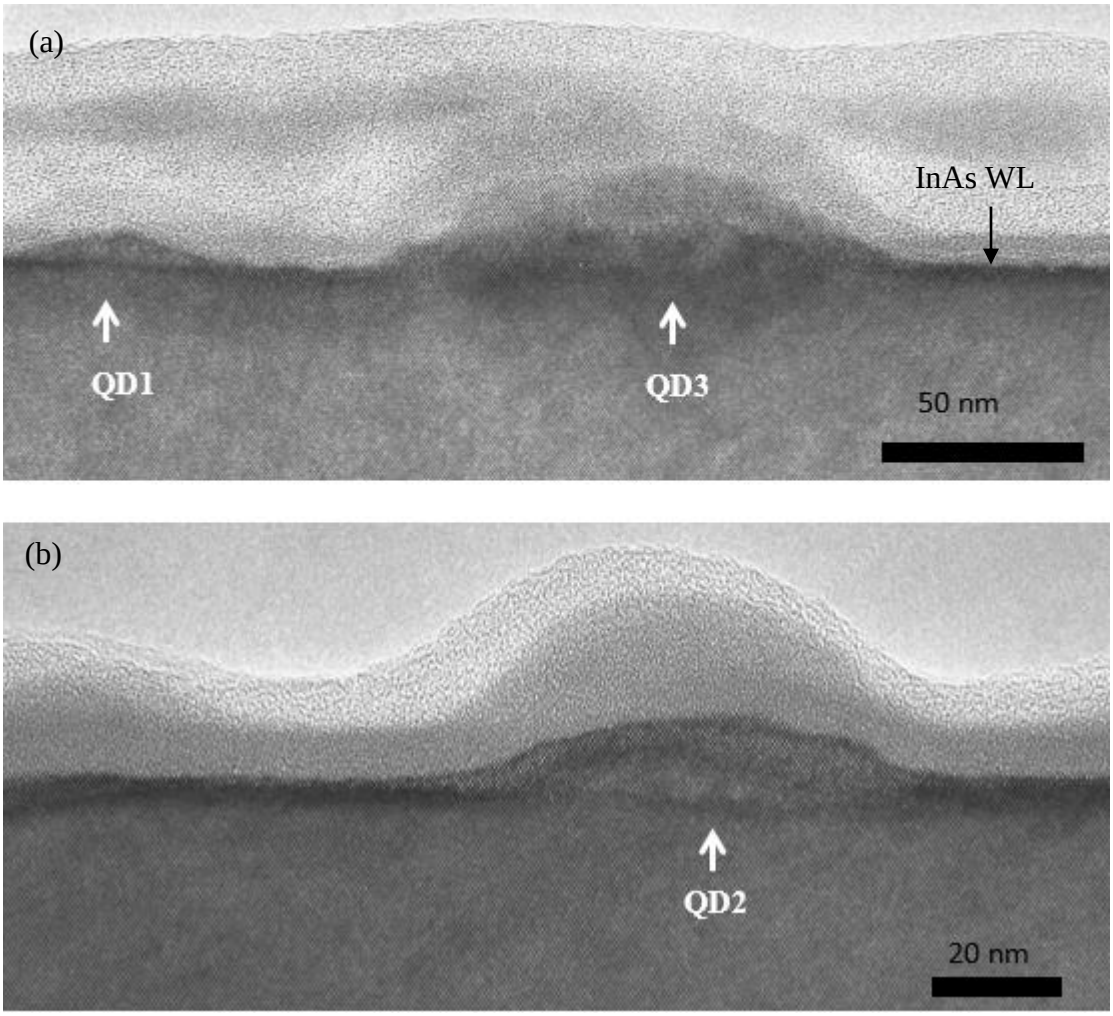

Figure 7.1: Conventional phase-contrast HR-XTEM images of InAs QDs of three sizes on GaAs(001). (a) QD1: smaller QD (≈ 40nm base width) , QD3: larger QD (≈ 120nm) and (b) medium size QD (80nm). An amorphous layer covering the QDs is observed, which was induced intentionally for preserving the QDs (D. Tang & D. A. Smith, University of Arizona).

Smaller QDs of ≈ 40nm base width are present and these QDs are flat in shape with low surface energies. The dots are bounded by the facets of the family {1 3 7} and {1 3 6} with a low aspect ratio (height/base diameter) of 0.2 (Kratzer *et al.* 2006) (Xu *et al.* 2005). HR-TEM image of the enlarged small QD (QD1) exhibited in Figure 7.2(a) shows that the

QD is defect free. With a base diameter of about 80nm, medium size QDs (QD2) are shown to be bounded by new facets at the edges. By comparison with the literature it is clear that these facets are of the family {$\overline{1\ 1\ 1}$}. {1 3 7} facets still dominate the top part of the QD (Kratzer *et al.*2006)(Xu *et al.* 2005). Presence of dislocations are clearly visible in larger QDs (QD3) and it is impossible to identify the facet orientation in these structures.

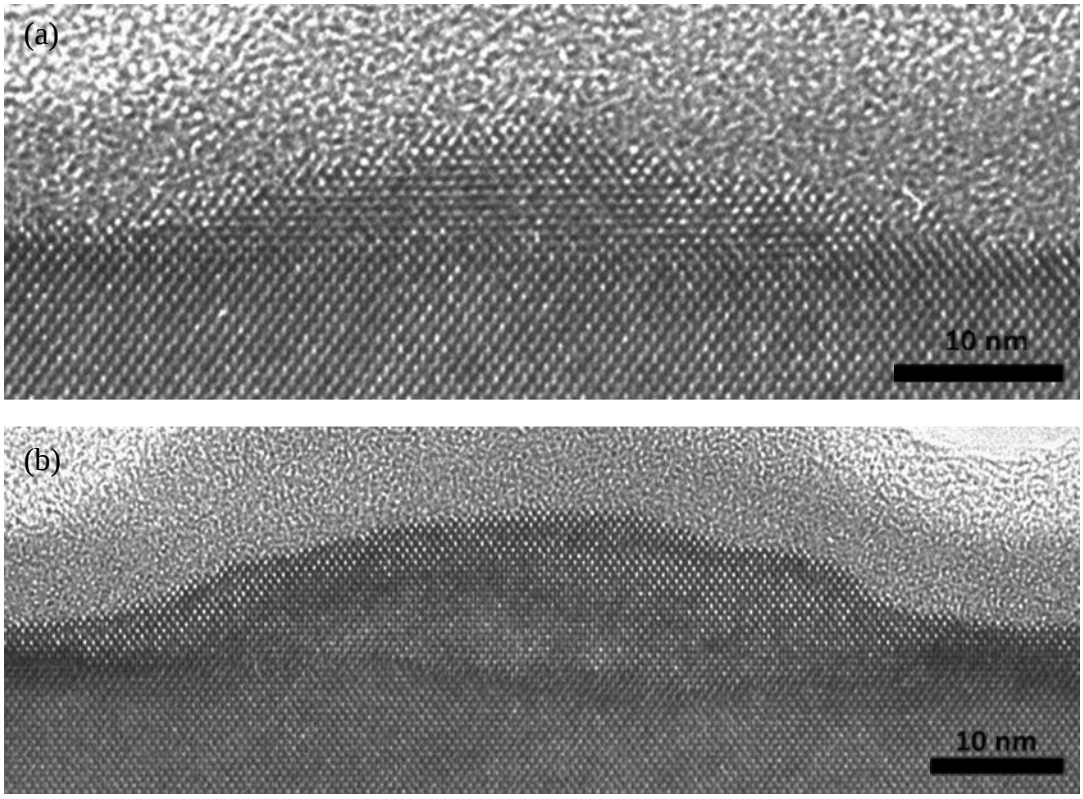

Figure 7.2: Phase-contrast HR-TEM images of (a) QD1 and (b) QD2 shown in Figure 7.1. (D. Tang & D. A. Smith, University of Arizona).

7.2.2 GaAs intermediate layer incorporated QDs

Effect of GaAs intermediate layer of thicknesses of 2 ML and 3 ML was investigated in this section using HAADF-STEM and TEM topographies. Figure 7.3 reveals that incorporation of 2ML GaAs intermediate layer in conventional InAs QD system does not fabricate wetting layer free islands. The thickness of the IL is not sufficient to separate the quantum dot from the wetting layer. Interdiffusion of Ga atoms in the IL and In atoms in the wetting layer creates a InGaAs layer which acts as a wetting layer for InAs molecules deposit in quantum dot growth stage. Reduced lattice mismatch between InGaAs layer and QD lowers WL critical thickness and InGaAs surface states such as InGaAs composition and roughness dramatically affect dot morphology. Flat dots with small heights and large diameters which we observe in the following figure have previously been reported in Seravalli *et al.* (Seravalli, Trevisi and Frigeri 2012) for InAs QDs grown on InGaAs wetting layer.

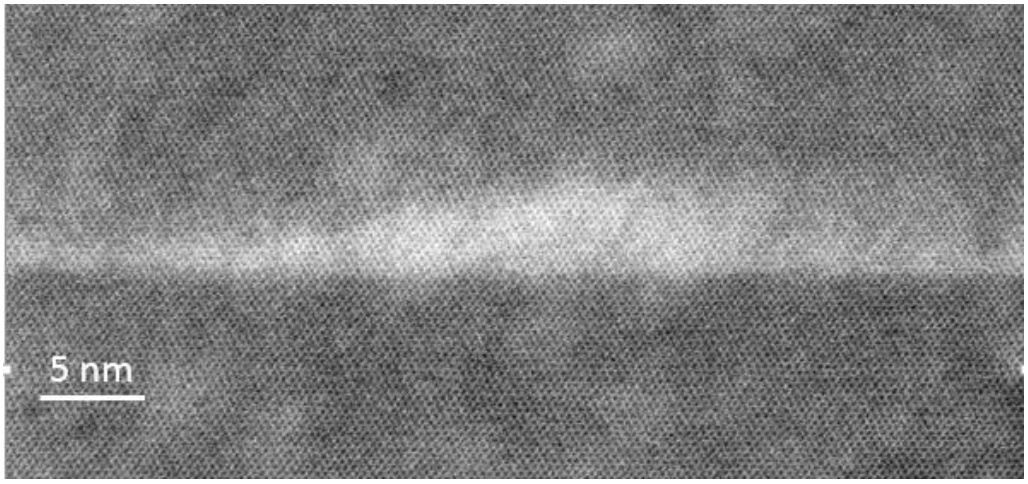

Figure 7.3: HAADF-STEM image of InAs QD with 2ML GaAs IL. No IL was observed due to intermixing of Ga and In adatoms (D. Tang & D. A. Smith, University of Arizona).

As seen in Figure 7.4, three monolayer GaAs space layer insertion, nucleates QDs isolated from the wetting layer and no intermixing between layers is observed(Freundlich *et al.* 2012). Hence, 3ML can be considered as the lower critical limit of GaAs space layer thickness to fabricate wetting layer free QDs. This growth mechanism fabricates dots with higher aspect ratio such that the facet will take the low index form $\{1\ 1\ n\}$ where n = 1, 2. Two size distributions are observed in this study where a smaller QD has a base width of ≈ 6nm and a large QD is with the base width ≈ 13nm.

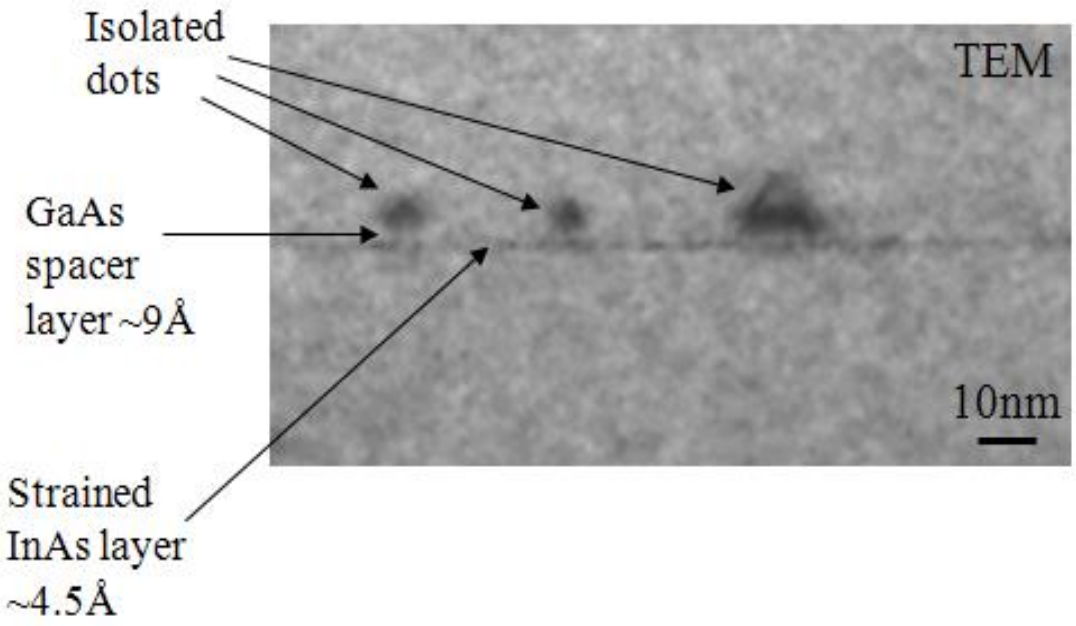

Figure 7.4: TEM topography of 3ML GaAs intermediate layer incorporated InAs quantum dots (collaboration I. Rusakova, University of Houston) (Freundlich *et al.* 2012).

7.2.3 AlAs intermediate layer incorporated QDs

According to Figure 7.5, inter-diffusion between Al and In atoms is observed in 3ML AlAs intermediate layer incorporated InAs QDs (Gunasekera *et al.* 2015). Further QDs seem to be coalesced and hence, a facet configuration cannot be defined. As in Figure 7.6, it has been reported that the In ad-atom mobility and desorption rate on Al containing layers is lower (Ballet *et al.* 2001). Hence, during the capping with GaAs, a higher effective mass flow of indium on the AlAs film takes place resulting a coalesced film of QDs as seen in STEM image.

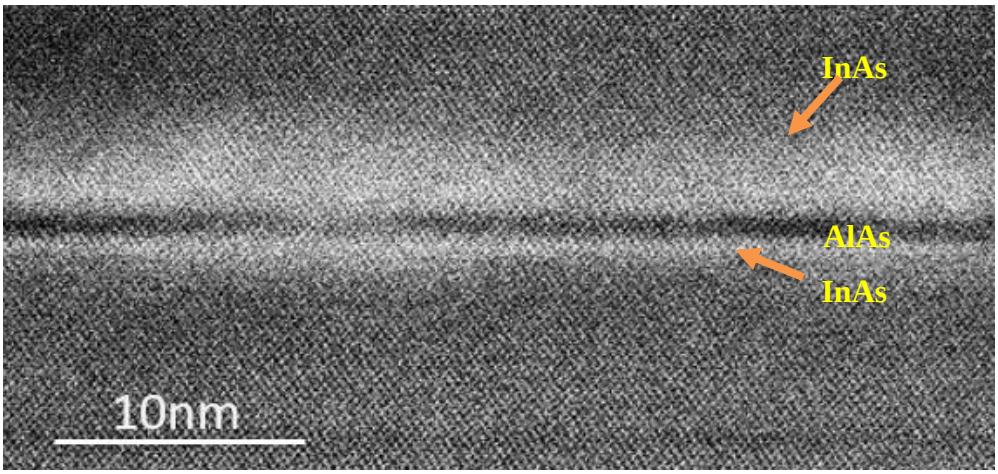

Figure 7.5: HAADF-STEM image of 3 ML AlAs incorporated InAs QDs. (Collaboration D. Tang & D. A. Smith, University of Arizona).

More details on roughness will be discussed in a later section. Further investigations on this growth structure is still in progress.

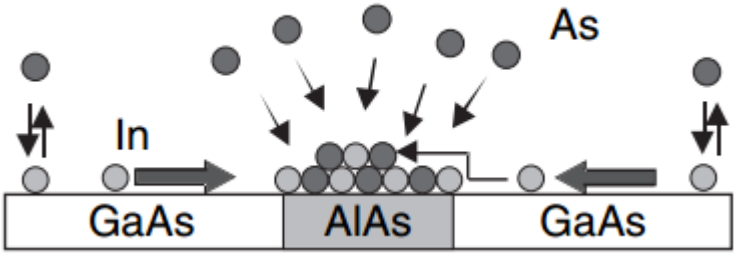

Figure 7.6: Schematics of dynamics of In and As-adatoms on the growing surface showing the preferential nucleation of InAs on AlAs (Uccelli *et al.* 2008).

7.3 Symmetric QD shapes and low density: AFM topographies

The coalesced QDs form dislocations at the QD and substrate interface which reduce optical efficiency and hence, controlling of dot coalescence is extremely important (Forbes *et al.* 2012). Manipulating the wetting layer interface could produce single QDs with low dot densities (Kim and Bae 2003).

7.3.1 Conventional InAs QDs on GaAs(001)

Dot morphology of quantum dots was investigated using AFM imaging (Figure 7.7) on uncapped QD layers. Quantum dots are elongated along [1 $\bar{1}$ 0] azimuth (Xu *et al.* 2005) and a wide distribution of dot sizes is present. Most of these asymmetric dots are closely packed into groups and those small dots coalesce to form large islands. Uncontrollable nucleation sites in self-assembly process causes higher dot density which in this case is 2.3E10 cm^{-2}. Dot heights are distributed in the range of 3-11nm and base width and base length are in the range of 30-40 nm and 50-110 nm respectively resulting islands with poor aspect ratio of ≈ 0.1.

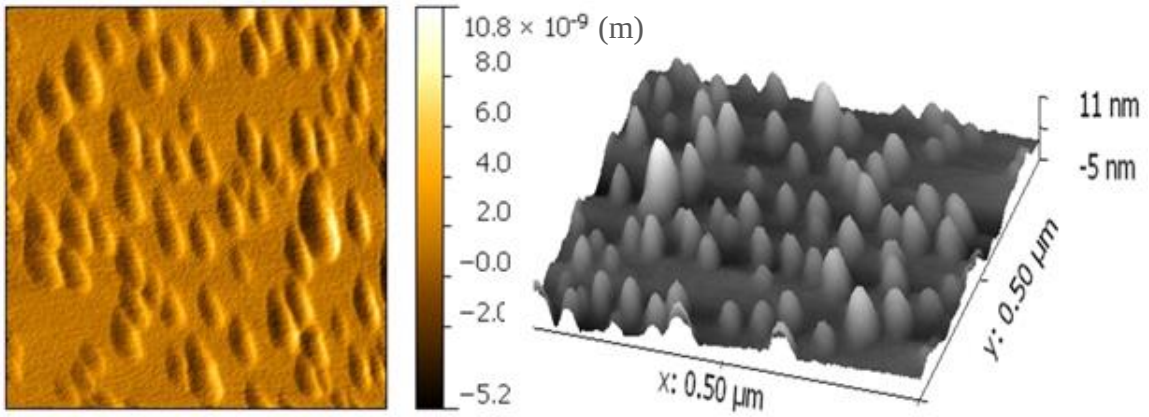

Figure 7.7: AFM image of uncapped InAs SK quantum dots. Scale is 0.5µm.

7.3.2 GaAs intermediate layer incorporated QDs

More symmetric dot shapes are visible in GaAs intermediate layer incorporated InAs quantum and dot density (0.9E10 cm^{-2}) is lesser than that of conventional QDs discussed in the above section. More importantly coalescing of dots is very low.

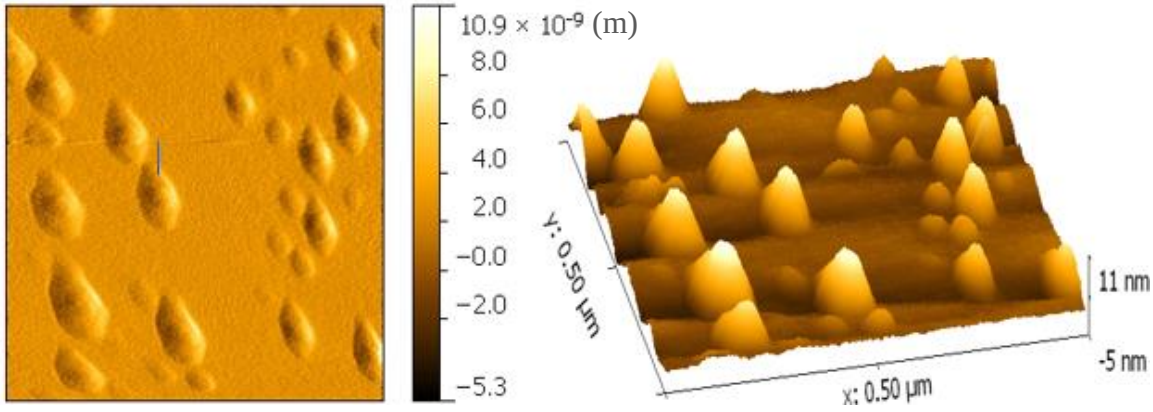

Figure 7.8: AFM image of uncapped 3 ML GaAs intermediate layer inserted InAs SK quantum dots. Scale is 0.5µm.

Three dot size distributions are present. Dimensions of these three categories are tabulated below in Table 7.1.

Table 7.1: Dimensions of 3 ML GaAs intermediate layer inserted QDs measured from AFM topography.

QD type	Height (nm)	Base length(nm)	Base width(nm)
Large	10	100	66
Medium	7	79	46
Small	3	40	27

Faceting is notable in this case compared to conventional islands. The dot shapes discussed in Section 7.2.2 differ from the shapes we observe here due to capping in the previous situation. Strain energy and surface energy are affected by capping and it alters dot shapes drastically (Songmuang, Kiravittaya, and Schmidt 2003).

7.3.3 AlAs intermediate layer incorpotated QDs

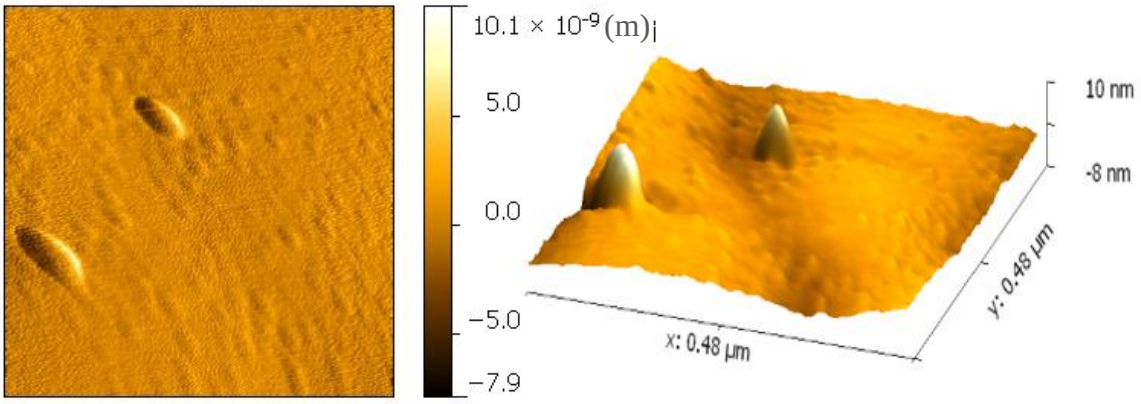

Figure 7.9: AFM image of uncapped 3 ML AlAs intermediate layer inserted InAs SK quantum dots. Scale is 0.5µm.

AFM image of an uncapped 3 ML AlAs intermediate layer incorporated InAs QD is exhibited in Figure 7.9. Two size distributions is present and the density of smaller QDs are much higher compared to the conventional and GaAs intermediate layer incorporated QDs. Dimension of the two are tabulated in Table 7.2.

Table 7.2: Dimensions of AlAs intermediate layer inserted QD features measure from AFM topography.

QD type	Height (nm)	Base length (nm)	Base width (nm)
Large QD	9	75	30
Small QD	2	39	20

The roughness of dots we observed in here could possibly be due to existence of a large number of QDs. Higher roughness and shorter migration length of AlAs surface compared to GaAs surface lead faster nucleation of InAs QDs on AlAs and a few large dots (Park, Tatebayashi and Arakawa 2004)(Hapke-Wurst *et al.* 1999). Reduced adatom mobility results and reduced diffusion length results in formation of a high density of small islands.

7.4 Optical improvement: PL spectroscopy

PL spectroscopy provides electrical characterization. In fact, it provides transition energies which are used to determine electronic energy levels. The intensity of the PL signal is a measure of radiative and nonradiative recombination and quality of surfaces and interfaces (Gfroerer 2000). Insertion of GaAs thin layer on the wetting layer has shown to be effective in controlling optical properties of InAs QDs due to the different growth front (Kim and Bae 2003).

7.4.1 Conventional InAs QDs on GaAs(001)

PL spectra of conventional QDs is shown in Figure 7.10. At 10K, GaAs peaks from excitons bound to neutral acceptors (A^0X) at 1.512 eV and band-acceptor recombination (eC^0) at 1.491 eV were identified (Bogardus and Bebb 1968). 1.479 eV corresponds to e1-lh1(bound electron to light hole) transition energy of 1 ML InAs WL(Hugues *et al.* 2007). Bound e-hh (electron to heavy hole) transition of 1 ML InAs WL is seen at 1.441 eV peak in the PL spectrum (Winzer *et al.* 2002)(Nabetani *et al.* 1994b). Multi size dot distribution is the reason for having a broad QD peak which ranges from 1.083 eV to 1.389 eV with the apex being 1.236 eV (Gunasekera *et al.* 2015).

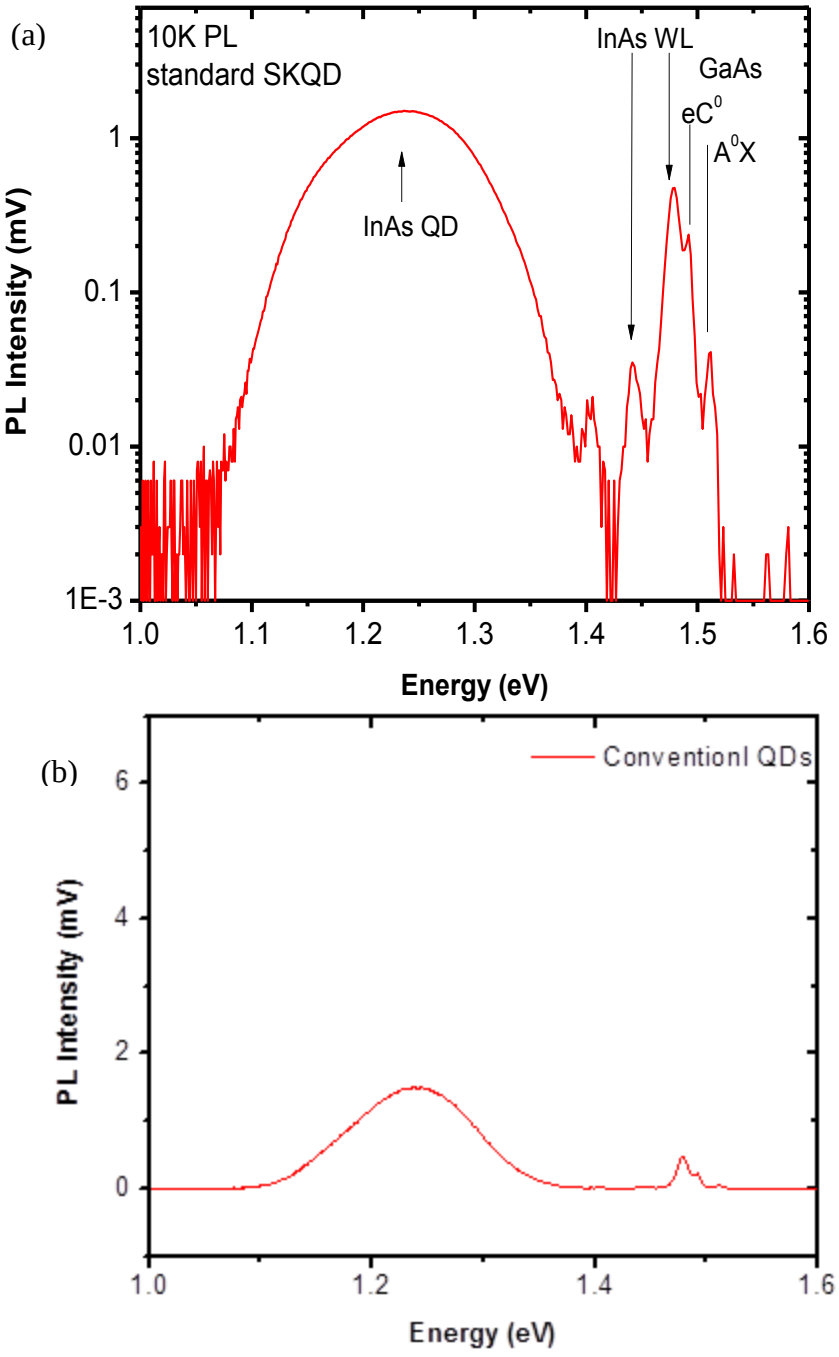

Figure 7.10: PL spectra of conventional SK quantum dots at 10K (a) log scale and (b) linear scale.

7.4.2 GaAs intermediate layer incorporated QDs

Referring to PL spectra of GaAs intermediate layer incorporated QDs (Figure 7.11), we no longer observed the peak for exciton bound to neutral acceptors (A^0X) at 1.5120 eV which we observed in the conventional QD PL spectrum. Instead the peak at 1.5156 eV corresponds to free excitons in GaAs (Uccelli *et al.* 2008) (Pavesi and Guzzi 1994). Similarly the peak at 1.4919 eV (band-acceptor recombination (eC^0)) has shifted to 1.497 eV which corresponds to recombination of band to a neutral acceptor C($e\text{-}A^0$) (Contour *et al.* 1983). This acceptor was found to be from carbon impurities (Rao *et al.* 1985). Wetting layer peaks are not distinguishable in this case.

Interestingly QD PL peaks are in the form of bimodal nature with one peak at 1.146 eV and the other at 1.3175 eV originate from two distinct dot sizes. The small QDs contribute in higher energy peak and the smaller energy peak is due to larger dots (Lee *et al.* 2003). Further the peak corresponds to QD1 cluster shows a blue shift in the spectrum. Similar type of blue shift due to insertion of ~ 2.12ML GaAs IL has been reported by Kim *et al*.((2003). By comparison to the PL spectrum in fig. 7.10 for conventional QDs, the most valuable feature in this PL spectrum is the increased intensity of QD peaks by a factor of two. The peak from QD1 ensemble is stronger and that of QD2 ensemble is relatively weaker as a result of the stronger carrier confinement in smaller QDs (Neogi *et al.* 2005). Rapid carrier relaxation, increased carrier confinement, and increased radiative properties are responsible for overall higher intensities in the PL QD region.

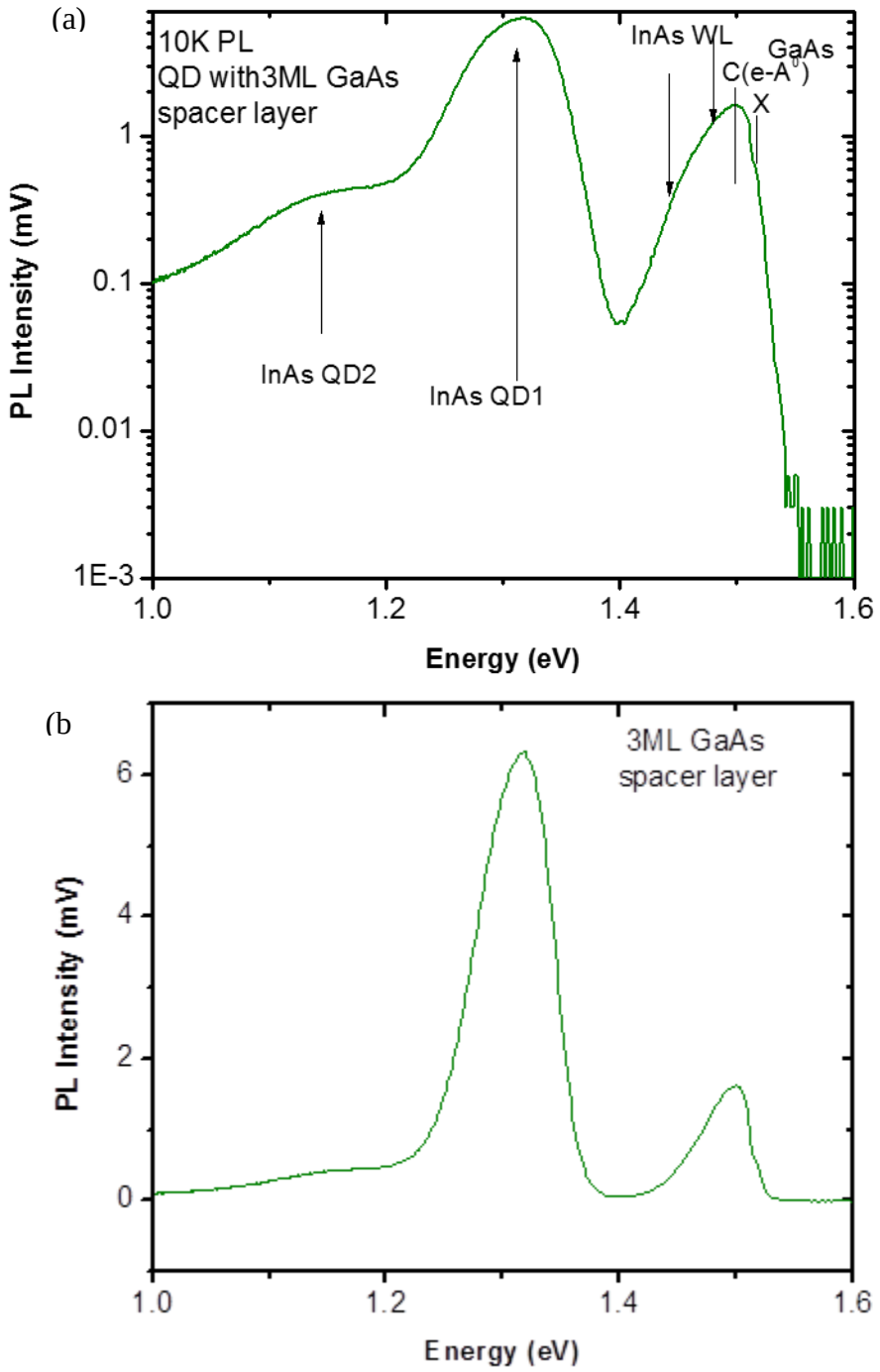

Figure 7.11: PL spectra of 3 ML GaAs intermediate layer incorporated quantum dots at 10K (a) log scale and (b) linear scale.

7.4.3 AlAs intermediate layer incorporated QDs

The PL spectrum of AlAs incorporated InAs QDs at 10K is illustrated in Figure 7.12. Similar to GaAs mediated InAs QD system, the peak at 1.516 eV is from free excitons in GaAs (X). The other GaAs peak at 1.5028 eV is due to donor-acceptor transitions (D-A) (Prutskij, Pelosi and Attolini 2011).

The intensities of GaAs peaks are comparatively similar to PL peaks of both conventional and GaAs IL mediated QD systems. As in the above case with GaAs IL mediated QD system (Figure 7.11), the PL peaks in the QD region has doublet feature suggesting that the QD ensemble has bimodal size distribution. The AFM images shown in Figure 7.9 confirm this bimodal nature as the dots can be categorized into two groups with large and small dots. The peak which is centered at 1.186 eV corresponds to large QDs is blue shifted and the peak at 1.309 eV is red shifted with compared to bimodal peaks in GaAs intermediate layer incorporated QD sample(Figure 7.11). In this case the peak corresponds to larger dots maintains the same intensity as in GaAs SL dot system while the PL peak corresponds to small QDs has shrunk enormously.

The incorporation of AlAs has reduced QD PL intensity substantially than conventional and GaAs intermediate layer incorporated QD systems. While the AlAs matrix layer can help with confinement, aluminum intermixing toward the InAs QDs can cause nonradiative recombination centers in the active region, resulting in degradation of the PL intensity (Park, Tatebayashi, and Arakawa 2004).

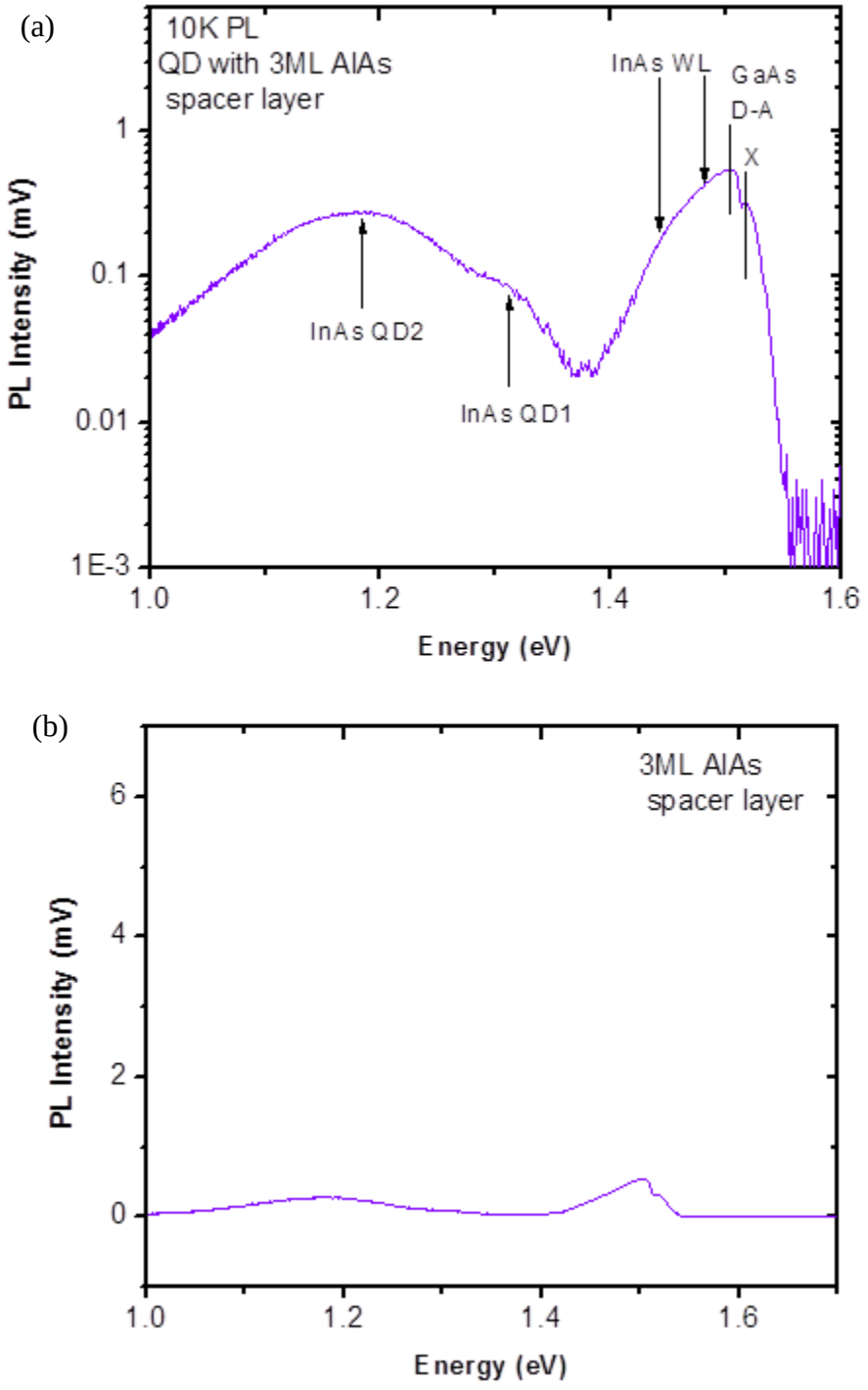

Figure 7.12: PL spectra of 3 ML AlAs intermediate layer incorporated quantum dots at 10K (a) log scale and (b) linear scale.

7.5 RHEED investigation and critical thickness of GaAs intermediate layer for formation of interface modified InAs QDs

RHEED was used as the in-situ characterizing tool for the investigation of InAs dot nucleation with GaAs/AlAs intermediate layer. The following Figure 7.13 shows the intensity variation of the diffraction spot during growth process and corresponding RHEED diffraction patterns recorded.

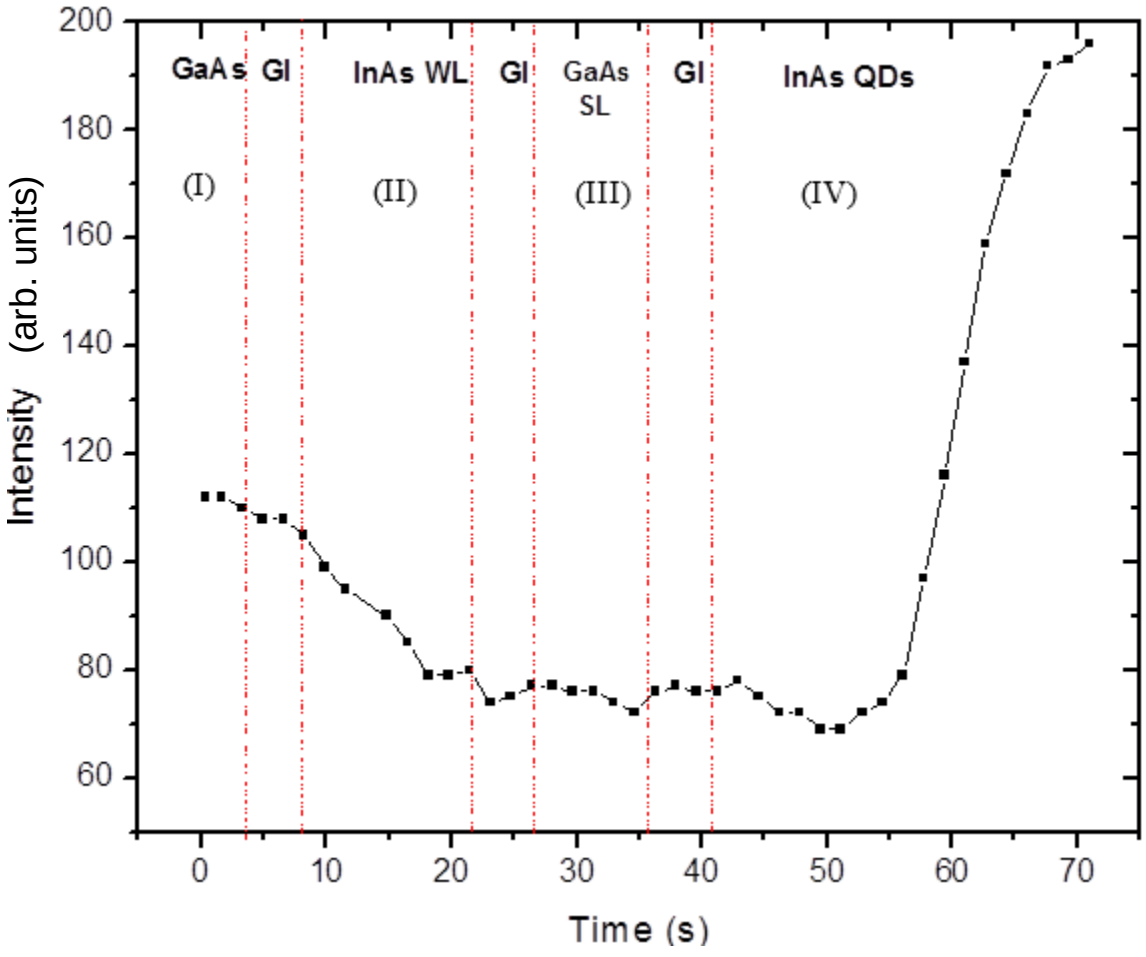

Figure 7.13: RHEED intensity profile of (002) diffraction spot

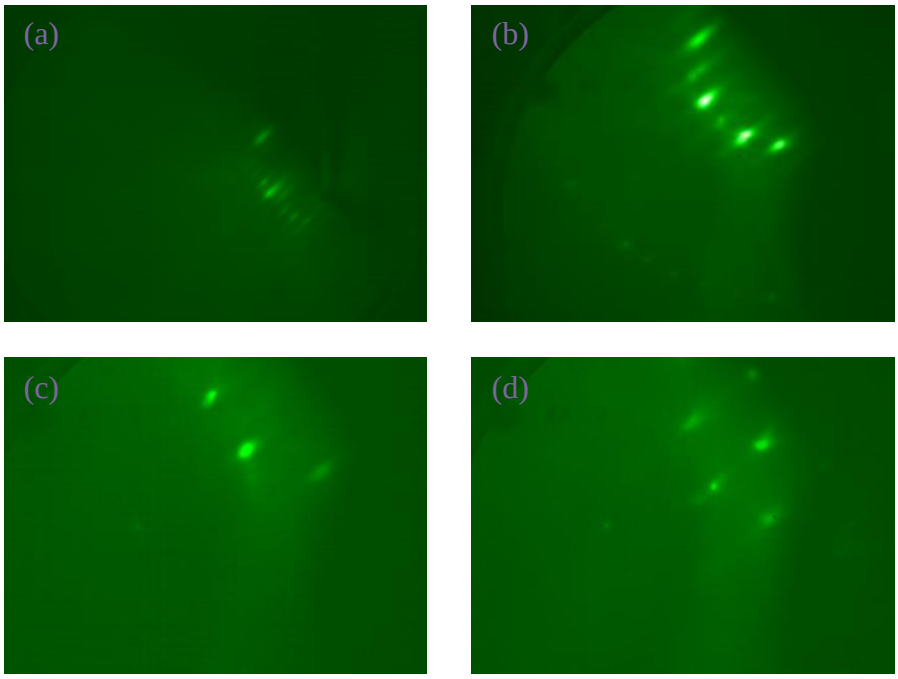

Figure 7.14: RHEED diffraction patterns along [1 $\bar{1}$ 0] direction corresponding to growth stages indicated in fig. 6.25 (a) X4 reconstruction of GaAs, (b) X3 from InAs WL, (c) X4 reconstruction GaAs intermediate layer and (d) chevron formation from InAs QDs.

In section 7.2.1 we found that the GaAs intermediate layer of 2ML is not enough to form isolated QDs but 3ML is the minimum layer thickness for such growth technique. We extended layer thickness up to 20ML to find the maximum limit of critical layer thickness and the analysis was done using RHEED analysis.

For the samples grown with 10 ML and 11 ML GaAs IL thicknesses chevron angles are observable. The reduction of intensity of the pattern is due to increase in surface roughness. At 12 ML insertion, no chevrons can be seen yet the diffraction spot which originates from 3D structures is present. Very flat QDs at the initial growth stages could be a plausible explanation for the existence of the round shape spot without any tails attached (Kudo *et*

al. 2008). From this we can deduce that the strain over 12 ML thickness is not sufficient to create larger QDs with distinguishable facets. Further increase of SL thickness does not form chevrons and remains streaky diffraction pattern as no QDs are nucleating (Figure 7.15(d)).

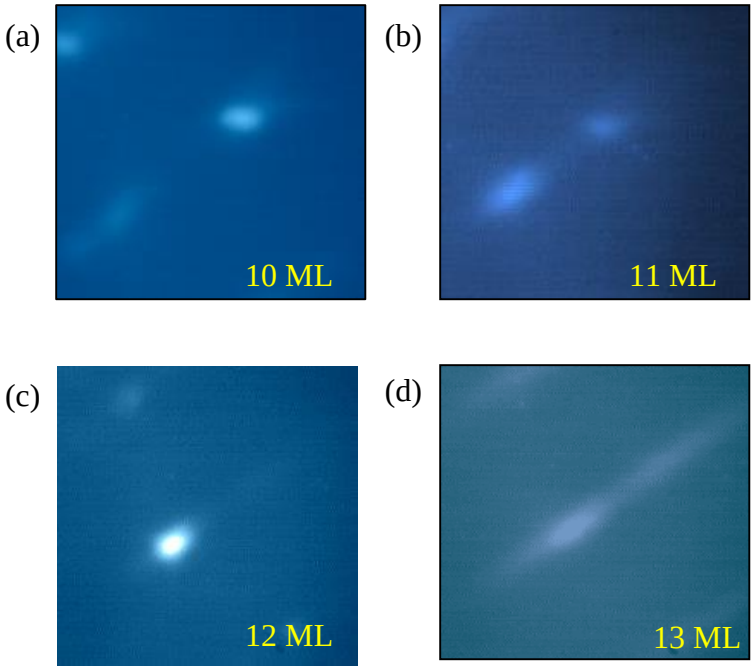

Figure 7.15: RHEED images taken along [1 $\bar{1}$ 0] for GaAs SL thickness (a) 10 ML, (b) 11 ML, (c) 12 ML and (d) 13ML.

From the above observations we can conclude that the critical thickness for nucleation of isolated QDs by insertion of GaAs intermediate layer is 12 ML. Further investigations are being performed using TEM topographies.

7.6 Summary

Here, we presented a separate study performed on strain engineering of the interface InAs wetting layer and InAs QDs by inserting a 3ML GaAs/AlAs intermediate layer. Improvements in dot densities and dot shapes were witnessed with both intermediate layer incorporations. Further PL spectra of both cases indicated bimodal size distribution. Yet only 3ML GaAs intermediate layer incorporated QDs showed an increase in PL intensity and blue shift of the QD peaks with compared to the conventional QDs.

More RHEED investigations on QDs with different thickness of GaAs SL indicate that the minimum critical thickness for the intermediate layer to form QDs is 2 ML and the maximum is limited to 12 ML.

Chapter 8

Summary and Conclusion

Discrete atom-like density of states of semiconductor quantum dots due to three-dimensional confinement is expected to enhance transport and optical properties of photovoltaic devices. Most significantly the tunability of emission spectrum over quantum dot size has attracted much attention in optoelectronic applications. To have a precise control over size, a sufficient understanding of dot nucleation and growth kinetics are required along with a thorough investigation of the effects of growth conditions such as growth temperature, material deposition rate and III/V ratio on dot structural properties. Subsequently QD size, density, and dot shape in terms facet orientation have been investigated intensively in literature using scanning tunneling microscope (STM) analysis.

The growth of Stranski-Krastanov InAs dots on GaAs had been shown to lead to the formation of quantum dots which are believed to be bounded by {1 3 7} facets at initial stages of dot nucleation. Previously the ability of Reflection High-energy electron diffraction (RHEED) *in-situ* technique for real time determination of average dot density and size as well as an ambiguous determination of dot facet orientations have been established.

Refining the home-made theoretical model for calculating QD atomic structure and RHEED images were first done by inclusion of scattering vector dependence scattering factor (*f(s)*). The initial model used constant values for *f(s)*. The refined calculations

produce noise less, better comparable intensity profiles along chevron tails compared to experimental observations and the results are given in Chapter 5. Further in this chapter the calculation of strain on a atomic plane is presented for a detailed understanding of the effect of relaxation of atoms in atomistic model.

The evolution of QD shape and size at the onset of dot formation is one of the main investigation carried out. Associating RHEED patterns along principal azimuths [1 1 0], [1 -1 0] and [1 -3 0] to experimental chevron patterns at very initial growth stages yielded the existence of very small QDs with {2 5 11} facets with RHEED chevron angle of 45.2^0 which we report for the first time in literature.

By performing a more careful study on half chevron angles, we were able to report first evidence on the existence of dot facet asymmetries at early growth stages. Using the periodicity of oscillations of the intensity profiles and half chevron angles we propose dot structures at different growth stages. More studies on understanding the driving forces for the formation of asymmetric dot shapes in required.

Further in the final section, a new development of advance QD structure is stated. Incorporating an intermediate layer between the wetting layer(before critical thickness) and QD layer modifies the strain at the interface creating isolated wetting layer free QDs. Less density with symmetric dot shapes were obtained in the incorporation of 3ML GaAs intermediate layer. The observed improvements in PL intensities and the bimodal nature in the QD regions were a promising aspect in device fabrication.

Bibliography

Alloing, B., Zinoni, C., Zwiller, V., Li, L.H., Monat, C., Gobet, M., Buchs, G., Fiore, A. and E. and Kapon, E.P., (2005). Growth and characterization of single quantum dots emitting at 1300 nm. *Appl. Phys. Lett.*, 86(10), pp.1–3.

Arakawa, Y. and Sakai, H., (1982). Multidimensional quantum well laser and temperature dependence of its threshold current. *Appl. Phys. Lett.*, 40(11), p.939.

Arciprete, F., Fanfoni, M., Patella, F., Della Pia, a. and Balzarotti, a., (2010). Temperature dependence of the size distribution function of InAs quantum dots on GaAs(001). *Phys. Rev. B*, 81(16), pp.1–5.

Arciprete, F., Placidi, E., Sessi, V., Fanfoni, M., Patella, F. and Balzarotti, a., (2006). How kinetics drives the two- to three-dimensional transition in semiconductor strained heterostructures: The case of InAs/GaAs(001). *Appl. Phys. Lett.*, 89(4), pp.87–90.

Arthur, J.R., (1968). Interaction of Ga and As2 molecular beams with GaAs surfaces. *J. Appl. Phys.*, 39(8), p.4032.

Arthur, J.R., (1974). Surface stoichimetry and structure of GaAs. *Surf. Sci.*, 43, pp.449–461.

Bailey, C.G., Forbes, D. V., Polly, S.J., Bittner, Z.S., Dai, Y., C., M., Raffaelle, R.P. and M., H.S., (2012). Open-circuit voltage improvement of InAs/GaAs quantum dot solar cells using reduced InAs coverage. In *IEEE PVSC*. pp. 269–275.

Ballet, P., Smathers, J.B., Yang, H., Workman, C.L. and Salamo, G.J., (2001). Control of size and density of InAs/(Al, Ga)As self-organized islands. *J. Appl. Phys.*, 90(1), pp.481–487.

Bauer, E., (1958). Phänomenologische Theorie der Kristallabscheidung an Oberflächen. II. *Zeitschrift für Kristallographie*, 110(1-6), pp.395–431.

Bauer, E., Bonczek, F., Poppa, H. and Todd, G., (1975). Thermal desorption of metals from tungsten single crystal surfaces. *Surf. Sci.*, 53, pp.87–109.

Biegelsen, D.K., Bringans, R.D., Northrup, J.E. and Swartz, L.-E., (1990). Surface reconstructions. *Phys. Rev. B*, 41(9).

Bimberg, D., Grundmann, M. and and Ledentsov, N.N., (2001). *Quantum Dot Heterostructures*, Germany: John Wiley & Sons.

Bogardus, E.H. and Bebb, H.B., (1968). Bound-exciton, free-exciton, band-acceptor, donor-acceptor, and auger recombination in GaAs. *Phy. Rev.*, 176(3), pp.993–1002.

Bute, O., Cimpoca, G.H. V, Placidi, E., Arciprete, F., Patella, F., Fanfoni, M. and Balzarotti, A., (2008). The monitoring of 2d-3d transition for InAs / GaAs (001) self-assembled quantum dots by atomic force microscopy. *J. Optoelectronics and Adv. Mat*, 10(1), pp.74–79.

Cho, A.Y., (1970). Morphology of epitaxial growth of GaAs by a molecular beam method: The observation of surface structures. *J. Appl. Phys.*, 41(7), p.2780.

Cho, A.Y. and Arthur, J.R., (1975). Molecular beam epitaxy. *Prog. in Solid State Chemistry*, 10, pp.157–191.

Contour, J.P., Neu, G., Leroux, M., Chaix, C., Levesque, B. and Etienne, P., (1983). An optical characterization of defect levels induced by MBE growth of GaAs. *J. Vacuum Sci. & Tech. B: Microelectronics and Nanometer Structures*, 1(3), p.811.

Davisson, C. and Germer, L.H., (1927). The Scattering of electrons by a single crystal of nickel. *Nature*, 119(2998), pp.558–560.

Daweritz, L. and Ploog, K., (1994). Contribution of reflection high-energy electron diffraction to nanometre tailoring of surfaces and interfaces by molecular beam epitaxy. *Semiconductor Sci. and Tech.*, 9(2), pp.123–136.

Dobbs, H.T., Vvedensky, D.D., Zangwill, A., Johansson, J., Carlsson, N. and Seifer, W., (1997). Mean-field theory of quantum dot formation. *Phys. Rev. Lett.*, 79(5), pp.897–900.

Doyle, P. a. and Turner, P.S., (1968). Relativistic Hartree–Fock X-ray and electron scattering factors. *Acta Crystallographica Section A*, 24(3), pp.390–397.

Ekimov, A.I., Efros, A.L. and Onushchenko, A.A., (1985). Quantum size effect in semiconductor microcrystals. *Solid State Communications*, 56(11), pp.921–924.

Enrlich, G., (1956). The mechanism of chemisorption on metals. *J. Phys. Chem. Solids*, 1, pp.1–13.

Farrell, H.H., (1990). Reflection high-energy electron diffraction characteristic absences in GaAs(100) (2×4)–As: A tool for determining the surface stoichiometry. *Journal of Vacuum Science & Technology B: Microelectronics and Nanometer Structures*, 8(4), p.903.

Feltrin, A. and Freundlich, A., (2007)(a). Effect of strain anisotropies on RHEED patterns of quantum dots. *J. Crys. Growth*, 301-302, pp.793–796.

Feltrin, A. and Freundlich, A., (2007)(b). RHEED metrology of Stranski–Krastanov quantum dots. *J. Crys. Growth*, 301-302, pp.38–41.

Forbes, D. V., Bailey, C.G., Polly, S., Bittner, Z.S., Kerestes, C., Slocum, M. and Hubbard, S.M., (2012). Correlation between quantum dot morphology and photovoltaic performance. *Conference Record of the IEEE Photovoltaic Specialists Conference*, pp.1798–1802.

Foxon, C.T., (1983). MBE growth of GaAs and III-V alloys. *J. Vacuum Sci. & Tech. B: Microelectronics and Nanometer Structures*, 1(2), p.293.

Franchi, S., (2013). From research to mass production. In M. Henini, ed. *Molecular Beam Epitaxy*. Amsterdam: Elsevier.

Frank, F.C. and van der Merwe, J.H., (1949). One-dimensional dislocations. I. Static theory. *Proceedings of the Royal Society of London*, 198(1053), pp.205–216.

Freundlich, A., Gunasekera, M., Rajapaksha, C. and Rusakova, I., (2012). Epitaxy of high aspect ratio and wetting-layer-free InAs quantum dots on (Al)GaAs. *Conference Record of the IEEE Photovoltaic Specialists Conference*, pp.1895–1897.

Freundlich, A., Rajapaksha, C. and Gunasekera, M., (2011). During-growth quantitative metrology of epitaxial quantum dots by reflection high-energy electron diffraction. *Conference Record of the IEEE Photovoltaic Specialists Conference*, pp.003483–003485.

Frood, J.S., Davies, G.J. and Tsang W. T., (1997). *Chemical Beam Epitaxy and Related Techniques*, West Sussex: John Wiley and Sons.

Garreau, Y., Sauvage-Simkin, M., Jedrecy, N., Pinchaux, R. and Veron, M., (1996). Atomic structure and faulted boundaries in the GaAs(001) β(2×4) surface as derived from x-ray diffraction and line-shape analysis. *Phys. Rev. B*, 54(24), pp.17638–17646.

Geelhaar, L., Temko, Y., Márquez, J., Kratzer, P. and Jacobi, K., (2002). Surface structure of GaAs(2 5 11). *Phys. Rev. B*, 65(15), pp.1–13.

Gfroerer, T.H., (2000). Photoluminescence in analysis of surfaces and interfaces. *Encyclopedia of Analytical Chemistry*, pp.9209–9231.

Goldstein, L., Glas, F., Marzin, J.Y., Charasse, M.N. and Le Roux, G., (1985). Growth by molecular beam epitaxy and characterization of InAs/GaAs strained-layer superlattices. *Appl. Phys. Lett.*, 47(10), pp.1099–1101.

Gunasekera, M. and Freundlich, A., (2012). Real time during growth metrology and assessment of kinetics of epitaxial quantum dots by RHEED. In *IEEE PVSC*,pp. 1794-1797.

Gunasekera, M. and Freundlich, A., (2013). Unveiling structural properties of self-assembled quantum dots. In *SPIE Proc*. 8634, pp. 86340R-1

Gunasekera, M., Freundlich, A., Smith, D.A. and Rusakova, I., (2015). Fabrication and characterization of interface engineered wetting layer free InAs QDs on GaAs(001). In *IEEE PVSC*. In press.

Gunasekera, M. V and Freundlich, A., (2015). Real-time growth assessments of size orientation and facet asymmetries of self-assembled quantum dots. In *IEEE PVSC*. In press.

Hanada, T., Koo, B.-H., Totsuka, H. and Yao, T., (2001). Anisotropic shape of self-assembled InAs quantum dots: Refraction effect on spot shape of reflection high-energy electron diffraction. *Phys. Rev. B*, 64(16), pp.1–6.

Hanada, T., Totsuka, H. and and Yao, T., (2001). Strain relaxation of self-assembled InAs /GaAs (001) quantum dots observed by reflection high-energy electron diffraction. *Jpn. J. Appl. Phys.*, 40(3), pp.1878–1881.

Hapke-Wurst, I., Zeitler, U., Schumacher, H.W., Haug, R.J., Pierz, K. and Ahlers, F.J., (1999). Size determination of InAs quantum dots using magneto-tunnelling experiments. *Semiconductor Science and Technology*, 14(11), pp.L41–L43.

Harris, J.J., Joyce, B.A. and Dobson, P.J., (1981). Oscillations in the surface structure of Sn-doped GaAs during growth by MBE. *Surf. Sci. Lett.*, 103(1), pp.L90–L96.

Heyn, C., Self-assmbly of quantum dots and rings on semiconductor surfaces. (2010).. In D. Heitmann, ed. *Quantum Materials*. Germany: Springer, p. 6.

Heyn, C., Stemmann, a., Schramm, a., Welsch, H., Hansen, W. and Nemcsics, Á., (2007). Regimes of GaAs quantum dot self-assembly by droplet epitaxy. *Physical Review B - Condensed Matter and Materials Phys.*, 76(7), pp.1–3.

Honma, T., Tsukamoto, S. and Arakawa, Y., (2006). Scanning tunneling microscope observation of InAs wetting layer formation on GaAs(001) during molecular beam epitaxy growth at 500 °C . *Jpn J. Appl. Phys.*, 45(No. 30), pp.L777–L779.

Huffaker, D.L., Park, G., Zou, Z., Shchekin, O.B. and Deppe, D.G., (1998). 1.3 um room-temperature GaAs-based quantum-dot laser. *Appl. Phys. Lett.*, 73(18), pp.2564–2566.

Hugues, M., Teisseire, M., Chauveau, J.-M., Vinter, B., Damilano, B., Duboz, J.-Y. and Massies, J., (2007). Optical determination of the effective wetting layer thickness and composition in InAs⁄Ga(In)As quantum dots. *Phys. Rev. B*, 76(7), pp.2–7.

Ichimiya, A. and Cohen, P.I., (2004). *Reflection High-energy Electron Diffraction*, United Kingdom: Cambridge University Press.

Ichimiya, A., Sato, T., Sueyoshi, T. and Horio, Y., (1994). Formation of √21x√21 structure by gold deposition on Si(111) √3x√3-Ag surface and wavering behavior. *Surf. Rev. Lett*, 1, pp.1–7.

Jacobi, K., (2003). Atomic structure of InAs quantum dots on GaAs. *Progress in Surf. Sci.*, 71(5-8 SPEC), pp.185–215.

Joyce, B. a, Dobson, P.J. and Neave, J.H., (1986). RHEED studies of heteroepitaxial and quantum well formation during MBE growth-From multiple scattering to band offsets. *Surf. Sci.*, 168, pp.423–438.

Joyce, B.A., (1981). Molecular beam epitaxy. *Phys Educ*, 16, pp.328-332.

Joyce, B.A.. and Vvedensky, D.D., (2004). Self-organized growth on GaAs surfaces. *Materials Science and Engineering: R: Reports*, 46(6), pp.127–176.

Keating, P.N., (1966). Relationship between the macroscopic and microscopic theory of crystal elasticity. I. Primitive crystals. *Phys. Rev.*, 152(2), pp.774–779.

Kikuchi, S., (1928). Diffraction of cathode rays by mica. *Nature*, 121, pp.271-274.

Kim, J.S. and Bae, I., (2003). Optical properties of wetting layer in InAs quantum dots at different growth temperatures. *J. Koren Phys. Soc*., 42, pp.483–486.

Kipp, T., Welsch, H., Strelow, C., Heyn, C. and Heitmann, D., (2006). Optical modes in semiconductor microtube ring resonators. *Phys. Rev. Lett.*, 96(7), pp.1–4.

Kiravittaya, S., Songmuang, R., Rastelli, a., Heidemeyer, H. and Schmidt, O.G., (2006). Multi-scale ordering of self-assembled InAs/GaAs(001) quantum dots. *Nanoscale Research Lett.*, 1(1), pp.1–10.

Kratzer, P., Liu, Q., Acosta-Diaz, P., Manzano, C., Costantini, G., Songmuang, R., Rastelli, A., Schmidt, O. and Kern, K., (2006). Shape transition during epitaxial growth of InAs quantum dots on GaAs(001): Theory and experiment. *Phys. Rev. B*, 73(20), p.205347.

Krzyzewski, T.J., Joyce, P.B., Bell, G.R. and Jones, T.S., (2002). Wetting layer evolution in InAs/GaAs() heteroepitaxy: effects of surface reconstruction and strain. *Surf. Sci.*, 517(1-3), pp.8–16.

Kudo, T., Inoue, T., Kita, T. and Wada, O., (2008). Real time analysis of self-assembled InAs/GaAs quantum dot growth by probing reflection high-energy electron diffraction chevron image. *J. Appl. Phys.*, 104(7), p.074305.

Labella, V.P., Yang, H., Bullock, D.W., Thibado, P.M., Kratzer, P. and Scheffler, M., (1999). Atomic structure of the GaAs (001)- (2X4) surface resolved using scanning tunneling microscopy and first-principles theory. *Phys. Rev. Lett.*, 83, pp.2989–2992.

Lakhtakia, A. ed., (2004). *The Handbook of Nanotechnoloty. Nanometer Structures: Theory, Modeling, and Simulation*, SPIE Press Monography vol. PM 129.

Landau, L.D. and Lifshitz, E.M., (1975). Course of Theoretical Physics: Volume 7, Theory of Elasticity. Available at: http://www.citeulike.org/group/13900/article/8652119.

Langmuir, I., (1913). The vapor pressure of metallic tungsten. *Phys Rev.*, 2, p.329.

Lee, H., Lowe-webb, R., Yang, W. and Sercel, P.C., (1998). Determination of the shape of self-organized InAs / GaAs quantum dots by reflection high-energy electron diffraction. *Appl. Phys. Lett.*, 72(7), pp.812–814.

Lee, J.W., Schuh, D., Bichler, M. and Abstreiter, G., (2004). Advanced study of various characteristics found in RHEED patterns during the growth of InAs quantum dots on GaAs (0 0 1) substrate by molecular beam epitaxy. *Appl. Surf. Sci.*, 228(1-4),pp.306–312.

Liu, H., T. Wang, Q. Jiang, R. Hogg, F. Tutu, F. Pozzi, and A.S., (2011). Long-wavelength InAs/GaAs quantum-dot laser diode monolithically grown on Ge substrate. *Nature Photonics*, 5, pp.416–419.

Löhr, S., Mendach, S., Vonau, T., Heyn, C. and Hansen, W., (2003). Highly anisotropic electron transport in shallow InGaAs heterostructures. *Phys. Rev. B*, 67(4), pp.1–4.

Madhukar, a, Xie, Q., Chen, P. and Konkar, A., (1994). Nature of strained InAs three-dimensional island formation and distribution on GaAs (100). *Microscopy*, 64, pp.1–3.

Márquez, J., Geelhaar, L. and and Jacobi, K., (2001). Atomically resolved structure of InAs quantum dots. *Appl. Phys. Lett.*, 78(16), p.2309.

Marshall, M.S.J. and Castell, M.R., (2014). Scanning tunnelling microscopy of epitaxial nanostructures. *Chemical Soc. Rev.*, 43(7), pp.2226–39.

Martin, R.M., (1970). Elastic properites of ZnS structure semiconductors. *Phys. Rev. B*, 1,pp. 4005-4011.

Matthews, J.W. and Blakeslee, A.E., (1974). Defects in epitaxial multilayers. *J. Crys. Growth*, 27, pp.118–125.

Meng, H.J., Lu, J., Yan, S., Tan, P.H. and Zhao, J.H., (2008). flux on the magnetic property of (In,Cr)As quantum dots. *EPL (Europhysics Letters)*, 84(5), p.58007.

Michler, P., Kiraz, A., Becher, C., Schoenfeld, W. V, Petroff, P.M., Zhang, L., Hu, E. and Imamoglu, A., (2000). A quantum dot single-photon turnstile device. *Science (New York, N.Y.)*, 290(5500), pp.2282–2285.

Miyake, S., (1938). A note on the reflection of cathode rays from a crystal surface. *Sci. Pap. Inst. Phys. Chem. Res.*, 34, pp.286-294.

Muller, P. and Kern, R., (1998). Equilibrium shape of epitaxially strained crystals (Volmer — Weber case). *J. Crys. Growth*, 193, pp.257–270.

Musgrave, M.J.P. and Pople, J.A., (1962). A general valence force field for diamond. *Proceedings of the Royal Society of London*, 268, pp.474–484.

Nabetani, Y., Ishikawa, T., Noda, S. and Sasaki, A., (1994). Initial growth stage and optical properties of a three-dimensional InAs structure on GaAs. *J. Appl. Phys.*, 76(113), pp.347–352.

Neave, J.H., Joyce, B. a., Dobson, P.J. and Norton, N., (1983). Dynamics of film growth of GaAs by MBE from Rheed observations. *Applied Physics A Solids and Surfaces*, 31(1), pp.1–8.

Neogi, A., Everitt, H., Kuroda, T. and Tackeuchi, A., (2005). Size dependence of carrier recombination efficiency in GaN quantum dots. In *IEEE Transactions on Nanotechnology*. 4, pp.297–299.

Nishikawa, S. and Kikuchi, S., (1928). Diffraction of cathode rays by calcite. *Nature*, 122(3080), pp.726–726.

Northrup, J.E. and Froyen, S., (1993). Energies of GaAs(001)-(2X4) and (4X2) reconstructions. *Phys. Rev. Lett*, 71, p.2276.

Park, S.K., Tatebayashi, J. and Arakawa, Y., (2004). Formation of ultrahigh-density InAs/AlAs quantum dots by metalorganic chemical vapor deposition. *Appl. Phys. Lett.*, 84(11), pp.1877–1879.

Parker, E.H.C., (1985). *The Technology and Physics of Molecular Beam Epitaxy*, Plenum Press, New York and London.

Patella, F., Arciprete, F., Fanfoni, M., Sessi, V., Balzarotti, A. and Placidi, E., (2005). Reflection high-energy electron diffraction observation of surface mass transport at the two- to three-dimensional growth transition of InAs on GaAs(001). *Appl. Phys. Letters*, 87(25), pp.1–3.

Pavesi, L. and Guzzi, M., (1994). Photoluminescence of AlxGa1-xAs alloys. *J. App. Phys.*, 75(10), pp.4779–4842.

Pehlke, E., Moll, N., Kley, A. and Scheffler, M., (1997). Shape and stability of quantum dots. *Applied Physics A: Materials Science & Processing*, 65(6), pp.525–534.

Placidi, E., Arciprete, F., Fanfoni, M., Patella, F. and Balzarotti, A., (2008). The InAs/GaAs (001) quantum dot transition: Advances on understanding. In Z. Wang, ed. *Self-assembled Quantum Dots*. Springer, New York

Placidi, E., Arciprete, F., Magri, R., Rosini, M., Vinattieri, A., Cavigli, L., Gurioli, M., Giovine, E., Persichetti, L., Fanfoni, M., Patella, F., and Balzarotti, A., (2012). InAs epitaxy on GaAs(001): A model case of strain-driven self-assembly of quantum dots. In S. Bellucci, ed. *Self-Assembly of Nanostructures*, Springer, NewYork.

Placidi, E., Della Pia, A. and Arciprete, F., (2009). Annealing effects on faceting of InAs/GaAs(001) quantum dots. *Appl. Phys. Lett.*, 94(2), p.021901.

Prohl, C., Höpfner, B., Grabowski, J., Dähne, M. and Eisele, H., (2010). Atomic structure and strain of the InAs wetting layer growing on GaAs(001)-c(4×4). *J. Vacuum Sci. & Tech. B: Microelectronics and Nanometer Structures*, 28(4), p.C5E13.

Prutskij, T., Pelosi, C. and Attolini, G., (2011). Temperature quenching of photoluminescence of ordered $GaInP_2$ alloy under different excitation densities. *Crystal Research and Tech.*, 46(2), pp.127–134.

Pryor, C., Kim, J., Wang, L.W., Williamson, a. J. and Zunger, A., (1998). Comparison of two methods for describing the strain profiles in quantum dots. *J. Appl. Phys.*, 83(5), p.2548.

Pukite, P., (1988). *Reflection High-energy Electron Diffraction Studies of Interface Formation*. Ph.D Thesis, University of Minnesota.

Rajapaksha, C., (2010). *Epitaxial growth and real time characterization of self-assembled quantum dots using Reflection High-energy Electron Diffraction*.Ph.D Thesis, University of Houston.

Rajapaksha, C. and Freundlich, A., (2009). Real time extraction of quantum dot size from RHEED intensity profiles. *J. Crys. Growth*, 311(7), pp.1758–1760.

Rao, E.V.K., Alexandre, F., Masson, J.M., Allovon, M. and Goldstein, L., (1985). Low-temperature photoluminescence properties of high-quality GaAs layers grown by molecular-beam epitaxy. *J. of Appl. Phys.*, 57(2), pp.503–508.

Raviswaran, A., Liu, C.P., Kim, J., A., Cahill, D.G. and Gibson, J.M., (2000). Evolution of coherent islands during strained-layer Volmer-Weber growth of Si on Ge(111). *Phys. Rev. B*, 63, pp.1–5.

Rosei, F., Motta, N., Sgarlata, A., Capellini, G. and Boscherini, F., (2000). Formation of the wetting layer in Ge/Si(111) studied by STM and XAFS. *Thin Solid Films*, 369(1), pp.29–32.

Saito, H., Nishi, K. and Sugou, S., (1999). Shape transition of InAs quantum dots by growth at high temperature. *Appl. Phys. Lett.*, 74(9), p.1224.

Sanguinetti, S., Henini, M., Grassi Alessi, M., Capizzi, M., Frigeri, P. and Franchi, S., (1999). Carrier thermal escape and retrapping in self-assembled quantum dots. *Phys. Rev. B*, 60(11), pp.8276–8283.

Santori, C., Pelton, M., Solomon, G., Dale, Y. and Yamamoto, Y., (2001). Triggered single photons from a quantum dot. *Phys. Rev. Lett.*, 86(8), pp.1502–1505.

Schmidt, W.G., Bechstedt, F. and Bernholc, J., (2002). GaAs(001) surface reconstructions: geometries, chemical bonding and optical properties. *App. Surf. Sci.*, 190(1-4), pp.264–268.

Seravalli, L., Trevisi, G. and Frigeri, P., (2012). 2D–3D growth transition in metamorphic InAs/InGaAs quantum dots. *CrystEngComm*, 14(3), p.1155.

Shchukin, V. a., Ledentsov, N.N., Kop'Ev, P.S. and Bimberg, D., (1995). Spontaneous ordering of arrays of coherent strained islands. *Phys. Rev. Lett.*, 75(16), pp.2968–2971.

Song, H.Z., Usuki, T., Nakata, Y., Yokoyama, N., Sasakura, H. and Muto, S., (2006). Formation of InAs GaAs quantum dots from a subcritical InAs wetting layer: A reflection high-energy electron diffraction and theoretical study. *Phys. Rev. B - Condensed Matter and Materials Physics*, 73(11), pp.1–8.

Songmuang, R., Kiravittaya, S. and Schmidt, O.G., (2003). Shape evolution of InAs quantum dots during overgrowth. *J. Crys. Growth*, 249(3-4), pp.416–421.

Srivastava, G.P. and Jenkins, S.J., (1996). Atomic geometry and bonding on the GaAs(001)-beta2(2x4) surface from ab. *Phys. Rev. B*, 53(19), pp.589–592.

Stranski, I.N. and Krastanov, L., (1938). Abhandlungen der mathematisch-naturwissenschaftlichen klasse IIb. *Akademie der Wissenschaften Wien*, 146, pp.797–810.

Totten, G.E. and Liang, H., (2004). *Surface Modification and Mechanisms: Friction, Stress and Reaction Engineering*,. Marcel Dekker Inc., New York.

Tsukamoto, S., Honma, T., Bell, G.R., Ishii, A. and Arakawa, Y., (2006). Erratum: Atomistic insights for InAs quantum dot formation on GaAs(001) using STM within a MBE growth chamber. *Wiley Inter Science*, 2(5), p.587.

Uccelli, E., Bauer, J., Bichler, M., Schuh, D., Finley, J.J., Abstreiter, G. and Morral, a F., (2008). Self-assembly of InAs quantum dot structures on cleaved facets. In Z. M. Wang, ed. *Self-assembled Quantum Dots*. Springer.New York.

Vanderbilt, D. and Wickham, L.K., (1991). Elastic relaxation energies of coherent germanium islands on silicon. In D. J. Srolovitz, C. V. Thompson, and J. Y. Tsao, ed. *Evolution of Thin-Film and Surface Microstructure*. MRS Proc. 202, p. 555.

Volmer, M. and Weber, A., (1925). Keimbildung in übersättigten Gebilden. *Z. Physikal. Chemie*, 119, p.277.

Vorobiev, Y.V., Torchynska, T.V. and Horley, P.P., (2013). Effect of aspect ratio on energy of optical transitions in a pyramid-shaped quantum dot. *Physica E: Low-dimensional Systems and Nanostructures*, 51, pp.42–47.

Whaley, G.J. and Cohen, P.I., (1990). Diffraction studies of the growth of strained epitaxial layers. In *MRS Proc*., 160, p.135.

Winzer, a. T., Goldhahn, R., Gobsch, G., Heidemeyer, H., Schmidt, O.G. and Eberl, K., (2002). Optical properties of wetting layers in stacked InAs/GaAs quantum dot structures. *Physica E: Low-dimensional Systems and Nanostructures*, 13(2-4), pp.289–292.

Wood, C.E.C., (1981). RED intensity oscillations during MBE of GaAs. *Surf. Sci.*, 108, pp.L441-L443.

Xu, M.C., Temko, Y., Suzuki, T. and Jacobi, K., (2005). Shape transition of InAs quantum dots on GaAs(001). *J. Appl. Phys.*, 98(8), p.083525.

Yang, H. –N., Wang, G. –C. and Lu, T. –M., (1993). *Diffraction from Rough Surfaces and Dynamic Growth Fronts*, World Scientific Publishing Co. Singapore.

Zhang, H., Chen, Y., Zhou, G., Tang, C. and Wang, Z., (2012). Wetting layer evolution and its temperature dependence during self-assembly of InAs/GaAs quantum dots. *Nanoscale Research Lett.*, 7(1), p.600.

Appendix A

Calculation of RHEED pattern: Kinematical approach

In kinematical theory, the geometrical or kinematical features of the diffraction pattern depend primarily on the positions of the scatterers and not on the details of the crystalline potential. The strength of the interaction is included by the means of a scattering factor. The mean potential is included by the refraction of the incident angle when a beam enters the crystal. Furthermore, inelastic processes, related to imaginary part of the potential, are included by factor that describes absorption.

The Schrödinger equation for electron scattering by a crystal potential ***V(r)***

$$-\frac{\hbar^2}{2m}\nabla^2\psi - eV(\boldsymbol{r})\psi = E\psi, \qquad \text{(A. 1)}$$

When the crystal potential is week for electron scattering taking the incident field as the driving field at each point in the scatterer, Born approximation can be applied to solve the above equation. Wave function ψ turns to be

$$\psi = \psi_0 + \frac{1}{4\pi r} e^{ikr} \int U(\boldsymbol{r}') e^{-is.r'}\, d\tau', \qquad \text{(A. 2)}$$

where **s** is the scattering vector defined as $\boldsymbol{s} = \boldsymbol{k} - \boldsymbol{k}_0$. The wave vectors $\boldsymbol{k}$ and $\boldsymbol{k}_0$ corresponds to the scattered and incident electrons respectively. For the calculations of $|\boldsymbol{k}|$, the incorporation of electron kinetic energy in to de Broglie relation is used.

$$|\boldsymbol{k}| = \frac{2\pi}{\lambda} = 2\pi \Big/ \sqrt{\frac{h^2}{2mE}} \quad , \tag{A.3}$$

where E is the the kinetic energy(eV) , m is the electron mass(kg), electron wavelength λ(Å) and h is the Planck's constant. The above equation holds true for non-relativistic case where λ < 50 keV.

$U(\boldsymbol{r})$ is the reduced potential $2me/\hbar^2 \; V(\boldsymbol{r})$. Equation A.3 is then can be interpreted as

$$\psi = \psi_0 + A(\boldsymbol{s})\frac{e^{ikr}}{r} \quad , \tag{A.4}$$

where the scattering amplitude is

$$A(\boldsymbol{s}) = \frac{1}{4\pi}\int U(\boldsymbol{r}')e^{-i\boldsymbol{s}.\boldsymbol{r}'}\, d\tau' \, . \tag{A.5}$$

A sum of atomic potentials $U_j^a(\boldsymbol{r} - \boldsymbol{r_j})$ is substitute for $U(\boldsymbol{r})$ to calculate$A(\boldsymbol{s})$.

$$A(\boldsymbol{s}) = \frac{1}{4\pi}\int U(\boldsymbol{r})e^{-i\boldsymbol{s}.\boldsymbol{r}}\, d\tau = \frac{1}{4\pi}\sum_j e^{-i\boldsymbol{s}.\boldsymbol{r}_j}\int U_j^a(\boldsymbol{r})e^{-i\boldsymbol{s}.\boldsymbol{r}}\, d\tau, \tag{A.6}$$

Adopting the atomic scattering factor

$$f_j(\boldsymbol{s}) = \frac{1}{4\pi}\int U_j^a(\boldsymbol{r})e^{-i\boldsymbol{s}.\boldsymbol{r}}\, d\tau \, . \tag{A.7}$$

Since the scattering in RHEED is strongly peaked in the forward direction, plane-wave Born approximation can be applied. Doyle and Turner calculated the atomic scattering

factor using the Hartree-Fock approximation, and expanded *f(S)* into a Gaussian series (Doyle and Turner 1968):

$$f(s) = \sum_{j=1}^{4} a_j \exp\left[-b_j \left(\frac{S}{4\pi}\right)^2\right], \qquad (A.8)$$

The Doyle-Turner coefficients a_j and b_j are listed in Table A.1.

Table A.1: Parameterization of the Debye-Waller factor of InAs and GaAs with zinc-blend structure for T > 80K.

	a1	b1	a2	b2	a3	b3	a4	b4
In	3.1528	66.6492	3.5565	14.4494	2.8180	2.9758	0.8842	0.3345
As	2.3989	45.7179	2.7898	12.8166	1.5288	2.2799	0.5396	0.3277
Ga	2.3205	65.6019	2.4855	15.4577	1.6879	2.5806	0.5992	0.3510

Appendix B

B.1 Photoluminescence (PL)

Photoluminescence is the spontaneous emission of light from a material under optical excitation. It is a non-destructive and selective method of probing discrete electronic states. PL often originates near the surface of a material, PL analysis is used to characterize surfaces and interfaces. The intensity and spectral content of the emitted PL is a direct measure of various material properties such as band gap determination, impurity levels and defect detention and recombination mechanisms. The following is a schematic of the PL system at CAM facility.

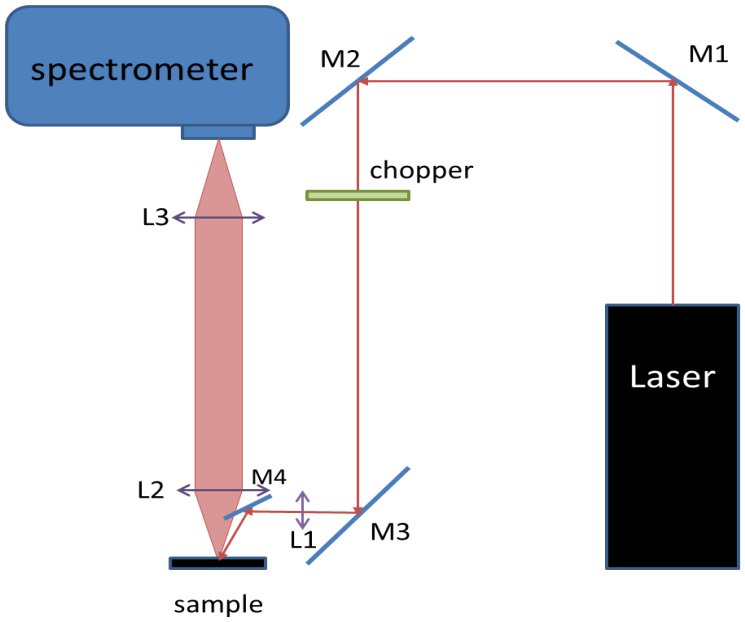

Figure B.1: Schematic of PL set up.

The PL system we used in our studies is shown in Figure B.2. A *Milles Griot* red Laser of wavelength 632.8 nm Laser was used in our PL set up. The sample is placed in a helium-cooled cryostat, which can go as low as 10 K. A heater and a temperature controller unit

are used for the temperature control of the samples during PL vs. temperature studies. The laser light is fi tuned with highly precise optics before hitting the cryostat entrance. The PL signal from the sample is focused using two lenses at the entrance of a Triax 320TM monochromator and was detected by either InGaAs or Si detector after the monochromator. The collected spectral signal was locked to the given frequency using a chopper and Stanford lock-in device to avoid the undesired white noise from the stray light and ac power frequency while a computer that controls the configuration of the monochromator, records the data.

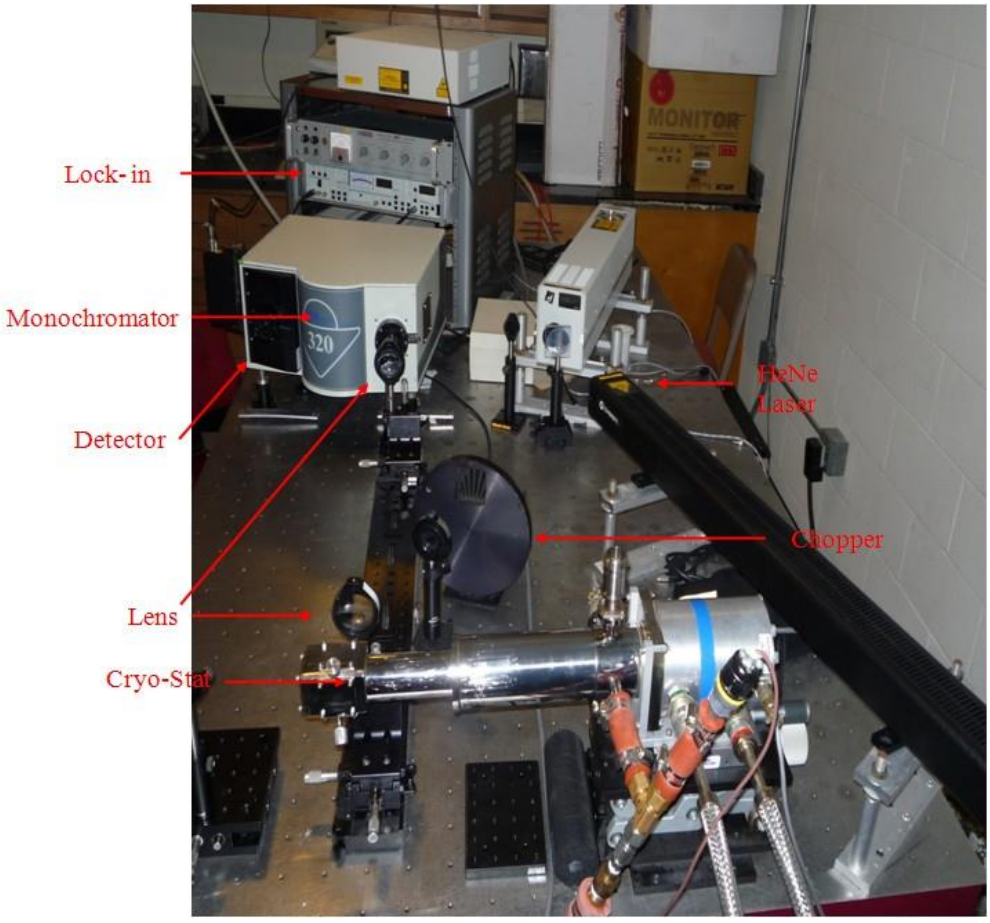

Figure B.2: PL setup at CAM facility

B.2 Atomic Force Microscopy (AFM)

The atomic force microscopy is a scanning probe microscopic tool which is designed to measure local properties such as a roughness of a surface at a high resolution including height, friction, and magnetism.

The AFM consists of a cantilever with a sharp tip (probe) at its end that is used to scan the specimen surface and it measures the force between the sample surface and the tip. When the tip is brought into proximity of a sample surface, forces between the tip and the sample lead to a deflection of the cantilever according to Hooke's law.

In this study a non-contact imaging mode was used. In this mode the tip of the cantilever does not contact the surface and the cantilever oscillates at either resonant frequency or amplitude modulation. Autoprobe cp atomic force microscope with a cantilever (fabricated by Applied NanoStructures, Inc.) with nominal tip radius 4 nm were the apparatus used. Following Figure B.3 shows the experimental set up used in the study).

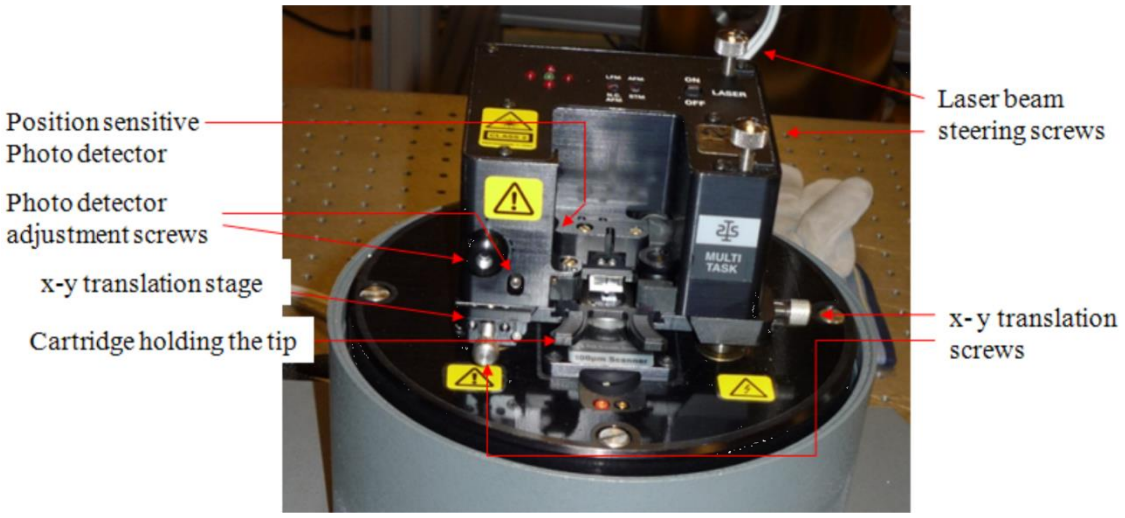

Figure B.3: Set up of atomic force microscopy.